



Growth and Characterization of Niobium/Gadolinium Superconductor-Ferromagnet Nano-composites

Hamed Parvaneh

*A dissertation submitted for the degree of Master of Science
in the field of Nanomaterials and Nanotechnology*

Department of Materials Science and Engineering
Royal Institute of Technology
Stockholm, Sweden

March 2006



**UNIVERSITY OF
CAMBRIDGE**



**Device Materials Group
Dept. of Materials Science and Metallurgy**

In the Name of God
the Compassionate
the Merciful

ABSTRACT

Superconductivity and ferromagnetism are two antagonistic physical phenomena which their coexistence in a *uniform* material can be resolved only under extraordinary conditions. The reason for that is the phonon-mediated attraction energy between electrons which results in the formation of the so-called Cooper pairs, is usually smaller than the exchange (Zeeman) interaction between electrons which tend to align the electron spins. However, non-zero total momentum Cooper pairs can be accomplished even in the presence of an exchange field as surprisingly! predicted first by Fulde and Ferrel [1] and independently by Larkin and Ovchinnikov [2] nearly 50 years ago. This coexistence has already been observed experimentally in both bulk samples [3, 4] and in thin films [5-7] which result from a different type of electron-pairing mechanism which electrons with spin pointing in the same direction team up to form Cooper pairs with one unit of spin, resulting in the so-called triplet superconductivity. Apart from this so-called ferromagnet-superconductors which both superconducting and ferromagnetism order parameters are present in a uniform material, hybrid systems [8] are made from materials with different or even mutually exclusive properties. Therefore the overall property can be strongly affected by the interaction between constituent materials. The present work, concerns such a hybrid system where Nb, a superconducting metal having transition temperature below 9.5K, is placed in contact with a ferromagnetic metal, Gd with bulk Curie temperature of around 290 K in a form of a nanocomposite. The mutual immiscibility of these two elements gives us the opportunity to take advantage of both the superconduction and ferromagnetism properties of the constituents and further study the transport and magnetic behavior of the system and their effects on each other specially on the critical current of the superconductor which is expected to be modified by the proximity of the ferromagnetic metal.

- [1] P. Fulde and R. A. Ferrel, *Phys. Rev.* 135, A550 (1964).
- [2] A. I. Larkin and Y. N. Ovchinnikov, *Sov. Phys. JETP* 20, 762 (1965).
- [3] D. Aoki *et al.*, *Nature (London)*, 413, 613 (2001).
- [4] S. S. Saxena *et al.* *Nature (London)*, 406, 587 (2000).
- [5] T. Kontos *et al.* *Phys. Rev. Lett.* 89, 137007 (2002).
- [6] V. V. Ryazanov *et al.* *Phys. Rev. Lett.* 86, 2427 (2001).
- [7] R. Meservey *et al.*, *Phys. Rep.* 238, 173 (1994).
- [8] I. F. Lyuksyutov *et al.*, *Adv. in Phys.* 54, 1, 67–136, (2005).

PREFACE

I declare that this dissertation is the result of my own work in the Device Materials Group, Department of Materials Science and Metallurgy, Cambridge University, in the theme of the thesis project for the fulfillment of the degree of *Master of Science*.

This thesis work includes nothing which is the outcome of work done in collaboration except where specifically stated. This report has been submitted to the Materials Chemistry Division of the Department of Materials Science and Engineering at the Royal Institute of Technology (KTH), Stockholm, Sweden for the degree of *Master of Science* in the field of *Nanotechnology and Nanomaterials*. No part of this dissertation has been or is being submitted for any other qualification at this or any other University.

Hamed Parvaneh

Cambridge

February 2006

ACKNOWLEDGEMENTS

I would have not been able to carry out this research without the help of many people. Firstly, I would like to thank both of my supervisors; Professor Mamoun Muhammed at the Royal Institute of Technology, Stockholm, for his support and giving me the opportunity to explore other research environments and also Professor Mark Blamire for his guidance and advice throughout this project. Many thanks to Dr. Zoe Barber for her thorough guidance regarding the sputter deposition system. A special thank you to Dr. Nadia Stelmashenko for her infinite patience in training me how to use the Mark III sputter deposition system and Atomic Force Microscopy and all her corrections and reminders. Many thanks to the wonderful technical staff especially Dr Mary Vickers for her amazing wealth of knowledge concerning all the aspects of the XRD and her useful theoretical comments and corrections to my work and also Andrew Moss for training me how to use the instruments. I owe a lot to David Nicole and David Vowles for their superb training regarding the SEM and FEG-SEM facilities.

Important on a day to day basis to my research during my stay in Cambridge, have been all the other group members of the Device Materials Group. I like to thank them all for being so nice and helpful and for providing such a lovely and friendly environment which made it more convenient to carry out research. Special thanks to my officemate and my friend Jason Robinson for all the fruitful discussions (scientific and political!) and his help with FIB and other instruments and also for proof reading some parts of my thesis. I hope all the best for him and his adorable one!

I owe more than words can describe to Dr. Enric Pardo for all the great discussions regarding the theoretical aspects of superconductivity and helping me interpreting the results and proof reading some parts of my thesis. A huge thank to Dr. Anna Palau for performing some of the measurements and also for patterning my films with lithography technique. I was so impressed by her wealth of knowledge and ability to organize and process HUGE amounts of data in Klaidagraph software without messing up!

I am also grateful to my friend Edgar Patino for great discussions, Laura Singh for answering lots of my questions regarding sputtering system and nice chats in the sputtering room, Dr. Wilma Eerenstein for training me how to use Vibrating Sample Magnetometer and her patience for installing LHe cryostat! Alex Michtchenko, Rainer Schmidt, and Patrick Zerrer for their companionship in the parties and chill outs during weekends.

Back in Stockholm, I would like to thank two of my lecturers, Dr. Muhammet Toprak and Dr. Maria Mikhaylova for their wealth of knowledge and for all the efforts they put for teaching us. Having them as my teachers and friends; was absolutely a great pleasure for me.

Finally I would like to have an exclusive thank you my family and especially my parents for their love, support and constant guidance and care throughout my life. May God bless you two; my mom and dad, as I could never ever thought of any two persons sacrificing and dedicating themselves to my success so trustworthy and humbly and without any expectation whatsoever. I wish I could return all these kindness. My brother and sister, thank you very much for your encouragement, company and support throughout the years. I still have to thank to the rest of my friends, whom I can't name all, but I am sure know I owe them a lot for all the good times together.

*I DEDICATE THIS THESIS TO MY PARENTS
WHO HAVE ALWAYS BEEN THERE FOR ME
IN DEEDS AND IN NEEDS...*

TABLE OF CONTENTS

Abstract	ii
Preface	iii
Acknowledgements	iv
1 Introduction	1
<i>Bibliography</i>	6
2 Theoretical Background	8
2.1 Superconductivity Phenomenon	9
2.2 Different Types of Superconductivity (Ginzburg-Landau Theory)	10
2.3 Vortex state in Type II Superconductors	14
2.4 Flux Pinning in Mixed State of Type II Superconductors	16
2.4.1 Introduction	16
2.4.2 Critical Current in Type II Superconductor, Critical State	16
2.4.3 Interaction of Vortices with pinning centers	20
2.4.4 Interaction of vortices with the surface of a superconductor	21
2.4.5 Interaction of a vortex with a cavity in a superconductor	22
2.4.6 Resistive state	23
2.5 Ferromagnetism	25
2.5.1 Introduction	25
2.5.2 Energy of Magnetic Materials	25
2.5.3 Domain Walls	26
<i>Bibliography</i>	28
3 Experimental Methods	29
3.1 Thin Film Deposition	30
3.1.1 Sputter Deposition Technique	30
3.1.2 Sputter deposition mechanism	30
3.1.3 Types of Sputtering Techniques	33
3.1.3.1 Direct Current (DC) Sputtering	33
3.1.3.2 Magnetron Sputtering	33
3.1.3.3 Radio Frequency (RF) Sputtering	34
3.2 Film Deposition Experimental Runs	36
3.2.1 Substrate Preparation	36
3.2.2 Co-Sputtering of Niobium and Gadolinium	36

3.2.3	Thickness Measurement	45
	<i>Bibliography</i>	47
4	Characterization Techniques	48
4.1	Energy-dispersive X-ray Spectroscopy (EDXS)	49
4.1.1	Introduction	49
4.1.2	Principles	49
4.1.3	Sample Preparation	55
4.2	X-ray Diffraction	55
4.2.1	X-ray Generation	55
4.2.2	X-ray Analysis of Thin Films	55
4.2.3	Ward-Wallace Texture Camera	58
4.2.3.1	Introduction	58
4.2.3.2	Description of Camera	58
4.2.3.3	Application of the Camera to Thin Films	59
4.3	Transmission Electron Microscopy	60
4.4	Atomic Force Microscopy (AFM)	61
4.5	T_c Measurements	63
4.6	Measurement Rig	66
4.7.1	Sample Mounting	66
4.7.2	Cryostat	66
4.7.3	Measurement Apparatus	67
4.7.4	Sample Preparation	79
4.7	Vibrating Sample Magnetometer (VSM)	73
4.8	Focused Ion Beam (FIB)	74
	<i>Bibliography</i>	77
5	Results and Discussions	78
5.1	Transition Temperature (T_c)	79
5.2	Energy Dispersive Spectroscopy – SEM	81
5.3	Microstructure Imaging & Topography	84
5.4	X-ray Diffraction	90
5.5	Transport & Magnetization Results	99
5.5.1	Critical Transition Temperature	99
5.5.2	Critical current of Niobium plane and the Nanocomposite	105
5.5.3	Magnetization in the Presence of Flux Pinning	112
	<i>Bibliography</i>	117



In the beginning the Universe was created.

This made a lot of people very unhappy and has been widely regarded as a bad move.

Douglas Adams, "The restaurant at the end of the Universe")

Superconductivity and ferromagnetism are two competing physical phenomena which their coexistence in a *uniform* material, can be resolved under extraordinary conditions. The opposition of these two phenomena is macroscopically manifested by the Meissner effect [1]. A superconductor in its superconducting state tends to expel the magnetic field (below its critical field) whereas a ferromagnet concentrates the magnetic field flux lines in its interior (the effect of magnetic induction). From a macroscopic point of view, there are two interaction energies competing with each other. One is the phonon-mediated attraction (coupling) energy between electrons which results in the formation of Cooper pairs (in a singlet state superconductor) and its value is the measure of the superconductor gap energy, Δ . The other is the electron exchange (Zeeman) interaction which tends to align the electron spins parallel.

The suppression of superconductivity by a ferromagnet which was first explained in transition metals by Ginzburg [2], takes place when the Zeeman energy of the electron pairs in an exchange field, I , exceeds the coupling energy, Δ , hence the electrons align their spins and the time-reversed pairs with zero momentum cannot form. The corresponding critical exchange field for the suppression of superconductivity is $I_C \sim \Delta / \mu_B$, where μ_B is the Bohr magneton [3]. This field acts on electron spins and attempts to align the spin of the electrons along the field direction, the so-called paramagnetic effect. The other magnetic effect which can also destroy the superconductivity is known as “orbital effect” which acts on orbital states of the electrons in a Cooper pair and is a manifestation of the Lorentz force. Since the electrons in a Cooper pair have opposite momenta, the Lorentz force acts in opposite direction and the pairs break up. However, non-zero total momentum Cooper pairs can be

accomplished even in the presence of an exchange field as surprisingly first theorized by Fulde and Ferrel [4] and independently by Larkin and Ovchinnikov [5] nearly 50 years ago (the so-called LOFF state). Observation of superconductivity in organic conductors, heavy fermion systems, the ruthenates and ferromagnetic superconductors provide strong evidence for existence of more exotic types of superconductivity which can not be explained by the BCS theory and in fact there is no unambiguous theoretical explanation for them today. Indeed, superconductivity in ferromagnets must result from a different type of electron-pairing mechanism in which electrons with spin pointing in the same direction team up to form Cooper pairs with one unit of spin, resulting in the so-called triplet superconductivity. This coexistence has already been observed experimentally in both bulk samples [6, 7] and in thin films [8-10].

Apart from these so-called ferromagnet-superconductors, in which both superconducting and ferromagnetic order parameters are present in a uniform material, hybrid systems [11] are being made from materials with different or even mutually exclusive properties. Therefore, the overall properties can be strongly affected by the interaction between constituent materials. A natural way in order to avoid the mutual suppression of superconducting and ferromagnet order parameters is, for example, to separate them by a thin insulating film. Another effective way could be to selectively choose a superconductor (preferably a Type II one because of its more practical promises) and a ferromagnet element, which are mutually immiscible. Then it is possible to take advantage of these two antagonistic phenomena at the same time without worrying about suppression of one by the other, by bringing them together in a form of a composite. Considering the proximity effect and the coherence length of the superconductor into the ferromagnet, two conditions have to be met in order for the supercurrents to percolate among the ferromagnet material. First, the ferromagnet islands should be dispersed in the superconductor matrix rather than vice versa so that the percolative pathways between the ferromagnetic islands can be established. Secondly, the length scale of separation between the superconductor and the ferromagnet or in other words the minimum connections between the superconducting islands should be on the order of the coherence length otherwise if the minimum thickness of the intermediate ferromagnetic grains is comparable to coherence length, then the superconductivity is going to be strongly suppressed. The number of systems that can be chosen for the purpose of this experiment is limited as it is not possible to produce dispersions of ferromagnet elements (Iron, Cobalt and Nickel) in most superconductors since the group VIII elements either make an alloy or intermediate phases with most of the superconducting elements [17].

The technological importance of type II superconductors requires carrying as much amount of electrical current as possible without energy dissipation which occurs when Abrikosov vortices start to move under the influence of Lorentz force. The solution is to

avoid their movements by the so-called pinning centers. The subject of flux pinning itself has attracted a considerable interest firstly because of its technological importance, as mentioned above, and secondly from the fundamental point of view which give model systems to study the interaction of vortices and different pinning centers [19, 20]. Enhancement of pinning, benefiting from direct magnetic interaction of vortices with magnetic pinning centers, has been studied extensively as well.

The original idea was born in 1960's showing pinning enhancement in low-temperature superconductors mechanically mixed with magnetic nanoparticles [21-23]. Further work has focused more on ferromagnetic particles deposited on the surface or in the surface layer and mostly in artificial periodic arrays to emphasize the pinning effectiveness and explore the pronounced commensurability effects in the critical current density as a function of transverse field [25-27]. Van Bael *et al.* [25] studied the periodic arrays of sub-micron ferromagnetic Co/Pt antidot layer and observed the asymmetrical behavior of the magnetization with respect to the sign of the applied field which was attributed to the magnetic contributions. In a similar study, Moschalkov *et al.* and Van Bael *et al.* [26, 27] studied the effect of a periodic sub-micron Co particles placed on a thin Pb film, on the magnetic response of the superconductor and observed the pronounced matching effect after the particles are magnetized showing the importance of stray field of the magnetic particles on pinning properties. Martin *et al.* have successfully fabricated periodic triangular arrays of sub-micrometric ferromagnetic dots of Fe or Ni, creating a strong periodic pinning potential in a superconducting Nb film that is grown on top of it [31]. Recently Snezhko *et al.* studied the magnetic pinning enhancement of a bulk MgB₂ as a Type II superconductor both experimentally and theoretically using the London model approach [24]. Apart from the considerable increase of the total bulk pinning force due to magnetic interaction of embedded nanoparticles, the other important conclusion was that magnetic pinning is more efficient in high- κ ¹ high- T_c superconductors compared to low- κ low- T_c superconductors. Experimental work by Koch *et al.* for micron size ferromagnetic Gd and weakly paramagnetic Yt dispersions in Nb made by solidification from melt, support this idea. They attributed such behavior to the lack of proximity effect due to the much larger precipitate size and spacing compared to the coherence length [17]. Other experiments with iron in Hg-¹³In also showed no macroscopic proximity effects although having much smaller precipitate sizes [32].

Sürgers *et al.* [30] have studied artificially multilayered films of Nb and Gd by electron-beam evaporation for different substrate temperatures mainly focusing on growth morphology, chemical and structural characterizations. The effect of varying the Nb and Gd

¹ $\kappa = \lambda / \xi$ is the Ginzburg-Landau parameter.

thicknesses on superconductivity and magnetic properties of the same system has also been studied by Strunk *et al.* [29]. The effect of ion implantation of non-magnetic impurities on Niobium has been studied and reported before [14-16]. Scholten *et al.* [18] have studied the effect of ion implantation energy of the ferromagnet Gd, on superconducting properties of thin Nb samples.

In this project the growth and characterization of Nb/Gd superconductor-ferromagnet self-assembled nanocomposites by co-sputtering from two targets on a *c*-plane sapphire substrate is carried out. Further characterization of the films and the effect of Gd nanoparticles as pinning centers on critical current and transport properties of superconductor Nb have been studied. Niobium (bcc, $a = 3.299\text{\AA}$) is a type II superconductor which has the highest transition temperature among superconducting elements $T_c = 9.46\text{ °K}$ [12]. Gadolinium (hcp, $a = 3.636\text{\AA}$, $c = 5.783\text{\AA}$) is a ferromagnet with a Curie temperature $T_{Curie} = 293\text{ °K}$ which has the simplest magnetic structure of rare-earth metals [13]. The system Nb/Gd has the advantage that the thermodynamic phase diagram shows no mutual solubility either in solid or in the liquid state [28] which implies having a sharp interface between two components.

The proximity effect of ferromagnets to superconductors in thin film heterostructures and the so-called π -junctions has been studied extensively and is not a concern of this project. The mutual immiscibility of these two elements gives us the opportunity to take advantage of both the superconducting and ferromagnetic properties of the constituents and further study the transport and magnetic behavior of the system and their effects on each other specially on the critical current of the superconductor which is expected to be modified by the proximity of the ferromagnetic metal.

Chapter two of this thesis gives an overview of the relevant theoretical background behind superconductivity and ferromagnetism and their co-existence, followed by some remarks about critical current and enhancement of pinning properties of Type-II superconductor by adding a second phase. Chapter three deals completely with the growth process of the films from substrate preparation to thickness measurements, starting with a little bit theory of different thin film sputtering processes. Chapter four describes the extensive characterization techniques used to study the films, again starting with theoretical aspects and more emphasize on the practical concerns that should be considered in each technique. Finally, chapter five brings the results and further discussion of the observed data.

BIBLIOGRAPHY

- [1] W. Meissner and R. Ochsenfeld, *Naturwissenschaften* **21**, 787 (1933).
- [2] V. L. Gizburg, *Zh Eksp. Teor. Fiz.* **31**, 202 (1965) [*Sov. Phys. JETP* **7** 278 (1958)].
- [3] Yu. A. Izyumov *et al.* *Phys.-Uspe.* **45**, 2, 109-148 (2002).
- [4] P. Fulde and R. A. Ferrel, *Phys. Rev.* **135**, A550 (1964).
- [5] A. I. Larkin and Y. N. Ovchinnikov, *Sov. Phys. JETP* **20**, 762 (1965).
- [6] D. Aoki *et al.*, *Nature (London)*, **413**, 613 (2001).
- [7] S. S. Saxena *et al.* *Nature (London)*, **406**, 587 (2000).
- [8] T. Kontos *et al.* *Phys. Rev. Lett.* **89**, 137007 (2002).
- [9] V. V. Ryazanov *et al.* *Phys. Rev. Lett.* **86**, 2427 (2001).
- [10] R. Meservey and P. M. Tedrow, *Phys. Rep.* **238**, 173 (1994).
- [11] I. F. Lyuksyutov and V. L. Pokrovsky, *Adv. in Phys.* **54**, 1, 67–136, (2005).
- [12] W. Desorbo, *Phys. Rev.* **132**, 107 (1963).
- [13] W. C. Koehler, in R. J. Elliot (ed.), *Magnetic Properties of Rare Earth Metals*, Plenum, New York, pp. 81 (1972).
- [14] P. Crozat, R. Adde, J. Chaumont, H. Bernas and D. Zannatti, in S. T. Picraux, J. G. EerNisse and S. L. Vook (eds.) *Applications of Ion to Metals*, Plenum, New York, pp. 27 (1974).
- [15] O. Meyer, H. Mann and E. Phrilingos, in S. T. Picraux, J. G. EerNisse and S. L. Vook (eds.) *Applications of Ion to Metals*, Plenum, New York, pp. 15 (1974).
- [16] C. H. Arrington and B. S. Denver, *Appl. Phys. Lett.* **26**, 204 (1975).
- [17] C. C. Koch and G. R. Love, *Jour. of Appl. Phys.* **40**, 9 (1969).
- [18] P. D. Scholten and W. G. Moulton, *Phys. Rev. B*, **15**, 3 (1977).
- [19] A. M. Campbell and J. E. Evetts, *Adv. Phys.* **21**, 199 (1972).
- [20] G. Blatter, M. V. Feigel'man, V. B. Geshkenbein, A. I. Larkin and V. M. Vinokur, *Rev. Mod. Phys.* **66**, 1125 (1994).
- [21] D. Brochier and P. Cardin, M. Renard, *Journal de Physique*, **29**, 10, 953 (1968).
- [22] T. H. Alden and J. D. Livingston, *J. Appl. Phys.* **37**, 9, 3551 (1966).
- [23] C. C. Koch and G. R. Love, *J. Appl. Phys.* **40**, 9, 3582 (1966).
- [24] A. Snezhko, Tanya Prozorov and Ruslan Prozorov, *Phys. Rev. B*, **71** 024527 (2005).
- [25] M. J. Van Bael, M. Lange, L. Van Look, V. V. Moshchalkov, Y. Bruynseraede, *Physica C*, **364-365**, 491-494 (2001).
- [26] V. V. Moshchalkov, M. Baert, V. V. Metlushko, E. Rosseel, M. J. Van Bael, K. Temst, Y. Bruynseraede and R. Jonckheere, *Phys. Rev. B* **57**, 3615 (1998).
- [27] M. J. Van Bael, K. Temst, V.V. Moshchalkov and Y. Bruynseraede, *Phys. Rev. B* **59**, 14674 (1999).

- [28] R. P. Elliot, *Constitution of Binary Alloys, First Supplement*, McGraw-Hill, New York, 1965. F. A. Shunk, *Constitution of Binary Alloys, Second Supplement*, McGraw-Hill, New York, 1965.
- [29] C. Strunk, C. Sürgers, U. Paschen and H. v. Löhneysen, *Phys. Rev. B*, **49**, 6 (1994).
- [30] C. Sürgers and H. v. Löhneysen, *Thin Solid Films*, **219**, 69-79 (1992).
- [31] J. I. Martin, M. Velez, J. Nogues and Ivan K. Schuller, *Phys. Rev. Lett.* **79**, 1929 (1979).
- [32] T. H. Alden and J. D. Livingstone, *J. Appl. Phys.* **37**, 3551 (1966).



Learn from yesterday, live for today, hope for tomorrow. The important thing is to not stop questioning.

Albert Einstein

This chapter gives a brief introduction to the theoretical concepts and physics about superconductivity, ferromagnetism which is needed to understand and follow the rest of the thesis. The pinning effect has been given extra attention due to its importance in this project. All the formulas used in this chapter are in the Gaussian Unit System for the sake of simplicity.

2.1 SUPERCONDUCTIVITY PHENOMENON

Superconductivity was discovered in 1911 by H. Kamerlingh Onnes in Leiden [1], in an attempt to measure the changes of resistivity with temperature of mercury, after having successfully liquefied helium in 1908. The mercury could be made very pure by distillation, and this was important because the resistivity at low temperatures tends to be dominated by impurity effects. He found that the resistivity suddenly dropped to zero at 4.2 °K, a phase transition to a zero resistance state. This observation was then followed by other metals showing the same behavior below a certain temperature. This phenomenon was called superconductivity, and the temperature at which it occurred is called its critical temperature, T_c .

Meissner and Ochsenfeld in 1933 discovered that a superconductor below its transition temperature expels all the magnetic field smaller than a certain critical field or in other words is a perfect diamagnet. This is called Meissner effect [2] which distinguishes a superconductor from a merely perfect conductor which will also show zero resistance. Zero resistance implied a nulled electrical field (i.e. $E = 0$) inside a superconductor. In consequence in the case of a superconducting closed loop (e.g. with a shape of a torus), according to Faraday's law, $\oint E dl = -\partial\Phi / \partial t$, any magnetic flux Φ enclosed must be constant. Therefore if the external magnetic field applied on a sample is not strong enough to produce the constant flux required by the superconducting material, it is expelled from the material (perfect diamagnetism). In a perfect conductor this field is trapped inside.

However when the field reaches a certain amount H_c the magnetic flux starts to penetrate into the superconductor and the Meissner effect disappears. The critical magnetic field H_c is related thermodynamically to the free energy difference, or condensation energy, between normal and superconducting states in zero field. This energy is the work done on the specimen by the magnetic field and is equal, per unit volume to:

$$\frac{H_c^2}{8\pi} = f_n(T) - f_s(T) \quad (2.1)$$

Where f_n and f_s are the Helmholtz free energy densities in their respective phases at zero field. It was found experimentally that the dependence of H_c on temperature follows a parabolic law:

$$H_c(T) \approx H_c(0) \left[1 - \left(\frac{T}{T_c} \right)^2 \right] \quad (2.2)$$

Apart from the magnetic field, if a superconductor wire with radius $a \gg \lambda$, λ being the London penetration depth, carries a transport current which exceeds a certain critical current, the superconducting state will also be annihilated. This happens because of the self field produced on the surface of the superconductor wire of magnitude $H = 2I / ca$ by the current (c is the speed of the light) reaches the critical field value. Therefore the value of the critical current would be $I_c = Hca / 2$. This is called Silsbee's criterion for simple superconductors [3].

Despite of the Meissner effect, in reality; however, upon applying a magnetic field some field does penetrate into the superconductor and the depth to which the field penetrates was first introduced in the London's model. London brothers were the first ones who introduced a phenomenological model for electro-dynamical properties of superconductors and in this model they introduced the London's Magnetic field penetration depth, λ :

$$B_x(T) = B(0) \exp(-x / \lambda_L) \quad (2.3)$$

Equation 2.3 which is the solution of the London equation for B_0 parallel to the superconductor surface, show that the magnetic field decays exponentially to zero inside a superconductor. In general the magnetization behavior of the superconductors in a field fall into two classes: Type I and Type II.

2.2 DIFFERENT TYPES OF SUPERCONDUCTIVITY (GINZBURG-LANDAU THEORY)

The macroscopic theory of superconductivity which describes the quantum mechanical nature of the superconductive state is the phenomenological Ginzburg-Landau theory. In this theory, the details of the quantum interactions within the superconducting state may be simplified by a macroscopic quantum wavefunction, ψ where $n_c = \psi \cdot \psi^* = |\psi|^2$ gives the density of the superconducting electron pairs. This quantity is the complex superconducting order parameter in the phenomenological Ginzburg-Landau theory. Based on Landau theory for second order

phase transitions, this theory can describe situations in which the energy gap, Δ , changes in space, such as Superconductor-Normal Metal structures, or Type II superconductors.

It basically considers the free energy expansion associated to a second order phase transition, and includes a term to account for the increase in energy due to the spatial distortion of the order parameter, the interaction of electrons with magnetic field and a final energy term contribution due to magnetic field itself:

$$f = f_{n0} + \alpha|\psi|^2 + \frac{\beta}{2}|\psi|^4 + \frac{1}{2m}\hbar\left|\left(\nabla - \frac{ie}{\hbar c}\vec{A}\right)\psi\right|^2 + \frac{\hbar^2}{8\pi} \quad (2.4)$$

α and β are phenomenological coefficients associated to the variations of the free energy due to temperature (α) and magnetic vector potential, \vec{A} .

Taking the $\partial f / \partial A$ from the expression (2.4), the current density is obtained:

$$\vec{J}_s = \frac{e^*\hbar}{i2m^*}(\psi^*\nabla\psi - \psi\nabla\psi^*) - \frac{e^*}{m^*c}|\psi|^2\vec{A} \quad (2.5)$$

From this equation in the limit where the first term is negligible, the London penetration depth is recognized by replacing $|\psi|^2$ for n_s , which is given as a function of Ginzburg Landau parameters as:

$$\lambda = \sqrt{\frac{m\beta}{4\mu_0e^2|\alpha|}} \quad (2.6)$$

Equivalent to the characteristic length of penetration of the magnetic field as described in the London model. Finally a Ginzburg-Landau coherence length is defined as;

$$\xi_{GL}(T) = \sqrt{\frac{\hbar^2}{2m|\alpha|}} \quad (2.7)$$

Which in contrast with the Pippard-BCS coherence length¹ (ζ_0), ξ_{GL} depends on the temperature. This quantity is the spatial distance over which ψ changes. For a pure superconductor (i.e. $l \rightarrow \infty$) and far below T_c ; $\xi(T) = \xi_0$, therefore these two quantities are not the same but related.

¹ Pippard made a correction to London model and showed that non-locality of the characteristic dimension associated with the superconducting wave function, can be estimated by the uncertainty principle. ζ_0 is Pippard coherence length and represents the smallest size of the superconducting wave packet

The relative sizes of two characteristic length scales, namely as magnetic penetration depth, λ (which determines the length scale over which spatial variations of the local magnetic field occur) and the superconducting coherence length, ξ (which determines the length scale over which the spatial variations of the order parameter take place and come from the Ginzburg-Landau theory), distinguish two different classes of superconductors.

The ratio of the two is called the Ginzburg-Landau parameter, κ ,

$$\kappa = \frac{\lambda}{\xi_{GL}} \quad (2.8)$$

Materials with $\kappa < \sqrt{2}/2$ are known as Type I superconductors with the identifying characteristics of zero electrical resistivity below a critical temperature, zero internal magnetic field (Meissner effect) and a critical magnetic field H_c , above which superconductivity ceases. Also the phase transition from the superconducting state to normal state is abrupt and the temperature dependence of the critical field is well described by expression 2.2.

While instructive for understanding superconductivity, Type I superconductors are of limited practical use because their critical magnetic fields are so small and the superconducting state disappears suddenly at that critical field. Type I superconductors are sometimes called "soft" superconductors. On the contrary, Type II superconductors ($\kappa > \sqrt{2}/2$) show a slightly different behavior comparing to Type I. For Type II superconductors, above a certain critical field H_{c1} , the magnetic flux starts to penetrate the superconductor. This state is known as mixed state. At the upper critical field H_{c2} the material is saturated with magnetic fluxes and the superconductivity state ceases².

The phase diagram for two types of superconductors is shown in Fig. 2.1.

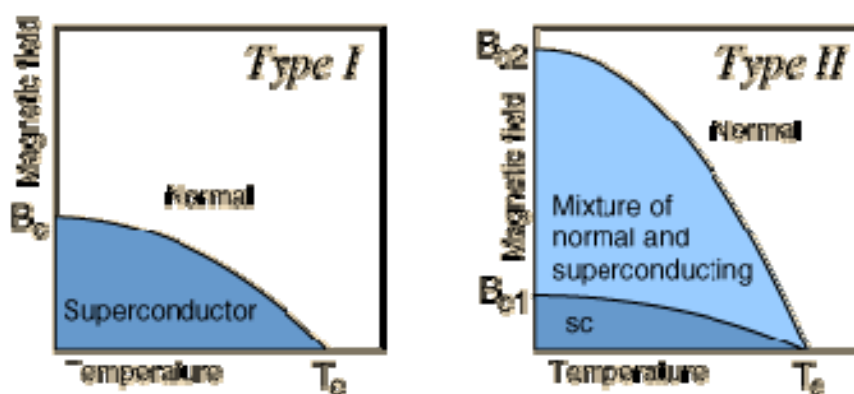


Figure 2.1. Phase diagram of Type I and Type II superconductors showing an extra mixed state in Type II superconductors.

² Some superconductors may retain superconductivity at their surfaces in fields higher than H_{c2} , upto a third critical field H_{c3} .

Beyond H_{c1} the field penetrates as quantized flux lines or vortices. The basic unit of the mixed state is a flux vortex, which essentially contains one quantum of flux, Φ_0 , given by

$$\Phi_0 = \frac{hc}{2e} \quad (2.9)$$

A flux vortex consists of a normal core of radius ξ , surrounded by a cylindrical superconducting region, where a supercurrent circulates around the normal core to generate the single quantum of flux, Φ_0 . This superconducting region is extended to distance λ , the penetration depth. Deep inside the vortex the order parameter, ψ , is zero and the direction of the supercurrent circulating around the vortex is such that coincides with the direction of applied field parallel to the normal core.

Two vortices of the same sign repel each other while two vortices of the opposite sign (vortex-antivortex) would attract each other and when meeting annihilate releasing energy.

The occurrence of the mixed state is caused by the negative energy associated with the normal-superconducting interface in the case of $\kappa > \sqrt{2}/2$. Consequently the energy will be minimized by maximizing the number of the normal cores within the superconducting state. Figure 2.2 shows the variation of the Cooper pair density, n , and the magnetic flux density B in the interior of a Type II superconductor in the mixed state.

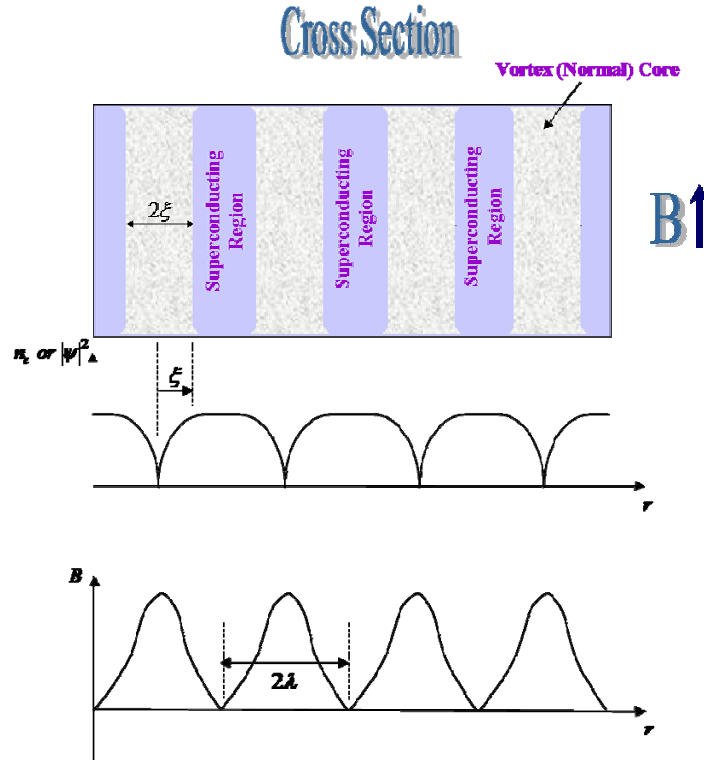


Figure 2.2. Variation of the Cooper pair density n and the magnetic flux density B in the interior of a Type II superconductor.

2.3 VORTEX STATE IN TYPE II SUPERCONDUCTORS

The response of a Type II superconductor to an applied magnetic field can be visualized as follow. Figure 2.3 shows the magnetization curve of an ideal Type II superconductor. At low magnetic fields, the flux vortices are completely expelled from the interior and the superconductor is in the Meissner state. In this state, the free energy of an isolated vortex is greater than the reduction in energy that would be gained if the vortex penetrates the superconductor. Increasing the field and reaching the first critical field $H_{c1} = (\ln(\kappa) + 0.5)\Phi_0 / 4\pi\xi^2 \kappa^2$, the condition for equality of these two energies would just be met and the vortices start to enter the superconductor with further increase of the applied magnetic field. Here $\Phi_0 = 2 \times 10^{-7} \text{ G.cm}^2$ is the flux quantum and $\kappa = \lambda / \xi$ is the Ginzburg-Landau parameter. λ and ξ are London penetration length and coherence length respectively. The equilibrium vortex density at any applied field would be determined by the interaction forces between the vortices as they come closer together. By further increase of the magnetic field, the number of vortices increases and so the total area occupied by the normal cores in the superconductor, therefore the order parameter decreases continuously and finally becomes zero at the upper critical field with a second phase transition to the normal state.

The upper critical field, H_{c2} is given by:

$$H_{c2} = \frac{\Phi_0}{2\pi\xi^2} \quad (2.10)$$

This equation implies that the superconducting state is annihilated due to the overlapping of the normal cores of the vortices. By minimizing the free energy as a function of the lattice configuration, the vortices in the mixed state are arranged in a hexagonal pattern known as Abrikosov lattice (figure 2.4 A).

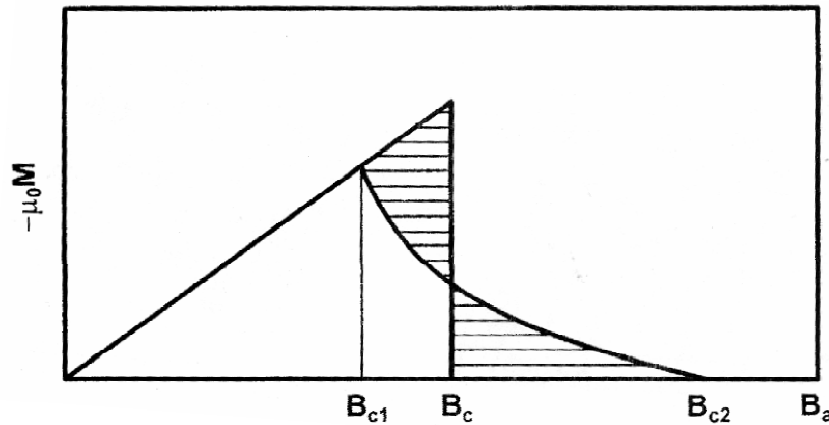


Figure 2.3. Magnetization curve for an ideal Type II superconductor. The shaded areas left and right of the thermodynamical critical field B_c are equal [6].

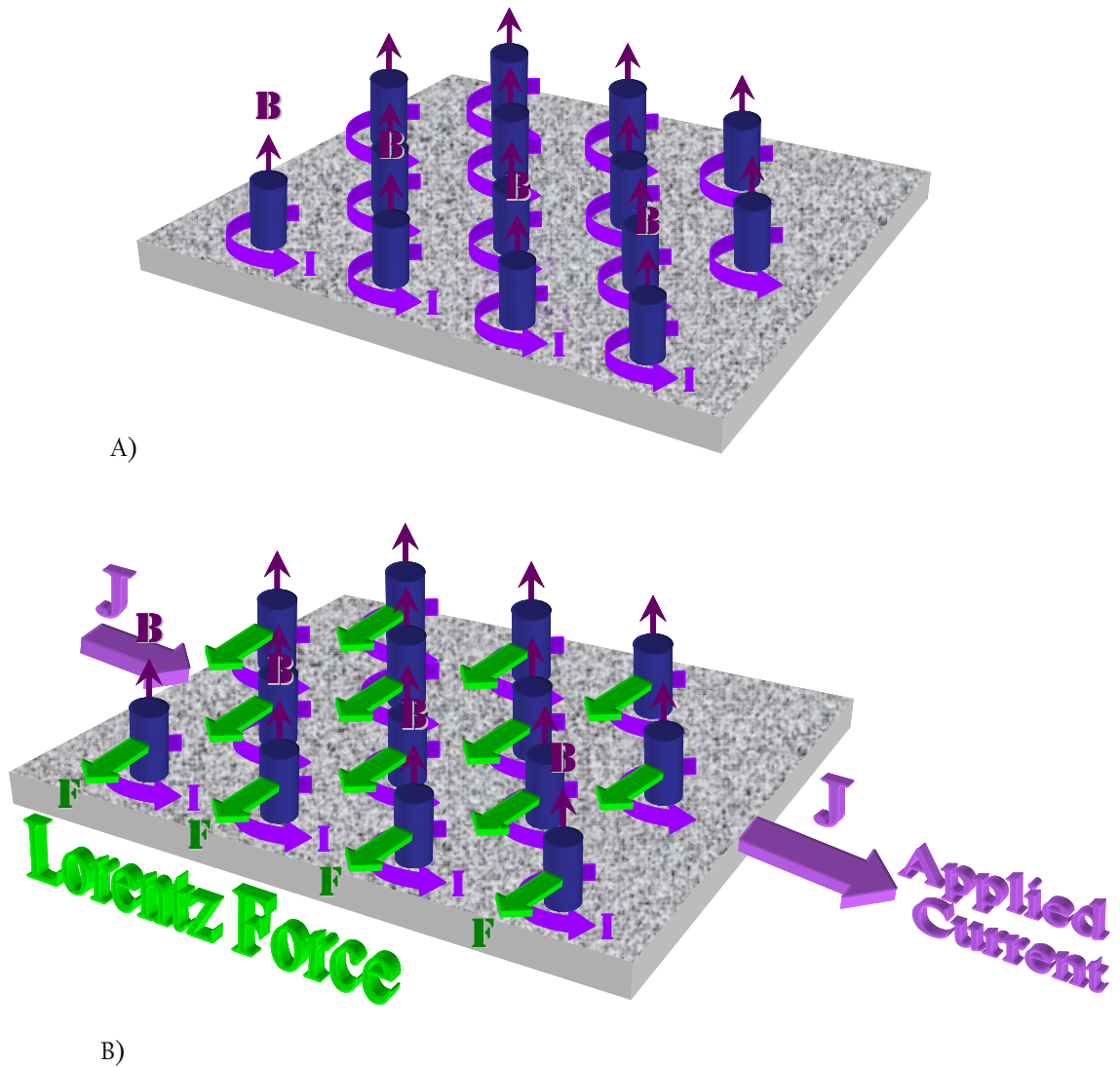


Figure 2.4. The vortex lattice of a Type II superconductor in a magnetic field (A) and in the presence of an applied current (B). The Lorentz force causes flux flow perpendicular to the direction of the current and to the applied magnetic field.

The lattice spacing, a_v , in a triangular lattice is determined by the magnetic flux density in the material and is given by:

$$a_v = \sqrt{\frac{2}{\sqrt{3}} \frac{\Phi_0}{B}} \quad (2.11)$$

Therefore because of the vortex-vortex interactions, the vortices tend to arrange themselves into a vortex lattice. Due to the presence of vortex lattice, a Type II superconductor can withstand a field much higher than the thermodynamic critical field H_{c1} *but* it can not carry a dissipationless electrical current. In the presence of an applied current, J , a Lorentz force (figure 2.4 B) acts on vortices which will be further discussed in section 2.4.

2.4 FLUX PINNING IN MIXED STATE OF A TYPE II SUPERCONDUCTOR

2.4.1 INTRODUCTION

From the practical point of view, the most useful aspects of type II superconductors to date has been the ability to make superconducting solenoids which can supply steady fields of over 10,000 G (gauss) without dissipation of energy because of the resistanceless persistent current. A comparable field produced by a water-cooled copper solenoid would require a steady dissipation of 2MW of power, with attendant cooling problems, and it would not have the essentially infinite stability of the superconducting magnet.

The superconducting material must not only have a critical field substantially higher than the field to be produced, but it must also be able to carry a high current in that field without resistance.

The first requirement is well met by many dirty superconductors since

$$H_{c2} = \frac{\Phi_0}{2\pi\xi^2} \approx \frac{\Phi_0}{2\pi\xi l} \approx \frac{3ck}{e} \frac{T_c}{v_F l} \approx 3 \times 10^4 \frac{T_c}{v_F l} \quad (2.14)$$

Thus given a high T_c and low Fermi velocity (v_F), a low mean free path (l) can lead to a value of H_{c2} of up to ~25,000 Oe (Oersteds) for such brittle materials as V_3Si and Nb_3Sn , and many materials with much more convenient mechanical properties have $H_{c2} \sim 100,000$ Oe. For the high-temperature superconductors, H_{c2} can be as high as 10^6 Oe or higher.

The real problem lies in finding a material that is able to carry a usefully high current in the presence of this strong penetrating field without dissipation of energy. Any appreciable dissipation leads to heating, which degrades the performance further, leading to intolerable catastrophic flux jumps.

2.4.2 CRITICAL CURRENT IN A TYPE II SUPERCONDUCTOR; CRITICAL STATE

If we apply a transport current (i.e. a current from an external source) to a Type II superconductor in the mixed state in the direction perpendicular to the vortices, the current will give rise to a Lorentz force on the vortices which in the case of an absolutely homogenous superconductor (i.e. free of defects), the vortices would start to move at an infinitely small Lorentz force. As the motion of the vortices cause dissipation of energy, the critical current of such an absolutely homogenous superconductor is zero. The Lorentz force in general, is the force exerted on a moving charge particle in an electromagnetic field. The

particle will experience a force due to the electric field of qE and due to the magnetic field $qv \times B$, which combined give they give the Lorentz force (figure 2.5 a).

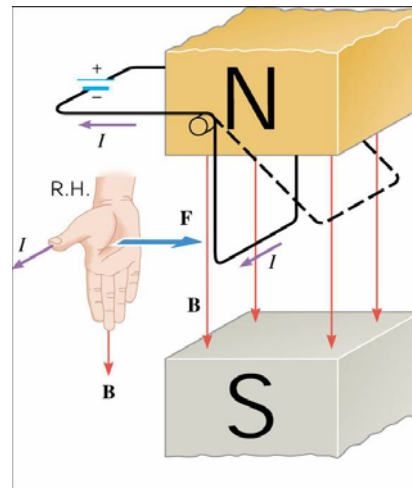
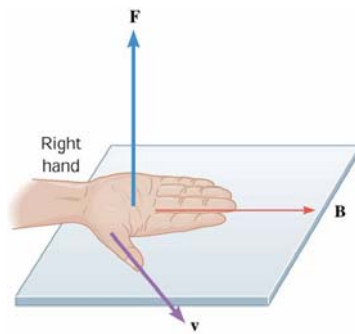
$$F = q(E + v \times B) \quad (2.15)$$

Where

- F : lorentz force
- q : Charge of particle
- v : Instentaneous velocity
- E, B : electric and Magnetic fields

However, in Type II superconductors, upon applying a current, the Lorentz force acts on the individual vortices and tend to move them in the direction determined by the right hand rule. Remember that magnetic field penetrates a Type II superconductor in the form of vortices; hence the direction of the magnetic field is parallel to the long axis of the vortex normal core (figure 2.5 b).

a)



b)

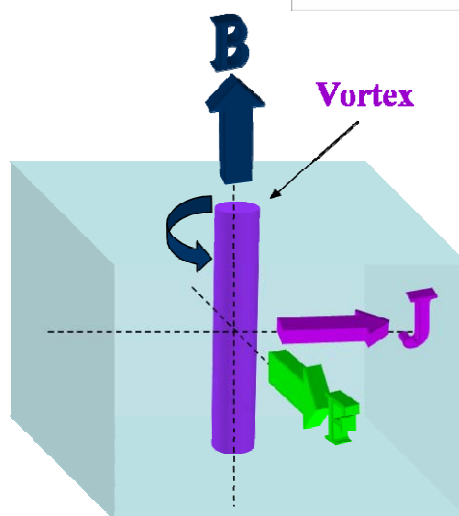


Figure 2.5. a) The Lorentz Force and manifestation of the right hand rule for finding its direction [John Wiley & Sons, Inc.]. b) Manifestation of Lorentz force in a Type II Superconductors.

In the case of an inhomogeneous superconductor containing various types of defects such as grain boundaries, dislocation walls, voids or second-phase precipitates, the vortices are pinned by these defects. Therefore a finite transport current would be required to set them free such that the Lorentz force produced by it would be sufficient to tear the vortices off the defects. These defects are often referred as *Pinning Centers* and the current density corresponding to the initiation of vortex break-off from the pinning centers is called the *Critical Current Density*, J_c .

The critical current density is a structure-sensitive property which can vary as much as several orders of magnitude as a result of thermal or mechanical treatment of the material, leaving the critical temperature, T_c and the critical field H_{c2} virtually unaffected. In applications such as superconductor magnets, the critical current can be as large as 10^6 A.cm^{-1} .

Let us now consider in more details the flow of critical current through a Type II superconductor which contains a large number of pinning centers. In order for the transport current to be distributed over the entire cross section of the specimen, we have to stipulate that the distribution of the vortices is inhomogeneous.

The total current density at a given location is:

$$\vec{j}_{tr} = \frac{c}{4\pi} \text{curl} \mathbf{B} = \frac{c}{4\pi} \nabla \times \vec{B} = \frac{c}{4\pi} \begin{vmatrix} \vec{x} & \vec{y} & \vec{z} \\ \partial/\partial x & \partial/\partial y & \partial/\partial z \\ B_x & B_y & B_z \end{vmatrix} \quad (2.16)$$

Furthermore $B = \Phi_0 n$, is the average field at this location or in other words, the average magnetic induction in a region of dimensions much larger than the distance between the vortices and n is the average vortex density. Therefore from the above equation it follows that the j_{tr} is only non-zero if n is a function of the coordinates, $n = n(r)$.

How can we have such a state with the critical current established across the entire cross-section of the superconductor?

Assume an infinite plate of thickness d (with d much bigger than the vortex radius) containing large number of vortices, with the surfaces of the plate coinciding with the planes $x = \pm d/2$. First we consider the applied magnetic field is zero and a transport current is applied perpendicular to the plate (y axis). At first because of the Meissner-Ochsenfeld effect, the current will flow along the surface of the plate in the thickness of the London penetration length. This current will generate a magnetic field and as soon as the generated field H_I exceeds the critical field H_{c1} , vortices start to penetrate the plate from both surfaces with their signs opposite when they penetrate from the opposite sides. The vortices will be pinned by the defects in the plate while moving toward the center of the plate and hence are not able to penetrate far inside the plate. This implies appearing of a vortex density gradient which

obviously will be the maximum possible gradient corresponding to the critical value of the current. Thus certain parts of the plate near the surfaces will carry the critical current while in the rest of the plate; there will be no current at all. The situation is illustrated in figure 2.6 (a) which shows the distribution of the magnetic field in the plate when it carries a current I_1 .

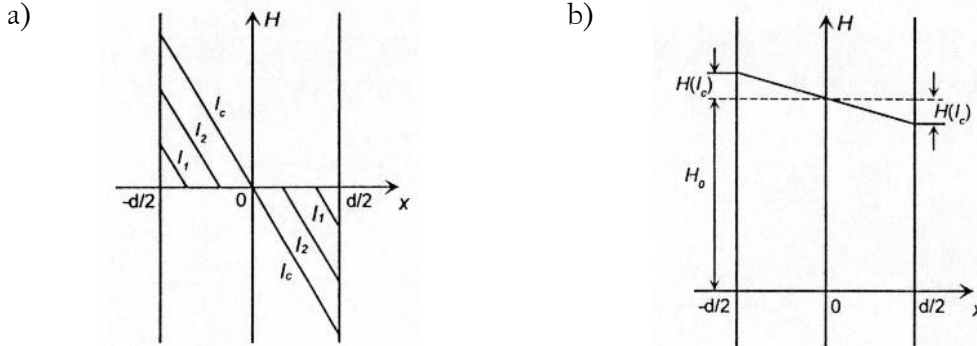


Figure 2.6. Distribution of magnetic field in a plate of thickness d containing pinning centers and carrying a current I . A) External magnetic field is zero and the circulating currents in the plate $I_1 < I_2 < I_c$. B) Finite external magnetic field (distribution of external magnetic field in the critical state, $J_c = \text{const.}$) [4].

If we now increase the current, the vortices while keeping their density gradient, will move closer to the center of the plate so that only a small central part of the plate will remain free of the transport current, while everywhere else the current density will have the critical value. If we keep increasing the current, at some time it will reach a value I_c that the current density at any point of the plate will be of the critical value (as shown in figure 2.6 a), this state is known as *Critical State*.

Let us now apply external magnetic field H_0 parallel to the surface of the plate, perpendicular to the current. Assuming that the field is $H_0 \gg H_1$ (H_1 being the internal field created by current itself) we can assume that every point of the superconductor is in the field H_0 . The distribution of the current in the critical state will be shown as figure 2.6 (b). The critical gradient of the vortex density in the presence of the H_0 is less than that without the field because the critical current is reduced, as will be explained below.

If we consider the Lorentz force per unit length of the vortex as $f_L = j_w \Phi_0 / c$, the Lorentz force per unit volume is $f_L = j_w B / c$ as the density of the vortices is $n = B / \Phi_0$. When the vortices are at rest, the Lorentz force is balanced by the pinning force exerted on the vortices. If the average density of the pinning force per unit volume is denoted by F_p , the critical current must satisfy the following equation:

$$\frac{1}{c} j_c B = F_p \quad (2.17)$$

Which for F_p independent of the external field H_0 , the critical current is $j_c \propto B^{-1}$.

If the distribution of the pinning centers in a superconductor is random, they can not pin an absolutely rigid vortex lattice. For proving the above statement let us shift the vortex lattice by a small distance in the direction of the Lorentz force. This displacement does not affect the energy of the system because the random distribution of the pinning centers relative to the rigid vortex lattice essentially the same as before. Since there is no variation of system energy, there is no restoring force which would push the vortices to their old positions, that is there is no pinning force. But if we assume that the vortex lattice is an elastic medium, then every time the vortex lattice is being shifted, it will adjust itself to the random distribution of the pinning centers so as to ensure that the energy of the vortex system as a whole is a minimum. Therefore if we try to shift the vortex lattice in this case, a certain effort is needed to overcome the restoring force and tearing the vortices off the pinning centers. Obviously the softer the vortex lattice, the more pliable it is, hence the pinning force is larger.

At $H_0 \rightarrow H_{c2}$, the elastic moduli of the vortex lattice decreases, that is, the lattice become softer and the pinning force becomes stronger, which results in a maximum of the critical current at $H_0 \rightarrow H_{c2}$ (peak effect) which is often in agreement with experiment.

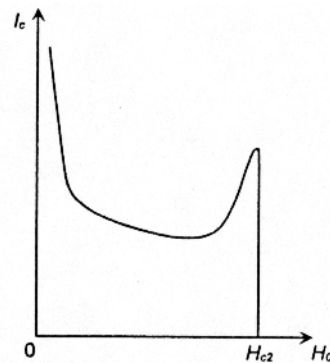


Figure 2.7. Dependence of critical current on perpendicular magnetic field. The pronounced peak effect is observed at H_{c2} [4].

2.4.3 INTERACTION OF VORTICES WITH PINNING CENTERS

Vortices interact with many different types of defects which often lead to large values of the critical current. But not every defect interacts with vortices effectively due to the characteristic size of the vortex. As an example, vacancies, second phase atoms and other similar tiny defects are not effective pinning centers because the size of a vortex (the coherence length) exceeds by far the atomic size. Therefore simply a vortex does not notice these types of defects. Conversely, structural defects with the dimensions on the order of coherence length and larger can be very effective and cause very large critical current densities.

This situation is however different for high-temperature superconductors, because there the coherence length are on the order of point defects!

Among other effective pinning centers in superconductors are dislocations, dislocation walls, grain boundaries and interfaces between superconductors with different parameters.

2.4.4 INTERACTION OF VORTICES WITH THE SURFACE OF A SUPERCONDUCTOR

Let us consider an ideally homogeneous Type II superconductor in the form of a plate of thickness d , which is much larger than the distance between vortices. An external applied field H_0 ($H_{c1} < H_0 < H_{c2}$) is applied parallel to the surface of the plate. The vortices form a triangular lattice in the plate with period $a \ll d$. According to detailed calculations, the distance between the edge of the plate and the nearest vortex row is $\approx a$.

If we pass a small transport current from the plate perpendicular to the field, the current generates a field H_I , and the total field at one side of the plate becomes $H_0 + H_I$ and the other side $H_0 - H_I$. As explained before a stable state with a gradient of vortex density is not possible in a homogeneous superconductor. Therefore in response to the applied current the vortex structure as a whole must shift in the direction of the Lorentz force. As the vortices were in equilibrium before the current was applied, even a very small displacement from their equilibrium position must bring about a restoring force. The result is the elastic shift of the whole vortex lattice by a certain distance determined by the balance between the Lorentz force and the restoring force. If the Lorentz force acting against the restoring force is sufficient enough to shift the vortices by a distance $\approx a$, a continuous flow of vortices will start. When the vortex row reaches the edge, it is annihilated by its image and at the same time, an identical row enters the plate from the opposite side and moves by a distance a and so on. This implies that the transport current shifting the vortex lattice by approximately, a , is the critical current.

As a conclusion for the flow of transport current through a superconducting plate in the mixed state, if the current is well below the critical value, the Lorentz force causes an elastic shift of the vortex structure as a whole by a certain distance $\delta x < a$. As soon as this happens, the Lorentz force is balanced by a restoring force brought about by the shift, and the vortex lattice comes to rest again. The vortex lattice period is the same everywhere; therefore, in the interior of the plate, the current is zero. In other words, the transport current flows within the layer $\approx \lambda$ near the surface.

2.4.5 INTERACTION OF A VORTEX WITH A CAVITY IN A SUPERCONDUCTOR

Consider an infinite superconductor with a defect in the form of a cylindrical cavity, assuming the diameter of the cavity satisfies $d > \xi(T)$, the interaction energy can be easily understood. A vortex with a normal core of diameter $\sim 2\xi$ stores a positive energy relative to the energy of the superconductor without the vortex, because the free energy of the normal state exceeds that of the superconducting state by $H_{c1}^2/8\pi$ per unit volume. Then the energy of the normal core per unit length is:

$$\frac{H_{c1}^2}{8\pi} \times \pi \xi^2 \quad (2.18)$$

Therefore if the vortex is trapped by the cavity, i.e. passed through its interior, it does not have the normal core and accordingly the energy of the system is reduced by the above amount. This implies an attractive interaction between vortices and cavity. The interaction force per unit length f_p can be easily found if we recall that the energy changes by the value of f_p when the vortex changes its position near the edge of the cavity by $\sim \xi$:

$$f_p \approx \frac{H_{c1}^2}{8} \xi \quad (2.19)$$

If instead of cylindrical cavity, the superconductor contains a spherical cavity of diameter d , the pinning force f_{pd} on the vortex can be obtained from:

$$f_{pd} \approx \frac{H_{c1}^2}{8} \xi d \quad (2.20)$$

The above force is quite large and the critical current to tear off the vortices from spherical cavities is of the same order of magnitude as the pair-breaking current. Thus in order to release vortices from spherical voids, one should apply the maximum possible current for a given superconductor. The above reasoning is also valid in the case of a superconductor containing tiny dielectric inclusions. It is also valid at least by the order of magnitude if the inclusions are of a normal metal. Generally various types of normal inclusions, represent effective pinning centers in superconductors.

2.4.6 RESISTIVE STATE

Let us now consider what happens when the Lorentz force due to an applied current exceeds the pinning force and vortex flow in the direction of the applied current. Such a vortex flow as has mentioned before, results in dissipation of energy and a finite electric resistance, therefore this state is known as *Resistive State*. By Faraday's law of electromagnetic induction, a flow magnetic flux generates an electric field E in the same direction as the applied current. This means that energy dissipation Ej_{tr} arises across the bulk of the superconductor.

If we assume the velocity of vortices in the direction of the Lorentz force, that is in the direction perpendicular to both current and magnetic field, is v_L , then the work done by the external source to keep the vortices moving is $F_L v_L$ per unit time, where F_L is the density of the Lorentz force (figure 2.8). Obviously this work is equal to the energy dissipated by the system per unit volume and unit time, that is,

$$F_L v_L = E j_{tr} \quad (2.21)$$

Recalling that $F_L = j_{tr} B / c$, we obtain

$$E = B v_L / c \quad (2.22)$$

The resistivity of a superconductor resulting from the flux flow is referred to as flux-flow resistivity and denoted by ρ_f :

$$\rho_f = E / j_{tr} \quad (2.23)$$

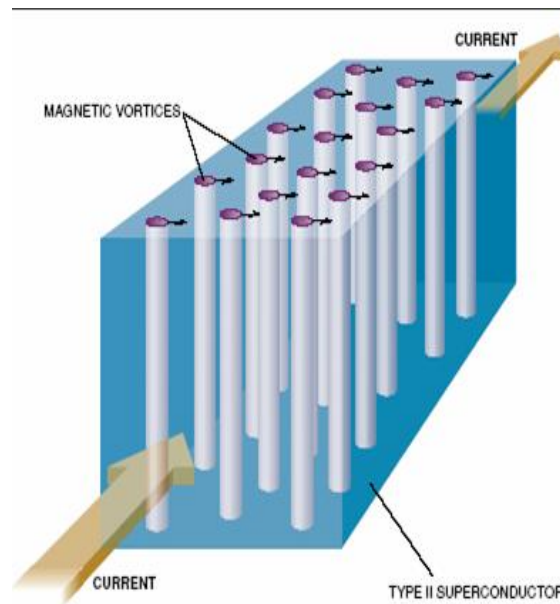


Figure 2.8. Initiation of Lorentz force in a Type II superconductor in the mixed state, when applying a current (Picture courtesy of D. J. Bishop et al., © Scientific American, 48, Feb. 1993).

The fact that the vortex motion is accompanied by dissipation of energy allows us to assume that the vortices move in a viscous medium, and then we can introduce a viscosity coefficient η :

$$f_{friction} = -\eta v_L \quad (2.24)$$

Where $f_{friction}$ is the friction exerted on one vortex moving with the velocity v_L . Neglecting the vortex mass, the stationary movement of the vortex is in the form

$$f_{friction} + F_L = 0 \quad (2.25)$$

After substituting the relevant expressions for the forces per unit volume, this equation becomes

$$\frac{B}{\Phi_0} \eta v_L = \frac{1}{c} B j_{tr} \quad (2.26)$$

By using (2.22) and (2.23) we can rewrite the above equation as:

$$\rho_f = \frac{\Phi_0 B}{c^2 \eta} \quad (2.27)$$

Then if η is independent of magnetic field, the resistivity ρ_f of the superconductor is a linear function of B .

A typical current-voltage characteristic of a superconductor in a resistive state is shown below

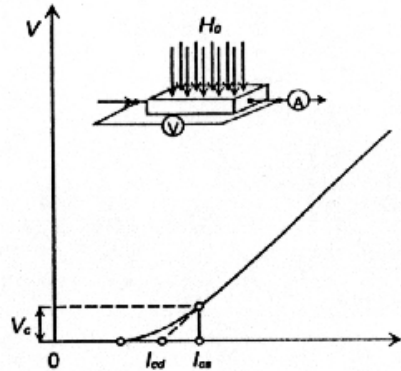


Figure 2.9. Current-Voltage characteristic of a superconductor containing pinning centers. I_{cs} and I_{cd} illustrated in the image are the two ways of determining the critical current [4].

As it is shown, a finite voltage appears at a certain value of current (the critical current) and also at small values of the voltage, the characteristic is non-linear. The non-linear part corresponds to a flow of vortices that is not yet stabilized, that is to flux creep, where the vortices jump randomly from one pinning center to another. As the current is increased further, the current-voltage characteristic becomes linear, where the linear part corresponds to

the flow of the vortex structure as a whole. There are two ways to define the critical current on an I - V characteristic. The current I_{cs} (the minimum current giving rise to a finite voltage) is the static critical current. At I_{cs} , the process of vortex break-off from pinning centers begin. However, the exact value of I_{cs} is difficult to determine because it depends on the actual value of the voltage that is assumed to correspond to the critical current (A 10^{-6} V threshold is applied in the majority of technical applications, i.e. a current that gives rise to a 10^{-6} V voltage is taken as the critical current).

The second definition of the critical current is I_{cd} , the dynamic critical current which is obtained by extrapolating the linear part of the current-voltage characteristic until it intersects the I -axis.

2.5 FERROMAGNETISM

2.5.1 INTRODUCTION

Ferromagnetic materials are defined as materials which exhibit spontaneous magnetization even in the absence of an external field. This behavior of course is observed below a critical temperature, called Curie temperature, T_C . Above the Curie temperature, thermal fluctuations disrupt the regular arrangement of magnetic moments and electron spins is vanished resulting in the loss of magnetization. Below the Curie temperature, the electron spins lose their randomness and by choosing a particular direction which is correlated over a macroscopically large area, the system attains a net magnetic moment.

In microscopic scale, the exchange energy in ferromagnet materials produces a spin-split of the electrons in the energy band near the Fermi surface. In other words, the splitting of energy bands to minority and majority spins which is caused by exchange interaction, causes some states with down-spin near the Fermi surface to be occupied whereas states with up-spin, unoccupied. This initially seems to be energetically unfavorable; however, according to the molecular field theory the interaction of magnetization with molecular field gives the energy reduction which outweighs this increase in energy.

2.5.2 ENERGY OF MAGNETIC MATERIALS

The total energy of a ferromagnetic material is composed of dipolar or magnetostatic energy, exchange energy, magnetocrystalline anisotropy energy and Zeeman energy. $E_{dipolar}$ which is sometimes called demagnetization or magnetostatic energy is the energy due to free poles of the ferromagnet at the surface or boundaries. These cause a demagnetizing field H_d inside of a magnetized material of finite dimensions. It can be detected during hysteresis measurements of short length samples when the applied field is reduced to zero but the measured field is

negative due to remanent magnetization. It is called demagnetizing field because it opposes the magnetization direction. The demagnetizing field depends on two factors only; magnetization (i.e. pole strength) and shape of the specimen (i.e. pole separation determined by sample geometry). It is proportional to magnetization and thus depends on applied field, as

$$H_d(H_{appl}) = -N_d M(H_{appl}) \quad (2.28)$$

where N_d is the demagnetizing factor calculated solely from the sample geometry. The demagnetizing field is not uniform inside the sample unless it has an ellipsoidal shape or for example in a thin film, far from the edges, where the field is mostly uniform.

The increase in energy due to domain wall formation $E_{exchange}$ is a direct consequence of the exchange interaction between neighboring magnetic moments. $E_{magnetocrystalline}$ describes the preference of the magnetization to be oriented along certain crystallographic directions (magnetocrystalline anisotropy) due to the spin orbit interaction. The magnetoelastic energy term $E_{magnetoelastic}$, part of the magnetocrystalline anisotropy, arises due to strains. Finally the Zeeman energy term E_{zeeman} is the increase in energy of a magnet in an applied field given by the expression;

$$E_{Zeeman} = -M.H \quad (2.29)$$

2.5.3 DOMAIN WALLS

Below the Curie temperature, a ferromagnetic material is made of magnetic Domains, small regions with constant magnetization. The reason for formation of the domains is that it is energetically favorable and reduces the energy of the system. The domain size and relative orientation depends on factors such as dipolar or magnetostatic interaction, surface area of the domain wall, exchange field and magnetocrystalline-magnetoelastic anisotropy. If we place a ferromagnet in an increasingly large magnetic field, the magnetization direction of each domain will rotate to align with the direction of the field and those domains oriented favorably to the applied field increase at the expense of those domains unfavorably oriented to the applied field. The interface or separation between domains is called the domain wall. In these regions the magnetization and the exchange field point in different directions. The change in the direction can not be abrupt because otherwise the exchange energy between two adjacent spins would be very large. In order to minimize the exchange energy the change is gradual so that the angle between adjacent spins has a small value. On the other hand if the spins within the wall point in a non-easy direction, due to crystal anisotropy, then the anisotropy energy is higher within the wall than at the domains. Thus the anisotropy energy tries to make the wall thin while the exchange energy tries to make the wall as wide as

possible in order to make the angle between adjacent spins small. As a consequence of this competition the wall has a finite width and a certain structure.

BIBLIOGRAPHY

- [1] H. Kamerlingh Onnes, *Leiden Comm.* 122b, **124** (1911).
- [2] W. Meissner and R. Ochsenfeld, *Naturwissenschaften*, **21**, 787 (1933).
- [3] A. M. Campbell and J. E. Evetts, "*Critical currents in superconductors*", (Taylor & Francis Ltd. London 1972).
- [4] V. V. Schmidt; P. Muller, A. V. Ustinov (eds) "*The Physics of Superconductors: Introduction to Fundamentals and Applications*" (Springer, Germany, 1997)
- [5] M. Tinkham, *Introduction to Superconductivity*, (McGraw-Hill, 1996).
- [6] J.R. Waldram, *Superconductivity of Metals and Cuprates*, (Institute of Physics Publishing, 1996).
- [7] C. Kittel, *Introduction to Solid State Physics*, (John Wiley and Son's, 1996).
- [8] S. Chikazumi, *Physics of Ferromagnetism*, 2 ed. (Oxford Science Publications, 1997).
- [9] D. Jiles, *Introduction to Magnetism and Magnetic Materials*, 2 ed. (Chapman and Hall, 1998).
- [10] B. D. Cullity, *Introduction to Magnetic Materials*, (Addison Wesley 1972).



*New ideas pass through three periods: *It can't be done. *It probably can be done, but it's not worth doing *I knew it was a good idea all along!*

Arthur C. Clarke

3.1 THIN FILM DEPOSITION

3.1.1 SPUTTER DEPOSITION TECHNIQUE

Sputter deposition, along with evaporation techniques are categorized as Physical Vapor Deposition (PVD). PVD involves the generation of a vapor source and transport of the vapor species to a substrate. In evaporation techniques, the vapor source is produced by thermal means, whereas in sputtering atoms are removed from the source through impact of energetic ions via momentum transfer.

After its first discovery in 1852 by Grove [1] and further development as a thin-film deposition technique by Langmuir [2] in the 1920's, it has become a widely used technique in both industry and research. The reason is besides being absolutely versatile technique, a wide range of materials can be deposited from either single element, composite, alloy or compound targets in many different geometries. The process can be easily automated or scaled up and the equipment cost is relatively low. Films used for magnetic and microelectronic applications often require stoichiometric alloys, which must conformally cover and adhere well to the substrates. These requirements have made sputtering (as well as chemical vapor deposition (CVD)) the technique of choice for most silicon-based technologies.

3.1.2 SPUTTER DEPOSITION MECHANISM

A schematic diagram of a sputtering system is shown in figure 3.1. The target is mounted on the magnetrons and, consists of a plate of the material to be deposited.

The magnetron hence, the target are then connected to the negative terminal of the power supply so that the magnetron or the target acts as the cathode. The body of the sputtering chamber and the substrates (because they are connected to each other), are earthed and therefore act as anode. The chamber is evacuated from air until ultra high vacuum condition is reached, and is filled with low-pressure sputtering gas (normally Argon). Once the argon gas is introduced inside the chamber, a large enough voltage is applied between the cathode and anode so that breakdown field of the gas is exceeded, creating a large number of ions and electrons. Therefore, the Ar ions possessing positive charge, accelerate towards the negatively charged target (magnetron) and bombard the target so the plasma will be initiated and sustained. This results in momentum transfer to surface atoms and a chain of collision events occurs, resulting in the ejection of target atoms, secondary electrons and reflected neutrals (neutralized argon ions) (figure 3.2).

The sputtered flux is scattered by the sputtering gas and so species arrive at the substrates at a range of angles, so good step coverage is achieved. Ions with very low energy will simply bounce off the surface. At energies less than about 10 eV, the ion may adsorb to the surface, giving up its energy to phonons (heat). At energies above about 10 eV, the ion penetrates into the material, transferring most of its energy deep into the target, where it changes the physical structure. These energies are typical for ion implantation. Between these two extremes, both energy transfer mechanisms occur; part of the ion energy is deposited in the form of heat, and the remainder goes into the physical rearrangement of the target material. Most of the energy transfer occurs within several atomic layers, and the atoms and clusters of atoms are ejected from the surface of the material.

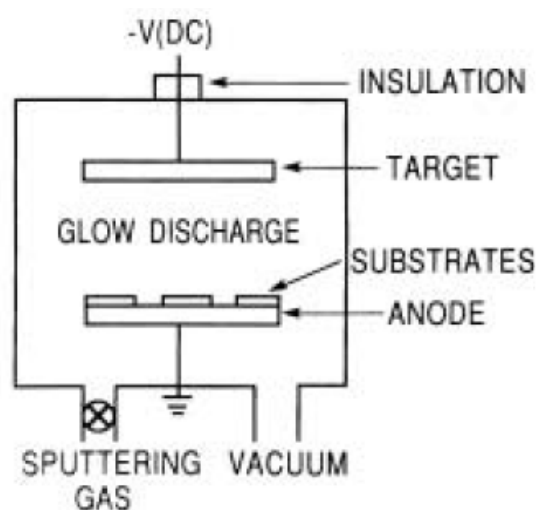


Figure 3.1. A schematic diagram of a dc sputtering system is shown [3].

The sputtered atoms escape with energies of typically 10 to 50 eV, which is about 100 times the energy of evaporated atoms. This results in energetic bombardment of the growing film and various processes can therefore occur, such as resputtering of impurities or atomic species which have only been physically adsorbed, or even forward sputtering can occur, where an atom collides with an atom on the film surface and knocks it into a different site, which enables more conformal coverage.

Also as the sputtered species bombarding the substrate carry high energies, ion implantation can occur if the reflected neutrals are incorporated into the depth of the substrate. Furthermore, defects can form during film growth because of the stress accumulated in the microstructure of the sputtered film.

The secondary electrons that are ejected from the target are accelerated away from the cathode and those that have sufficient energy will ionize neutral gas atoms, hence sustaining the plasma.

This region is known as the “negative glow”. In between this region and the cathode is the Crookes dark space where nearly all of the applied voltage is dropped.

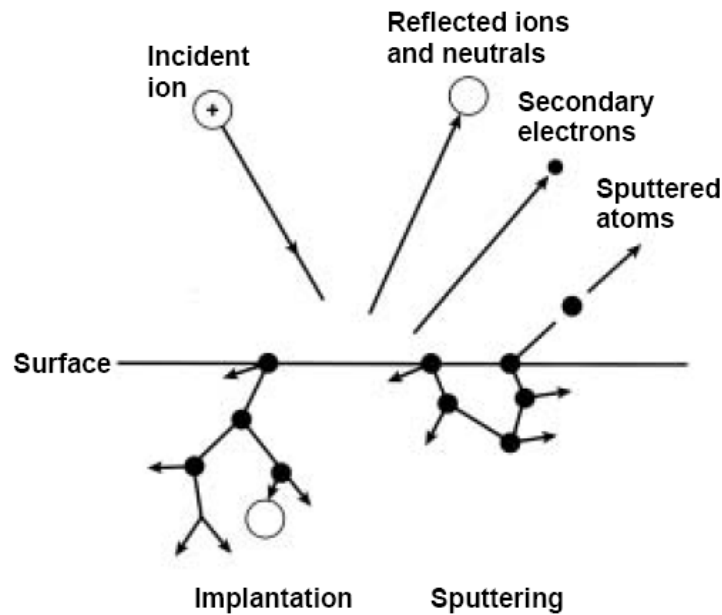


Figure.3.2. The interaction of incident ion with the sputtering target is shown [4].

The sputter yield, S is an important parameter in sputtering and is defined as the number of ejected particles per incident ion. It is a measure of the efficiency of sputtering and so for an incoming ion of incident energy, $E_i < 1keV$,

$$S = \frac{3\alpha}{4\pi^2} \frac{E_t E_i}{U} \quad (3.1)$$

Where E_t is the energy transfer function (derived from the theory of elastic binary collisions), U is the sublimation energy of the target material and α is a measure of the efficiency of momentum transfer in collisions. To obtain a quick estimate of S , the following approximation is often used

$$S \propto \frac{M_t}{T_m} \quad (3.2)$$

Where M_t is the mass of the target atom and T_m is the melting point of the target material.

3.1.3 TYPES OF SPUTTERING TECHNIQUES

3.1.3.3 DIRECT CURRENT (DC) SPUTTERING

The mechanism just explained for sputtering was actually based on dc sputtering. Sputtering techniques are used because of their high attainable deposition rate and therefore deposition rate is one of the most important parameters. Three main parameters affecting the deposition rate are sputtering gas pressure, target power and target-substrate distance.

If the sputtering pressure is too low, then produced sputtering gas ions are far from the targets and might hit the chamber walls and lost before reaching the targets. Also as the mean free path of the electrons is large, the ionization rate of the sputtering gas ions will be low and the plasma can not sustain and dies. On the other hand, if the sputtering gas pressure is too high, then there is a probability that the sputtered atoms undergo a lot of collisions and therefore never make it to the substrate. Therefore it's a kind of a compromise to determine the optimum sputtering parameters. Due to the high energy of incident ions, much of the energy is wasted as heat in the targets. Therefore a water cooling system for the targets during sputtering should be provided. In general it is found that

$$\text{Depositon Rate} \propto \frac{cW}{d_2} \quad (3.3)$$

Where c is a constant and W is the power applied to the target. Therefore simple dc-glow discharge sputtering is a fairly inefficient process because it is dependent on the rate of argon ions bombarding the target and the rate of ejected target atoms reaching the substrate. There are various ways to improve the efficiency, and one of the most commonly employed techniques is magnetron sputtering.

3.1.3.4 MAGNETRON SPUTTERING

In this context only planar magnetron is considered, although there are different configurations (e.g. toroidal, toroidal-conical and cylindrical) depending on the sputtering geometry required. The magnetron basically consists of an iron block with a cavity in the centre in which there is a copper/aluminium spacer and a very strong permanent magnet such as SmCo_5 . The iron block is attached to a copper backing plate and there is a water inlet and outlet to cool the magnetron.

The magnetic field lines are initially normal to the target, then bend with a component parallel to the target surface (this is the magnetron component) and return into the target, completing the magnetic circuit. During sputtering, there is an electric field E acting perpendicular to the target surface and a magnetic field oriented parallel to the target surface, as shown in figure

3.3. The Lorentz force describes how an electron would behave in crossed magnetic and electric fields.

$$F = m \frac{dv}{dt} = -q(E + v \times B) \quad (3.4)$$

Where q , m and v are the electron's charge, mass and velocity, respectively.

An electron emitted from the cathode would be accelerated towards the anode but on experiencing the region of the parallel magnetic field is bent back towards the target because of the Lorentz force which causes the electrons to spiral around the direction of the magnetic field lines. It therefore executes a cycloidal motion, which means that electrons are trapped near the target surface, increasing the collision probability with a gas atom. This leads to larger currents and increased deposition rates.

The plasma can be sustained at a lower pressure; typically 10^{-5} to 10^{-3} Torr so there is a larger pressure range in which sputtering can occur.

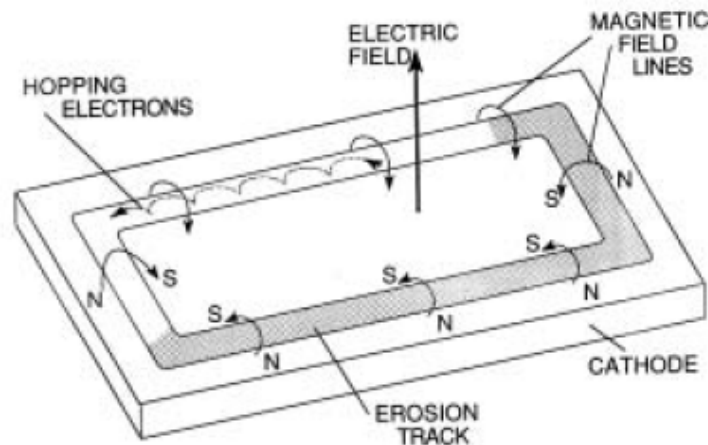


Figure 3.3. The plan view of a planar magnetron is shown [3].

Magnetron sputtering is the most popular sputtering method because of the high deposition rates attainable (e.g. up to $1 \mu\text{m}/\text{min}$). This is about an order of magnitude higher than conventional sputtering techniques.

3.1.3.5 RADIO FREQUENCY (RF) SPUTTERING

This was developed to deposit insulating films. A high frequency AC power supply is employed. RF frequencies in the range of 5 to 30 MHz are used although 13.56 MHz is the most common. The target develops a negative potential because electrons are more mobile than ions and once this has occurred it resembles a dc target. Oscillating electrons acquire enough energy to ionize the argon molecules, so we are no longer reliant on secondary electrons to sustain the discharge. Therefore, the discharge can be maintained at lower

pressures and for this reason RF sputtering is sometimes used for conducting targets. RF voltages can be coupled through any impedance so insulating targets are possible. Oxides and even polymers can be sputtered in this way.

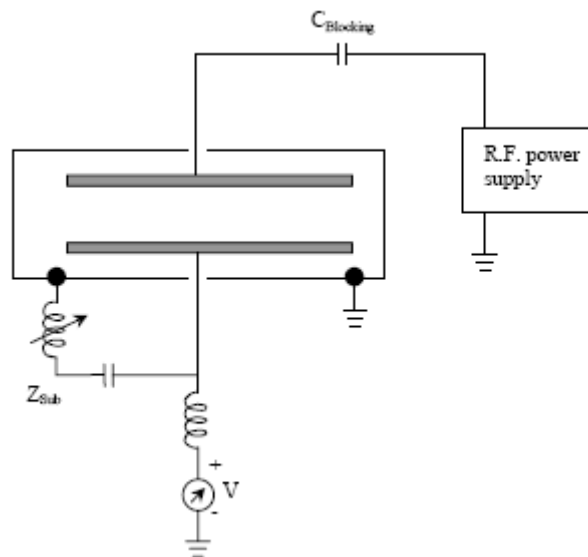


Figure 3.4. A schematic diagram of an R.F. plasma system is shown [4].

3.2 FILM DEPOSITION EXPERIMENTAL RUNS

3.2.1 SUBSTRATE PREPARATION

All the films were deposited on *c-plane* Sapphire ($11\bar{2}0$) with 0.7 mm thickness, which were cut into $4 \times 4 \text{ mm}^2$ for the VSM samples and $5 \times 10 \text{ mm}^2$ for XRD work. The substrates were cut with a diamond edged circular saw. They were first mounted on a glass slide using wax to avoid any movement during cutting. Care has to be taken since sapphire is very brittle and so the rotating blade is set to move slowly across the wafer in order to prevent substrate chipping. After cutting, the substrate were heated and then bathed ultrasonically in Chloroform for at least 20 minutes to remove wax and other contaminants. The substrates were then cleaned ultrasonically in Acetone for about 20 minutes, which then finally followed by 5 minutes of wash in Isopropanol. They were then dried using an air gun (which uses a clean air source). Prior to loading into the sputter deposition, they were cleaned with nitrogen air gun with Acetone followed by Isopropanol in order to assure there were no contaminants on the substrate surface.

3.2.2 CO-SPUTTERING OF NIOBIUM AND GADOLINIUM

Thin film samples were deposited using *Cambridge Device Materials Mark III* sputter deposition system. Mark III is an Ultra High Vacuum (UHV) deposition system capable of sputtering from multiple magnetrons simultaneously. Direct current (DC) magnetron sputtering technique was chosen because of its advantageous and simplicity over other methods (refer to section 3.1.3.3). A schematic of Mark III sputtering system is shown in figure 3.5.

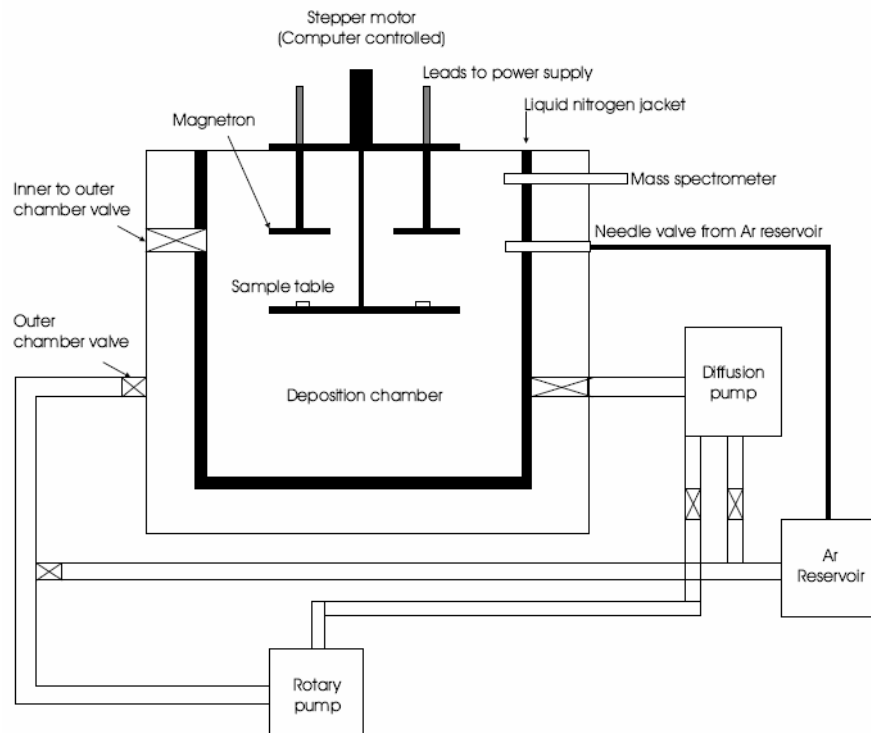


Figure 3.5 A schematic of Cambridge Mark III Ultra High Vacuum sputter deposition system. (Image Courtesy of J. Robinson)

The chamber consists of an inner and outer chamber with a nitrogen jacket in between. The film deposition takes place in the inner chamber. The cleaned substrates are placed on a substrate tray which stays under the Nb and Gd magnetrons in order to have a range of different compositions of niobium and gadolinium on substrates. A schematic of the sputtering flange arrangement used in this experiment is shown in figure 3.6.

Before running the experiment, the system must put in vacuum. The Ultra High vacuum (UHV) condition in the chamber is achieved in two stages. First a rotary pump is used which only achieves rough vacuum. An ultra high vacuum is achieved using the diffusion pump. The rotary pump is also used for backing the diffusion pump as well. The system is left for pumping overnight and at the same time is also baked at 423 °K for 8 hours in order to remove the remaining water from the system. Because of its intermediate adsorption energy, it is difficult to remove all the water from the system. Outgassing species with high adsorption energies such as inert gases are easy to remove from the system because they desorb rapidly and pumped away easily.

The photographs of the Mark III sputtering system and the flange used in this experiment are shown in figures 3.7 and 3.8 respectively.

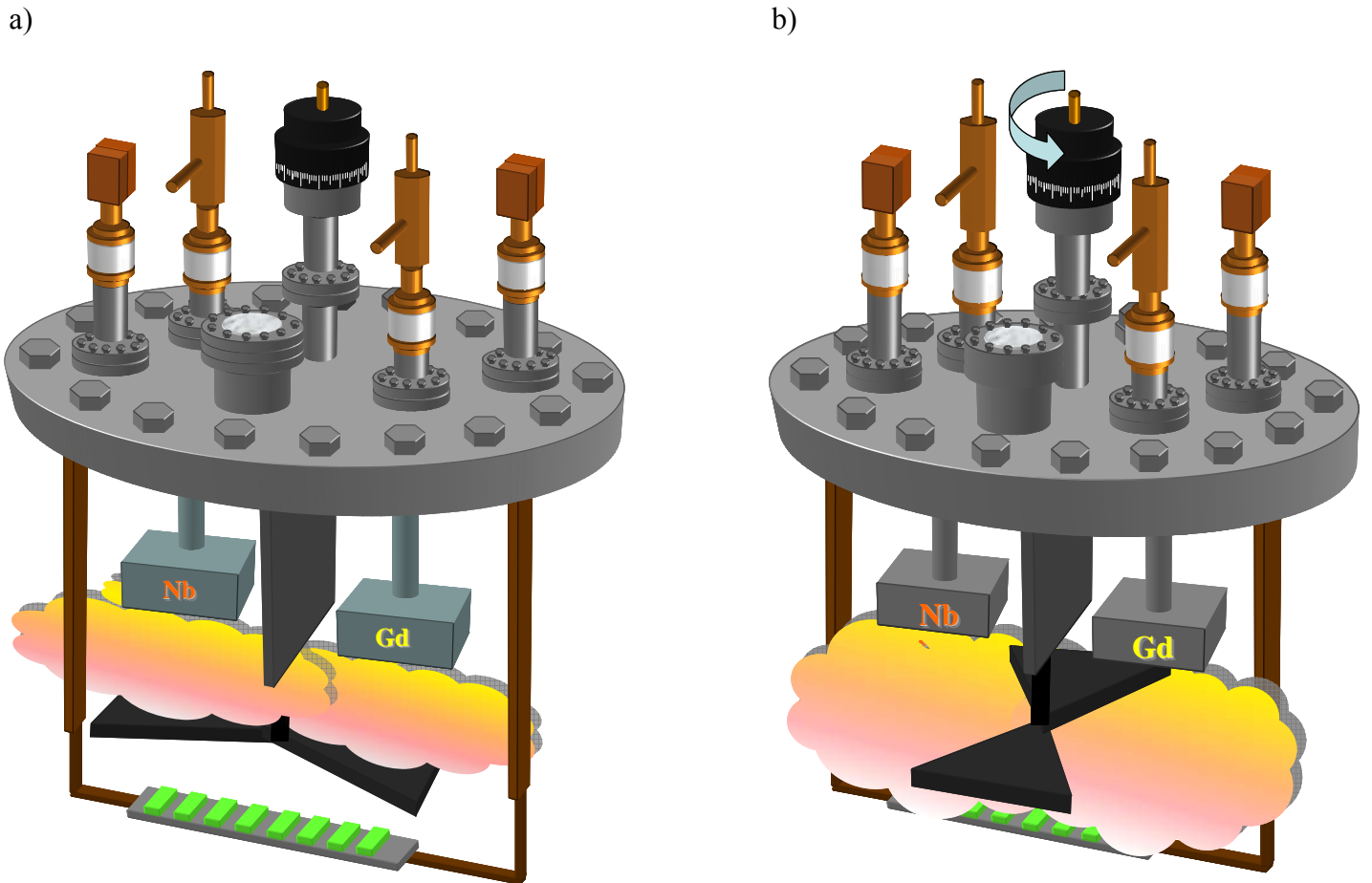


Figure 3.6. Schematic of the sputtering flange used in this experiment. a) shutter closed. b) shutter open. (Images prepared by the author)

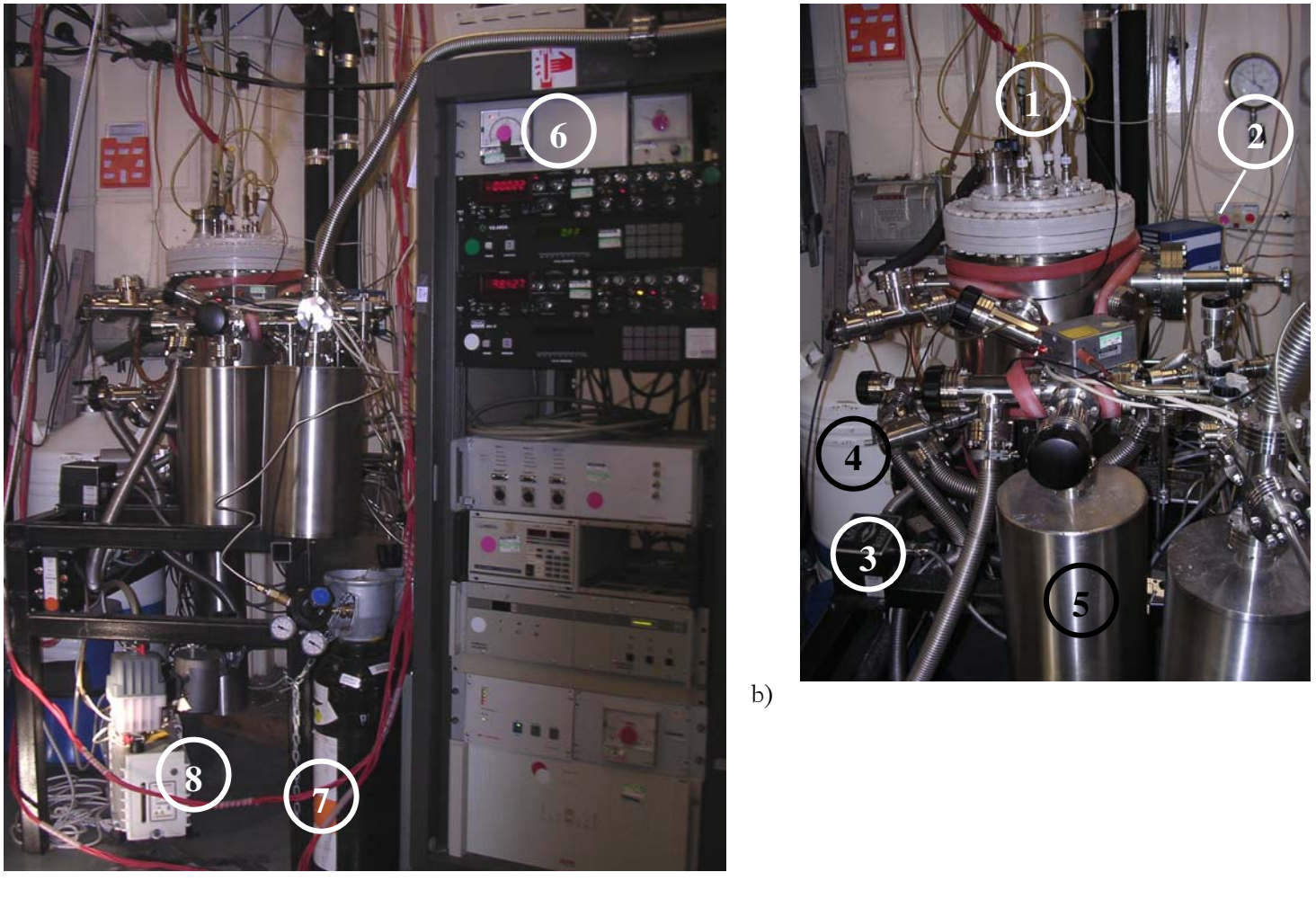


Figure 3.7. The photographs of MKVII sputtering system during experiment with flange installed. (a) is the whole system along with electrical controllers and (b) is the enlarged photo of the sputtering chamber. 1) Sputtering flange installed. 2) Mass spectrometer. 3) Baratron (pressure gauge). 4) Liquid He dewar. 5) Argon gas reservoir. 6) Pressure gauge indicators (Baratron, Pirani, Mass spectrometer). 7) Argon gas cylinder. 8) Rotary pump.

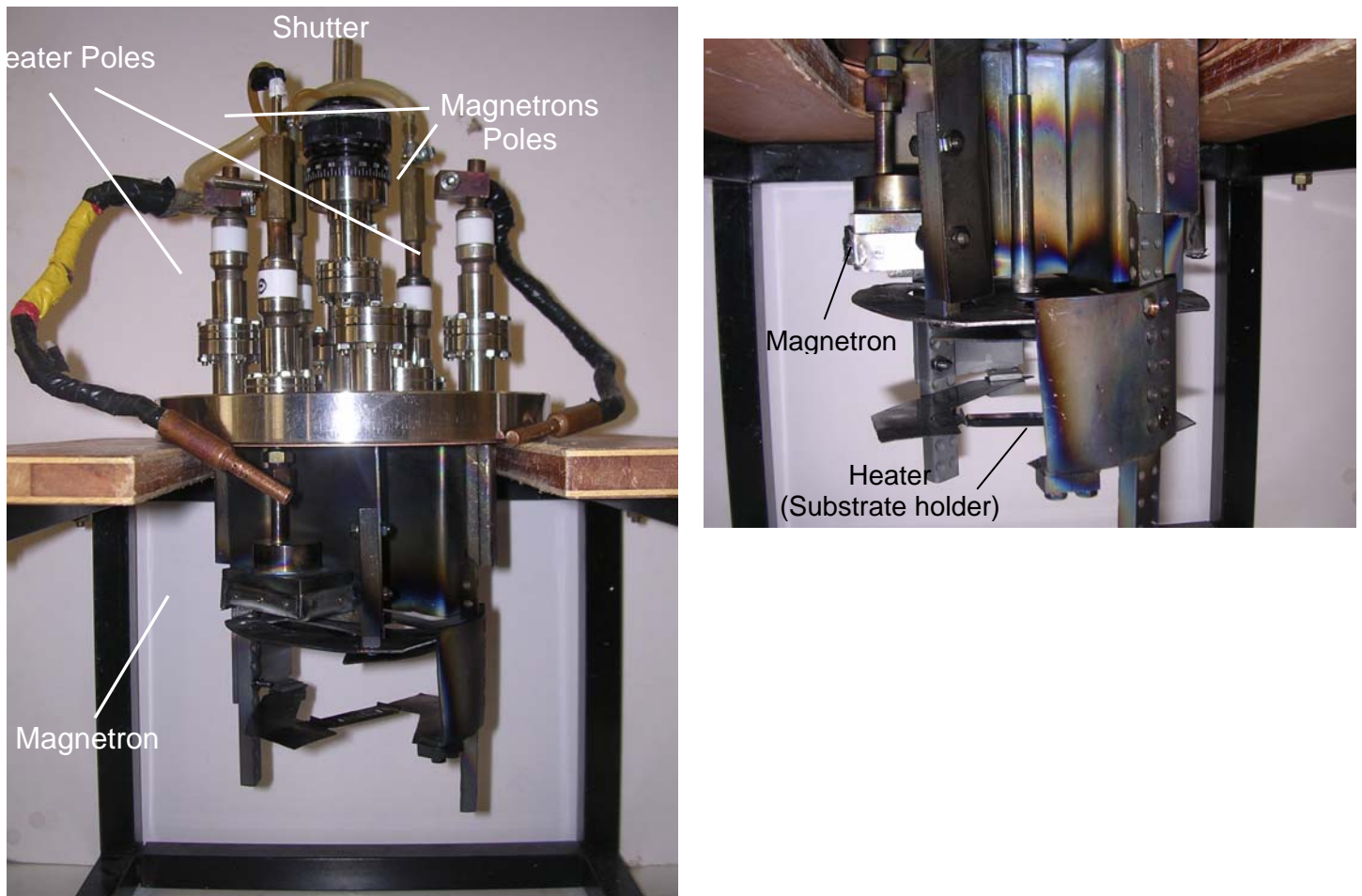


Figure 3.8. Photographs of the flange used in this project.

It is important after a bake-out to check that there are no leaks. In order to detect large leaks, the gate valve can be closed and the chamber pressure should be observed using the baratron. If the pressure is steady, there is no leak. If the pressure is rising, then one can determine whether it is gas leakage or outgassing from the chamber walls, by recording the pressure rise with time. Gas leakage causes a linear rise with pressure, whereas outgassing results in a pressure rise that becomes gradually smaller and tends to a limiting value. A typical base pressure obtained after a bake out is 1×10^{-6} Pa which is measured by the Mass Spectrometer. The mass spectrometer is also capable of measuring partial pressures of components such as oxygen, nitrogen and water. Therefore another way to check whether there is an air leakage in the system or not is to check the ratio of nitrogen to oxygen. If this ratio is 4:1 then there is definitely a leakage in the system.

The next step to further improve the vacuum of the system is to fill the nitrogen jacket with liquid nitrogen and let the system cool down for about three hours to freeze the remaining gaseous impurities on the chamber walls. This will further improve the base pressure of the system to better than 5×10^{-7} Pa and ensures a high quality vacuum with least contaminations. The argon (Ar) gas supply has purity of 99.9999%. In order to introduce Ar gas into the

chamber, a reservoir is first filled with Ar to about 50 kPa, from which it is connected to the chamber via a needle valve. The partial Ar pressure used for this experiment for deposition of films was 0.9 ± 0.05 Pa. For initiation of the plasma, a pressure of 10 Pa is required which of course is then reduced to the pressure considered for sputtering. This stage is called pre-sputtering during which the shutter is closed to avoid any coating on the substrates. It also helps to remove any surface contamination such as oxides from the target surface and to cover the surrounding area in the chamber so that the impurities from the chamber walls are not sputtered on the substrates. The flange in this experiment consisted of two magnetrons with one empty slot. The magnetrons were cooled by water in order to minimize the heating of the targets during sputtering. Also stainless steel shieldings were mounted between magnetrons to prevent cross-contamination of the sputter fluxes of the targets during sputtering. The heater consisted of a tantalum (Ta) foil through which a constant dc current is passed via low resistive copper poles. By adjusting the amount of the current, the temperature of the heater could be set. One way to calibrate the temperature is by using a pyrometer and trying to match the color of the filament to heater. In the flange used in this experiment, the window was too opaque and could not be seen through, therefore knowing the dimension of the heater (60mm×14mm); the temperature was approximated by comparing with the graphs provided by some extensive experimental work done before in the group¹. For 50A current passing through the heater, the temperature was approximated to be 1100 °C and generally a linear relationship between the applied current and the heater temperature has been found experimentally. Of course one has to bear in mind that the mentioned temperature, are for the heater foil and the temperature of the substrates are lower than this temperature because of the radiation losses. A 20% of temperature loss due to radiation was found to be reasonable for estimating the substrate temperature.

In the preliminary runs, for setting the power of the magnetrons accurately and having an estimate of the deposition rates and before running a calibration run for each target, a set of calculations were done according to the data provided in reference 5.

¹ These unpublished experiments have been carried out by Z. Barber, Department of Materials Science and Metallurgy, University of Cambridge.

According to 3.3, the deposition rate for each element follows

$$S \propto \frac{M_t}{T_m}$$

Where M_t is the molecular mass and T_m is the melting point of the element.

Therefore,

$$\left. \begin{array}{l} \text{Nb: } \left\{ \begin{array}{l} \text{Atomic weight} = 92.90 \\ T_m = 2740.05 \text{ K} \\ T_b = 5014.85 \text{ K} \end{array} \right. \Rightarrow D.R_{Nb} = 0.0251C \text{ nm/sec. Watt} \\ \text{Gd: } \left\{ \begin{array}{l} \text{Atomic weight} = 157.25 \\ T_m = 1585.85 \text{ K} \\ T_b = 3538.85 \text{ K} \end{array} \right. \Rightarrow D.R_{Nb} = 0.0664C \text{ nm/sec. Watt} \end{array} \right\} \Rightarrow \frac{D.R_{Gd}}{D.R_{Nb}} = 2.6455$$

According to the set of experiments which has been performed in reference 5 :

$$\text{For Pure Nb@} \left\{ \begin{array}{l} \text{Power} = 50W \\ d = 70mm \end{array} \right. \Rightarrow D.R_{Nb} = 0.2 \text{ nm/sec} \Rightarrow D.R_{Gd} @ \left\{ \begin{array}{l} \text{Power} = 50W \\ d = 70mm \end{array} \right. = 0.53 \text{ nm/sec}$$

But in the flange used in this project, $d = 85mm$ & $P = 30W$, Therefore

$$D.R_{Nb} = 0.2 \text{ nm/sec} \times \left(\frac{30}{50}\right) \times \left(\frac{70}{85}\right)^2 = 0.0814 \text{ nm/sec}$$

$$D.R_{Gd} = 0.53 \text{ nm/sec} \times \left(\frac{4.95}{50}\right) \times \left(\frac{70}{85}\right)^2 = 0.0356 \text{ nm/sec}$$

These deposition rates were employed in preliminary runs; however, the Deposition Rate of Nb was modified according to the D.R. measured from the step in the calibration sample (Set 4, Run # 21244):

$$D.R_{Nb} = 0.0917 \text{ nm/sec} \quad \& \quad \frac{D.R_{Gd}}{D.R_{Nb}} = 2.6455 \quad \& \quad Power_{Gd} = 4.95 \text{ W}$$



$$D.R_{Gd} = 0.0917 \times 2.6455 \times \left(\frac{4.95W}{30W}\right) \Rightarrow D.R_{Gd} = 0.04 \text{ nm/sec}$$

It is then possible to estimate the chemical composition of the film by stipulating the fact that the amount of material sitting on the substrate is linearly dependant to the deposition rates. For a 30 min deposition for example:

$$t = 30 \text{ min} \Rightarrow \begin{cases} \% Nb = \frac{0.0917 \times 25 \times 60}{(0.0917 \times 25 \times 60 + 0.04 \times 25 \times 60)} \times 100 = 69.63\% \\ \% Gd = \frac{0.04 \times 25 \times 60}{(0.04 \times 25 \times 60 + 0.0917 \times 25 \times 60)} \times 100 = 30.37\% \end{cases}$$

As the deposition was carried out from both targets simultaneously, the only way to predict the thickness of the film is to consider the deposition from each target independent of the other (like multilayers), i.e. contribution of each target to the total thickness is the multiplication of its deposition rate and deposition time. For example for a 25min deposition run, the estimated thickness is:

$$\text{Estimated average Thickness} : 0.0917 \text{ nm/sec} \times (25 \times 60) + 0.04 \text{ nm/sec} \times (25 \times 60) = th(\text{nm}) \Rightarrow th = 197 \text{ nm}$$

The calculated chemical composition and thicknesses, showed to be in good agreement with the measured values.

The simultaneous deposition rate of both niobium and gadolinium for estimating the thickness is found by measuring the thickness of one of the nanocomposite films with for example FIB (explained in section 3.2.3) for high accuracy as:

$$\text{Average thickness of the film} = 310 \text{ nm} \Rightarrow \text{D.R.}_{\text{Nb \& Gd Simultaneously}} = \frac{310 \text{ nm}}{35 \times 60 \text{ sec}} = 0.148 \text{ nm/sec}$$

Details of all the sputtering experiments are listed in Table 3.1.

Table 3.1. Details of all the sputtering experiments.

Set	Run No.	Magnetron Power (W)		Deposition Rate (nm/sec)		Sputter Time (min)	Sputtering Pressure (Pa)	Heater Spec.		Substrate Temp.(°C) Approx.	Thickness (nm)	Base Pressure (mbar)
		Nb	Gd	Nb	Gd			I(A)	V(v)			
1	# 21219	42.75	7.20	0.1160	0.0518	18	1.9	48	3.1	880	180	8.14E-9
2	# 21227	30	5.01	0.0814	0.04	25	0.85	53	3.03	980	200	3.98E-8
3	# 21231	30.1	5.06	0.0814	0.04	30	0.92	56	2.73	1080	266	2.28E-8
4	# 21244	3.04	-	0.0814	-	40	1.22	-	-	-	220	5.55E-9
5	# 21245	29.37	5.03	0.0917	0.04	25	0.95	59	2.25	1180	310	2.28E-8
6	# 21261	29.66	4.09	0.0917	0.04	25	0.93	56	2.49	1080	120	2.46E-8
7	# 21273	29.81	5.13	0.0917	0.04	25	0.95	56	2.26	1080	153	2.7E-8
8	# 21284	29.92	4.25	0.0917	0.04	25	0.95	56	2.29	1080	197	2.45E-8
9	# 21286	29.83	4.90	0.0917	0.04	20	0.95	56	2.60	1080	158	2.3E-8
10	# 21291	30.01	4.90	0.0917	0.04	20	0.95	56	2.60	1080	162	5.2E-8
11	# 21301	29.94	5.03	0.0917	0.04	25	0.96	56	5.57	1100	197	2.3E-8
12	# 21309	30.03	5.01	0.0917	0.04	25	0.96	53	4.89	1000	210	3.32E-8
13	# 21311	29.94	-	0.0917	-	20	0.97	-	-	-	-	2.08E-8
14	# 21315	30.10	5.21	0.0917	0.04	25	0.94	60	6.64	1300	-	2.4E-8
15	# 21318	-	5.54	-	0.04	30	0.98	-	-	-	-	3.9E-8
16	# 21325	30.00	(Mo) 4.9	-	-	35	0.97	60	6.61	1200	-	2.74E-8
17	# 213	-	5.04	-	0.04	60	1	60	6.65	1200	-	2.23E-8
18	# 213	29.92	5.24	0.0917	0.04	30	0.96	62	8.19	1300	275	4.15E-9
19	# 21348	29.96	4.88	0.0917	0.04	25	0.95	56	6.39	1100	30 (buffer)+ 146 nm	9.14E-10
20	# 21349	30.07	4.96	0.0917	0.04	14+45	0.97	56	6.57	1100	80 (buffer) + -	5.88E-9
21	# 21366	30.02	4.84	0.0917	0.04	18+29	0.96	40	4.44	800	100 (buffer) + -	3.49E-8
22	# 21370	30.09	4.92	0.0917	0.04	18+30	0.95	35	3.8	750	100 (buffer) + 170 (film)	2.51E-10
23	# 21377	30.12	-	0.0917	-	25	0.95	35	3.8	750	130	-
24	# 21383	30.77	4.98	0.0917	0.04	19+30	0.97	31	3.16	700	100 (buffer) + 170 (film)	9.8E-8

3.2.3 THICKNESS MEASUREMENT

Three methods were used for measuring the film thicknesses. The usual way is to wrap a strip of *Ta* or *Al* (depending on the deposition temperature) across the substrate so that no deposition occurs there. Then after the deposition, by removing the strip, a step is remained which can be measured with a Dek-Tak 6M Profilometer. This is basically a stylus with a diamond tip that traverses across the step and the vertical downward movement of the tip at the step corresponds to the thickness of the film. The accuracy of the profilometer is ± 5 nm.

For more accurate work, and especially for thickness calibrations, a step was defined by lithographic technique prior to deposition. First 2 μm of Hoechst AZ1529 resist was spun onto the chip and baked for one minute at 100 °C. The chip was then exposed to UV light through a negative mask of the contact pad pattern, using a projection lithography system. As fine features are not required in this process the resist was over exposed (4 minutes) to ensure that the developer was easily removed. Once exposed the pattern was developed in a 4:1 diluted proprietary developer solution for about 20 s. Then it was visually checked so see if all the resist has been removed. Of course careful check was done under the microscope in order to assure that all the resist has been removed. Of course in the calibration runs the bake out could not be done because the photoresist degrades above 423 °K. After the deposition, the film was washed ultrasonically in Acetone so that the photoresist layer (with the deposited film on it) was washed away (Lift-off process) and again a step was remained that could be measured using an AFM. The accuracy of this method is within 1 nm.

The most accurate way and of course the most expensive one is to use Focused Ion Beam for thickness measurement. FIB is capable of both chopping the sample and imaging the microstructure which enables a kind of in-situ thickness measurement based on the condition that different layers have different contrasts (different secondary electron coefficients). In this experiment, sapphire was used as substrate and since it is an insulator, there was no problem of contrast as it appeared dark in the images. Thickness measurement with FIB was done on calibration samples because of their importance and also for checking the consistency of the results obtained by profilometer and AFM.

Figure 3.9 shows the schematic of how the thickness measurement is done in FIB. First a hole is made on the sample by intense Ga^+ ions with the column perpendicular to the sample surface. By checking the signal coming from secondary electrons to the detector; it is possible to distinguish between different layers. After reaching the substrate, the sample is rotated 45° so that the incident beam from the column is almost parallel to the sample surface and then an image is taken at this position which shows the cross section of hole created and hence different layers.

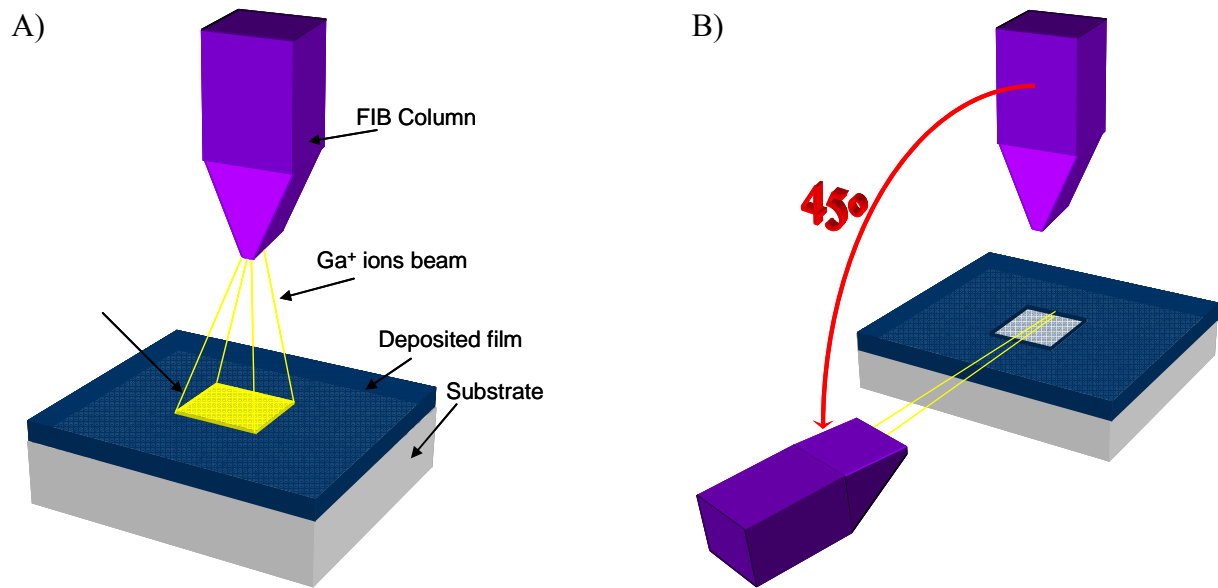


Figure 3.9. Schematic of thickness measurement procedure in FIB. A) Making of a hole in sample assuring that it reaches the substrate B) Tilting the sample 45 degrees and imaging the cross section of the hole.

In figure 3.10 the measured thickness of one of the samples by FIB is shown.

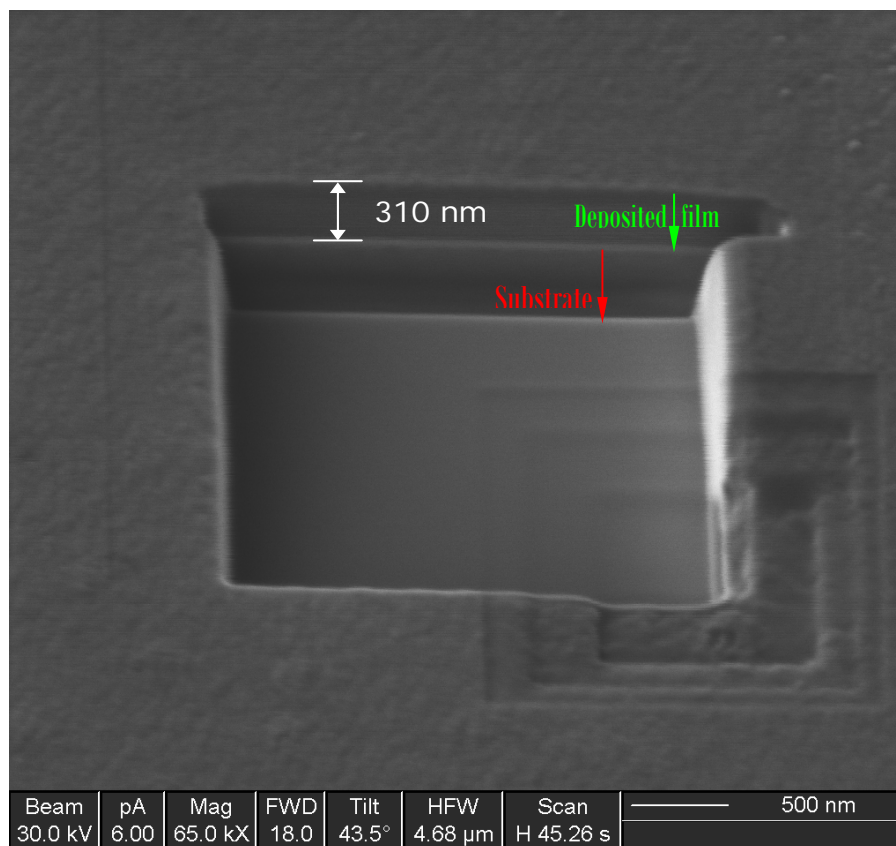


Figure 3.10. FIB image of the calibration sample. The different layers of deposited film and the substrate are clear. The array of squares on the bottom right is the result of focusing.

BIBLIOGRAPHY

- [1] W.R. Grove, Philos. Trans. Faraday Soc. **87** (1852).
- [2] I. Langmuir, General Electric Rev. **26**, 731 (1923).
- [3] M. Ohring, *The Materials Science of Thin Films*, (Academic Press, 1992).
- [4] S.A. Campbell, *The Science and Engineering of Microelectronic Fabrication*, (Oxford University Press, 2001).
- [5] R. E. Somekh and Z. H. Baber, J. Phyc. E:Sci. Instrum. **21**, pp. 1029-1033 (1988).
- [6] *Introduction to surface and thin film processes*, J. A. Venables, (Cambridge University Press, United Kingdom, 2000).
- [7] Z. Barber. *Film Deposition and microfabrication Techniques*, Lecture Notes, Cambridge University, 2005.



CHAPTER 4
CHARACTERIZATION TECHNIQUES

“Measure what is measurable, and make measurable what is not so.”

Galileo Galilei.

Various characteristic techniques used in this project are explained here. First a brief introduction of the instrument is given followed by the experiments done with that instrument. The results and discussions of the experiments are brought in chapter 5.

4.1 ENERGY-DISPERSIVE X-RAY SPECTROSCOPY (EDXS)

4.1.1 INTRODUCTION

Microanalysis is the determination of the composition of the specimen on the microscopic scale. Chemical analysis in the scanning electron microscope is performed by measuring the intensity distribution and the energy of the X-ray signal generated by a focused electron beam as the exciting medium. Physically the generation of the X-ray is a secondary process preceded by the ionization of an atom. In general two main spectroscopic techniques can be distinguished depending on the physical property measured, the wavelength or the energy of the emitted X-ray. The corresponding methods are Wavelength Dispersive X-ray Spectroscopy (WDXS) and Energy Dispersive X-ray Spectroscopy (EDXS) where WDXS is almost exclusively used in conjunction with SEM. In this experiment, however, EDXS was mainly used for determination of the chemical composition. The average energy resolution of EDXS detectors is approximately 130 eV which only allows measurement of the energy of the splitted energy levels in heavier elements whereas WDXS can be usually used to resolve individual sub-lines with resolution of 2eV approximately.

4.1.2 PRINCIPLES

When an atom is being ionized by electron bombardment, by transition of a K-shell electron into vacuum (The result is an ion in an excited state) and after a finite dwell time (typically 10^{-12} s), the generated hole can be filled by an electron coming from upper shells. In this case there is a certain probability that the energy set free by this replacement, leads to excitation of a characteristic X-ray. As an example if the generated hole is occupied by an electron from L shell or M shell, it leads to the excitation of the so-called K_{α} and K_{β} X-rays respectively.

As a matter of fact when an electron beam hits a material, X-rays are formed by two processes giving two types of X-ray, bremsstrahlung and characteristic X-rays. Bremsstrahlung X-rays caused by electrons being decelerated by the nucleus and electrons in the atoms in the material. Energy is lost by the electron on being decelerated and is emitted as X-rays. It contains all energies from 0 eV up to the beam energy. The intensity of the bremsstrahlung is given by *Kramer's law*:

$$I \approx \frac{iZ(E_0 - E)}{E} \quad (4.1)$$

Where,

$$\begin{cases} i = \text{beam current} \\ Z = \text{average atomic number} \\ E_0 = \text{incident electron beam energy} \end{cases}$$

This is shown as the dotted line in the figure 4.1.

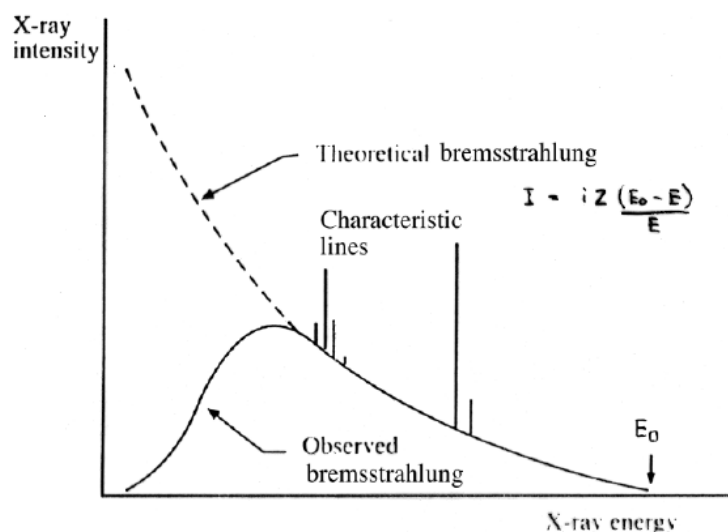


Figure 4.1. The bremsstrahlung and characteristic X-ray intensity as a function of energy. The generated intensity increases rapidly at low energies but low energy X-rays are absorbed by the specimen and the detector. E_0 is the energy of the electron beam causing the X-ray emission. Two families of characteristic lines are shown superimposed on the bremsstrahlung [1].

The maximum energy of the bremsstrahlung is E_0 . In practice the bremsstrahlung is cut off at low energies (solid line) because low energy X-rays are absorbed more in the specimen and thus never escape. The bremsstrahlung X-rays are generally not useful for analysis, they form a background that must be removed.

The process competing with the emission of X-rays is the emission of Auger electrons, where the sum of the fluorescence yield of X-rays and probability of emission of Auger electrons is always equal to 100%. The probability of X-ray emission is called the fluorescent yield, ω . For example, the fluorescence yield for the K shell is defined as:

$$\omega_K = \frac{\text{No. of X-ray photons emitted}}{\text{No. of K shell vacancies}} \quad (4.2)$$

The fluorescent yield has the following relation to the atomic number, Z :

$$\omega \approx \frac{Z^4}{a + Z^4} \quad (4.3)$$

For the K shell $a \approx 10^6$. The fluorescent yield versus the atomic number is plotted in figure 4.2.

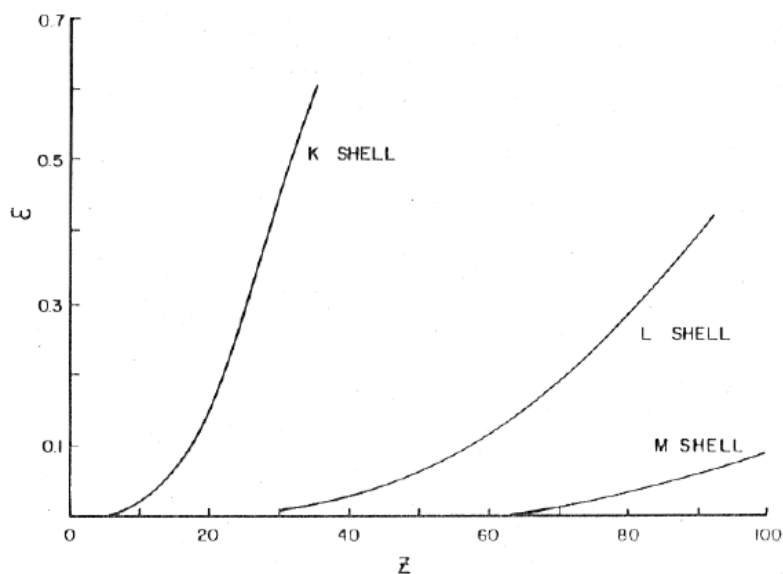


Figure 4.2. Fluorescence yield (ω) as a function of atomic number for the K, L and M shells [2].

For low Z the fluorescent yield becomes very small, e.g. for C ($Z=6$), $\omega_K \approx 0.001$ and for Ge ($Z=32$), $\omega_K \approx 0.5$. Thus X-ray emission is very inefficient for low Z , and Electron Energy Loss Spectroscopy (EELS) is a more efficient technique for analyzing low Z elements. However, in contrast to the fluorescence yield of X-rays which increases with atomic number Z , the portion of emitted Auger electrons is reduced by increasing Z .

One should bear in mind that not all conceivable transitions between the existing electronic energy levels are allowed. The so-called dipole selection rule enable prediction of all possible transitions between electronic energy levels where n is the principal quantum number, l the angular quantum number and $j = l \pm s$ is the total angular momentum i.e. the combination of the orbital and spin angular momentums.

Dipole selection rule:

$$\begin{aligned}
 \Delta n &> 0 \quad (\text{i.e. } L \rightarrow K \text{ and } M \rightarrow K \text{ possible but not e.g. } L_3 \rightarrow L_2) \\
 \Delta l &= \pm 1 \\
 \Delta j &= 0 \text{ or } \pm 1
 \end{aligned}
 \tag{4.4}$$

Transitions to the K shell are called K; transitions to the L shell are called L, etc. Greek letters are used to denote the shell the transition is from, in approximate order of intensity (α is more intense than β etc.). The transitions are very sharp and depend on the element the X-rays are emitted from, and are thus useful for analysis.

The energy (or wavelength) of characteristic X-rays follows Moseley's relation:

$$\begin{cases} X\text{-ray Energy (eV)} \Rightarrow E = \frac{hc(Z-C)^2}{eB} \\ X\text{-ray wavelength} \Rightarrow \lambda = \frac{B}{(Z-C)^2} \end{cases} \quad (4.5)$$

Where,

B, C = constants depending on the X-ray line (K_α, L_α etc.)

Z = atomic number

e = electron charge

c = speed of light

h = Planck's constant

In electron microscopes, only electrons are used to probe the specimen. The diagram 4.3 shows the signals emitted when a specimen is bombarded with electrons and the techniques that use these signals.

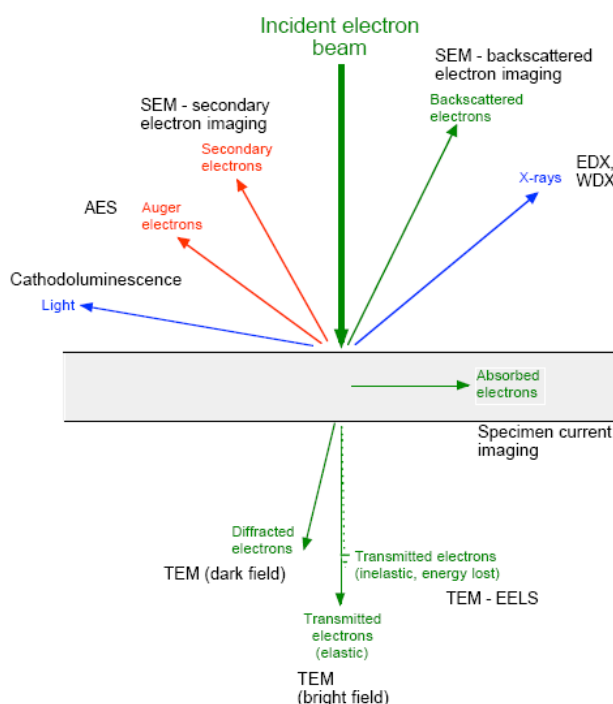


Figure 4.3. Output signals generated by electron bombardment of a thin specimen [4].

For a thick specimen, as in SEM, the transmitted electrons are absorbed in the specimen and give rise to a specimen current.

When an electron beam hits a material a characteristic *Interaction Volume* is generated by the electrons as they penetrate and slow down. The place where the electrons enter the material they have high energy and so suffer little lateral scattering. Thus they form a narrow neck. As the electrons are slowed down, they are scattered sideways more forming the bulb shape.

The general shape of the interaction volume in a bulk sample is shown in figure 4.4. The distances mentioned are for copper sample and a 20 kV electron beam.

X-rays are generated throughout the whole interaction volume and are detected from this volume. Backscattered, secondary and Auger electrons are also generated from all of this volume but due to their lower energies have limited ranges in the sample. Backscattered electrons are emitted from relatively large depths, e.g. 300 nm for Cu, secondaries from the top 5 to 50 nm and Auger electrons from the top 1 nm only. Thus the X-ray and backscattered signals have a much poorer resolution than the secondary or Auger signals.

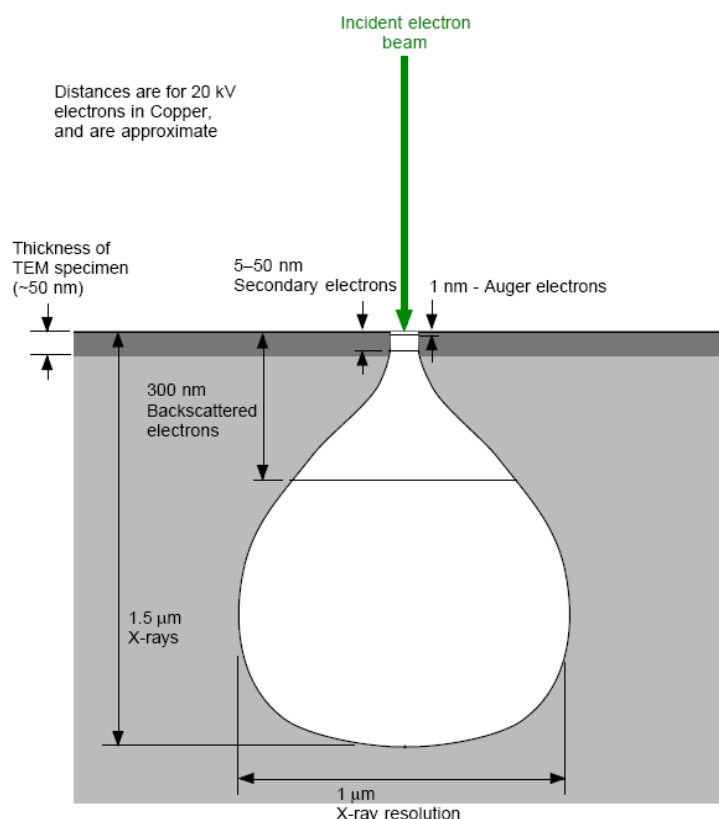


Figure 4.4. The interaction volume for electrons in a bulk sample. Distances are for 20 kV electrons in copper. For aluminum, multiply by 3 [4].

For electron beam illumination of an object the spatial extension of the volume from which a specific interaction signal is gained depends strongly on the material itself, the diameter of the beam, the primary electron energy and the specimen thickness. In bulk materials many more interaction processes occur between the incoming electrons and the target atoms in comparison to thin films. Each of the interactions can change the trajectory of the electron beam and therefore broadening the average diameter of the electron beam. Hence the thicker the specimen, the more extended the interaction volume which essentially limiting the achievable lateral resolution.

In the TEM, the sample thickness is typically around 50 nm, as shown above. Most of the electrons go right through the sample with little interaction. Thus the interaction volume does

not degrade the resolution like it does in SEM. However the much smaller interaction volume in TEM means a much smaller signal. The interaction volume varies with the atomic number (Z) of the target, the energy of the electron beam and the angle between the beam and the specimen surface. There are two ways of measuring the electron range in a material (and hence the size of the interaction volume), the *Bethe* range (average distance traveled by an electron derived from theory) and *Kanaya-Okayama* (K-O) range (more empirical). The *Kanaya-Okayama* range is perhaps the more accurate and more useful:

$$R = \frac{0.0276AE_0^{1.67}}{Z^{0.889}\rho} \quad (4.6)$$

Where,

$$\left\{ \begin{array}{l} A : \text{Atomic mass} \\ E_0 : \text{beam energy in keV} \\ Z : \text{Atomic number} \\ \rho : \text{Density in } \frac{\text{gr}}{\text{cm}^3} \end{array} \right.$$

Below is a table showing the electron ranges calculated using the above formula for three target materials at various electron energies.

Table 4.1. K-O electron ranges (in micrometers) [2]

Target	5 keV	10 keV	15 keV	20 keV
Aluminium	0.41	1.32	4.2	8.3
Copper	0.15	0.46	1.47	2.89
Gold	0.085	0.27	0.86	1.70

The width of the interaction volume, and hence the X-ray resolution, is typically about 2/3 of the electron range shown above. Thus the X-ray resolution is better at lower accelerating voltages, and is much worse for lower atomic number specimens.

The electron range also depends on the angle the electron beam hits the specimen at (measured as the angle between the beam and the specimen normal). This is given approximately by:

$$\text{Electron range at angle } \theta: R(\theta) = R \cdot \cos(\theta) \quad (4.7)$$

For TEM specimen, there is very little broadening of the beam and the X-ray resolution which depends mostly on the width of the electron beam, is much better than for the bulk specimens in SEM.

4.1.3 SAMPLE PREPARATION

Samples were mounted onto Al stubs (12 mm in diameter) using silver paint. Since the substrates were insulating, it was necessary to apply a small amount of silver paint to connect the film, substrate and stub. By placing two samples on each stub it was possible to analyze twelve samples without breaking vacuum. The paint was left to dry for one hour before placing the stubs in the SEM, as outgassing of the solvent would prevent the required high vacuum condition from being attained.

4.2 X-RAY DIFFRACTION

4.2.1 X-RAY GENERATION

X-rays are electromagnetic radiation with typical photon energies in the range of 100 eV - 100 keV. For diffraction applications, only short wavelength X-rays (hard X-rays) in the range of a few angstroms to 0.1 angstrom (1 keV - 120 keV) are used. Because the wavelength of X-rays is comparable to the size of atoms, they are ideally suited for probing the structural arrangement of atoms and molecules in a wide range of materials. The energetic X-rays can penetrate deep into the materials and provide information about the bulk structure. X-rays are produced generally by either X-ray tubes or synchrotron radiation. In an X-ray tube, X-rays are generated when a focused electron beam accelerated across a high voltage field bombards a stationary or rotating solid target. As electrons collide with atoms in the target and slow down, a continuous spectrum of X-rays are emitted, which are termed Bremsstrahlung radiation. The high energy electrons also eject inner shell electrons in atoms through the ionization process. When a free electron fills the shell, an X-ray photon with energy characteristic of the target material is emitted. Common targets used in X-ray tubes include *Cu* and *Mo* which emit 8 keV and 14 keV X-rays with corresponding wavelengths of 1.54 Å and 0.8 Å, respectively. (The energy E of a X-ray photon and its wavelength is related by the equation $E = h c / \lambda$, where h is Planck's constant and c the speed of light).

4.2.2 X-RAY ANALYSIS OF THIN FILMS

This is a very widely used characterization technique as it provides a lot of information about the structure of the film. One can determine if there is any texturing, the degree of crystallinity, lattice parameters, and the size of crystallites, if the expected phases are present etc. It is a non-destructive technique and the sample preparation is minimal. However, the large penetration depth of X-rays means that their path length through the film is too short to produce diffracted beams of sufficient intensity and the substrate tends to dominate the signal. Therefore, long counting times are required and the sample should be as large as possible. For

XRD work a thick film would be grown on 10×5 mm substrates where possible. The details of XRD are discussed below.

Figure 4.5 shows the geometry of diffraction from a series of (001) lattice planes. The incident beam penetrates the lattice and scatters from each of the atoms in the 3D lattice. When the angles of the incident and diffracted beams are equal, (as measured from atoms in the (001) planes in this case), the path lengths of rays scattered off any of the atoms in that plane will be the same. These rays constructively interfere resulting in a plane wavefront, which can be considered as having been specularly reflected from the (001) planes. The wave vectors of the incident and ‘reflected’ beams are denoted by k_0 and k_1 respectively. The distance between successive (001) planes is known as the d-spacing, d . Therefore, by simple trigonometry the path difference between beams ‘reflected’ from successive planes in the z direction is simply given by $2d\sin\theta$. For constructive interference, the path difference must be an integral multiple of wavelengths, and so we find that,

$$n\lambda = 2d \sin \theta \quad (4.8)$$

This is known as the *Bragg* equation and when this condition is satisfied a diffraction maximum will be observed.

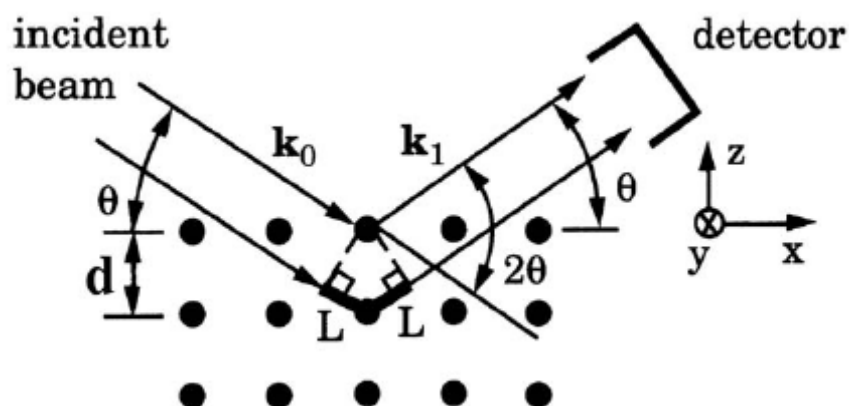


Figure 4.5. Geometry of X-ray diffraction from a series of (001) planes [8].

For XRD characterization of polycrystalline thin films, monochromatic X-rays and *Bragg-Brentano* geometry are normally employed. The thin film surface is oriented as shown in Figure. 4.6, so that the film normal bisects the angle made between the source, the centre of the film and the detector. θ is scanned by rotating the sample about the y -axis, while the detector is moved through 2θ to keep it at the specular angle with respect to the film surface. At values of 2θ for which the atomic periodicity, d perpendicular to the film surface satisfies the Bragg condition for the λ being used, a peak appears. This is how the diffraction pattern is built up and from the relative intensity of the peaks, the degree of texturing can be determined.

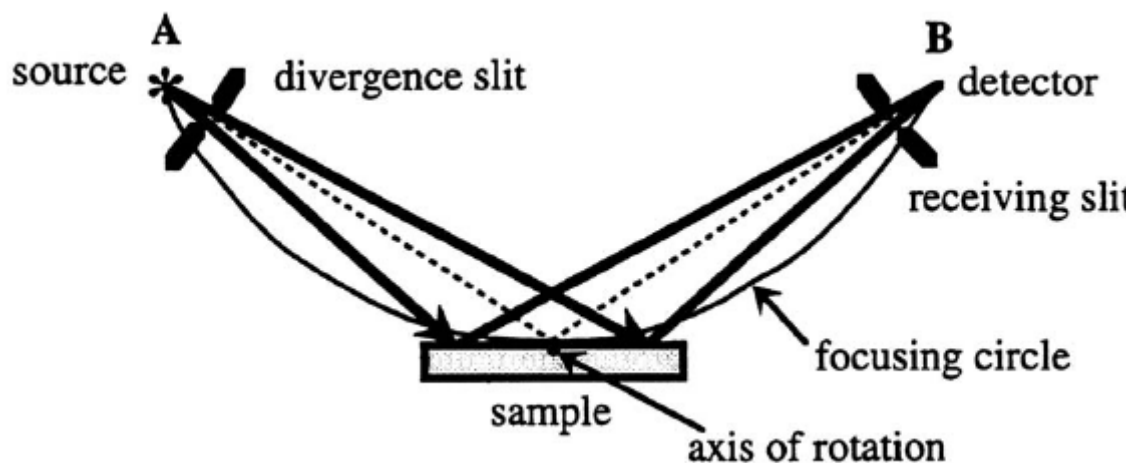


Figure 4.6. The schematic of Bragg-Brentano geometry [8].

The shape of an X-ray diffraction line can contain information about particle size (strictly the size of the coherently diffracting regions in the direction perpendicular to the reflecting planes) and about inhomogeneous variations in interplanar spacing arising from either residual stresses in the material or variations in composition from point to point in the material.

In this work, All X-ray scans carried out in this work were done using a Philips X'pert PW3020 diffractometer in Bragg-Brentano geometry. CuK_{α} radiation ($\lambda = 1.54056 \text{ \AA}$) was generated using a sealed copper tube (PW 1730 X-ray generator) with a tube current of 40 mA and a tube voltage of 40 kV. The divergence, receiving and anti-scatter slits were 1° , 0.2 mm and 1° respectively and a 10 mm mask was used. The large slits ensure high intensity of the incident beam which is necessary for phase identification. A nickel filter was employed whenever a substrate with an intense substrate peak was used, since a large number of counts can damage the X-ray detector. However, even Ni filter could not guarantee safety of the detector due to large slits used; therefore a deliberate offset in ω -scan was employed to reduce the number of substrate peak counts substantially. This approach found to be much effective than cutting out the strong substrate peaks from diffraction pattern as this lead to difficulties in background determination and profile fitting for the peaks neat the removed substrate peaks. For Rocking Curve scans, it was necessary to have good resolution; therefore smaller slits were used ($1/12^{\circ}$, 0.1 mm and $1/12^{\circ}$).

A 12×12 mm piece of silicon single crystal was mounted on an aluminium sample holder using a small amount of plasticene. The sample was then mounted onto the silicon single crystal. The Si single crystal does not produce any peaks in the range that is scanned, so all peaks must come from the film or the substrate. It was ensured that there was no plasticene visible to the X-rays because it does produce a diffraction peak. It was important that the sample was level with the sample holder so that the film surface is coincident with the axis of rotation of the goniometer. Any displacement by distance, D of the sample surface from the

center of the diffractometer (radius R) will cause an error in the measurement of 2θ . This error can be expressed as,

$$\partial(2\theta) = 2D (\cos\theta) / R \quad (4.9)$$

In order to compensate for this sample displacement error, first a ω -scan was done at the suspicious substrate peaks. After adjusting the offset, a 2θ -scan was done followed by changing the peak position to the maximum intensity or in other words, setting the offset between θ and ω . The offset adjustment between θ and ω was carried out until the ω -offset becomes constant.

All data was collected using Philips X'Pert software and phase analysis along with profile fitting were carried out using Philips HighScore Plus 2.0a software.

4.2.3 WARD-WALLACE TEXTURE CAMERA

4.2.3.1 INTRODUCTION

X-ray diffraction cameras in which the diffraction pattern is recorded on a cylindrical photographic film coaxial with the incident beam have previously been used to make measurements of preferred orientations in polycrystalline materials by Kratky (1930), Wooster (1948), Mackay (1953) and Richards (1964). The diffraction cones of constant 2θ intersect the recording film in straight lines. These may then be scanned with a linear densitometer to yield intensity distributions characteristic of the preferred orientation, allowing for the effects of X-ray absorption in the specimen.

The Ward-Wallace cylindrical texture camera [5, 6] employs a flat specimen inclined to the incident X-ray beam, which lies along the cylinder axis. The camera is particularly applicable to the crystallographic examination of thin crystalline films deposited on flat substrates. It is capable of detecting and identifying very thin deposits and of characterizing the type of preferred orientation that may have occurred. For cases where orientation effects are not pronounced, consideration of the specimen absorption factors provides information about layer thickness and order of deposition when more than one layer is present.

4.2.3.2 DESCRIPTION OF CAMERA

The camera uses a cylindrical cassette of 5-73 cm diameter (allowing for the thickness of the photographic film) and 12.5 cm long. Collimator and beamstop tubes, concentric with the camera axis, are mounted at each end of the cassette on discs which act as radiation shields. The flat specimen is mounted on a disc perpendicular to a motor shaft, which can if required rotate the specimen continuously in its own plane. (The experimental arrangement is shown in Figure 4.7) The angle between the motor shaft and the camera axis is continuously variable to

give the specimen plane any desired angle of inclination, i , up to 45° , to the incident beam. The position of the specimen along the camera axis is also variable, and since the finite length of the cassette cuts off the diffraction pattern at both ends of the 2θ scale, by altering the position of the specimen the whole diffraction pattern may be shifted along the axis so that either the low- 2θ or high- 2θ regions may be recorded on the film. Since the relative positions of the powder diffraction lines are unaffected by movement of the specimen along the camera axis or motor shaft or variation in i , the only essential alignment is that of the incident beam accurately coincident with the cylindrical axis.

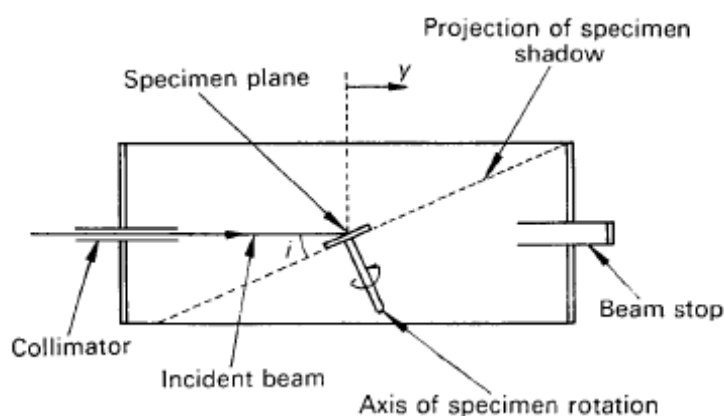


Figure 4.7. Diagram of cylindrical texture camera. i is the angle of incidence [5].

4.2.3.3 APPLICATION OF THE CAMERA TO THIN FILMS

The powder diffraction patterns of both thin films and substrates in the cylindrical camera (radius R) may be interpreted by measuring the positions of the lines, y , along the camera axis and deriving the corresponding values of 2θ , given by the relation $y = R \cot 2\theta$, and interplanar spacing, d , from Bragg's law. If ϕ is the angle between the planes, parallel to the camera axis, containing the diffracted beam and the specimen surface normal, then the x coordinate is equal to $R\phi$. Part of the diffraction pattern is excluded from the photograph by absorption of the diffracted radiation in the substrate.

Preferred-orientation effects are commonly exhibited by thin films and are revealed by arcing or intensity modulations of the powder diffraction lines along the x axis. Uniaxial or fiber textures, having cylindrical symmetry about the surface normal, may be developed during the growth or deposition of the films as there is a tendency for crystallites having certain lattice planes aligned with the surface to grow preferentially. Most thin films are characterized by one or more planes that are preferentially aligned parallel to the surface.

Therefore conventional methods give a very poor signal to noise ratio due to stress and preferred orientation effects present in most thin films. The effect of preferred orientation is to take the spherically symmetric reciprocal powder sphere and to impose a non-even

distribution. The simplest form of orientation is the Uniaxial or fiber orientation and the reciprocal powder sphere takes the form of bands with a common axis. The unique axis is usually termed the fiber axis. In order to better visualize the effect of fiber axis on formation of arcs (bands) rather than circles, we consider a reciprocal lattice of the compound of interest and decide one direction as the fiber axis. Now we consider a significant mosaicity and small crystallite sizes which will broaden each reciprocal lattice point. If we rotate the broadened reciprocal lattice around the fiber axis by 360° and keep the locus of the reciprocal lattice points as the reciprocal powder sphere, the intersection of this new reciprocal powder sphere with the Ewald sphere is now a series of arcs rather than circles as for a random powder. Therefore conventional diffractometers and powder cameras fail to show all the reflections when recording the diffraction pattern from a fiber oriented compound. Ward-Wallace camera is for overcoming this problem. The incident beam is coaxial with the film cassette with the result that Bragg cones record as straight lines allowing easy assessment of any fiber oriented arcing.

4.3 TRANSMISSION ELECTRON MICROSCOPY

Transmission Electron Microscope is used to obtain structural information from the thin enough samples that allow the electrons pass through. Therefore, the nature of the thin films makes them ideal for study with TEM; however, one should not forget that thin films usually are grown on thick and impenetrable substrates that shall be removed prior to insertion in the TEM.

The thermoionically generated electrons with accelerating voltages such as 100 kV and more, are focused on the specimen through condenser lenses. In this stage depending on what kind of scattering processes are experienced by electrons through their passage from sample, two modes and the kind of information obtained, are differentiated. Elastic scattering involves no energy loss and happens when electrons interact with potential ion core of sample atoms and give rise to diffraction image. Inelastic scattering, on the other hand, involves an energy loss in the interaction of the incident electron beam and the matrix electrons (electron clouds) at inhomogeneities such as grain boundary, dislocations, second phase precipitates, defects, density variations etc. This cause complex absorption and energy loss therefore scattering of the incident electrons leading to spatial variation in the intensity of the transmitted electrons. Of course generation of by-products such as X-rays and Auger electrons also happens which usually are not collected.

The primary and diffracted electrons are then forced to pass through a series of lenses starting from the Objective lens. As the objective lens produces the first image of the object, requires being the perfect lens. Depending on how the beams reaching the back focal plane of the

objective lens, distinguishes the operation mode. Anyhow, either a magnified image or a diffraction pattern is obtained.

Images can be formed in number of ways. The bright field image is obtained by intentionally excluding all the diffracted beams and allowing only the central beam to go through by placing a suitably sized aperture in the back focal plane of the objective lens. Intermediate and projection lenses then magnify this central beam. If instead of the central beam, one of the diffracted beams is selected (and all the others blocked) and magnified, a Dark field image is formed this time. In both Bright field and Dark field images, we are talking of amplitude contrast because almost all the diffracted beams with their phase relationships are excluded from the imaging sequence.

In the third method, the primary transmitted beam and one or more of the diffracted beams are made to recombine, thus preserving both their amplitudes and phases. This technique is used in High Resolution imaging which enables diffracting planes and arrays of atoms to be distinguished.

The high magnification of all the TEM methods is a result of the small effective wavelengths employed. According to the *De-Broglie* relationship [10],

$$\lambda = \frac{h}{\sqrt{2mqV}} \quad (4.10)$$

Where h is the Planck constant, m and q are electrons mass and charge. V is the potential difference through which electrons are accelerated.

4.4 ATOMIC FORCE MICROSCOPY (AFM)

Scanning probe microscopy (SPMs) consists of microscopy forms that are used to measure the properties of surfaces. There are many different types of SPMs including atomic force microscopes (AFM), scanning tunneling microscopes (STMs), and magnetic force microscopes (MFMs). A review of SPMs can be found in [11].

Atomic Force Microscopy is a powerful tool for assessing the morphological quality of films. The first AFM was made by gluing a tiny shard of diamond onto one end of a tiny strip of gold foil. In the fall of 1985 Gerd Binnig and Christopher Gerber used the cantilever to examine insulating surfaces. A small hook at the end of the cantilever was pressed against the surface while the sample was scanned beneath the tip. The force between tip and sample was measured by tracking the deflection of the cantilever. This was done by monitoring the tunneling current through a second tip positioned above the cantilever. They could delineate lateral features as small as 300Å. The force microscope emerged in this way. In fact, without the breakthrough in tip manufacture, the AFM probably would have remained a curiosity in

many research groups. It was Albrecht, a fresh graduate student, who fabricated the first silicon micro cantilever and measured the atomic structure of boron nitride. Today the tip-cantilever assembly typically is micro fabricated from Si or Si_3N_4 . The era of AFM came finally when the Zurich group released the image of a silicon (111) 7×7 pattern. The world of surface science knew that a new tool for surface microscope was at hand. After several years the micro cantilevers have been perfected, and the instrument has been embraced by scientists and technologists.

The AFM was operated in ‘Tapping Mode’. In this technique the probe is oscillated at a constant frequency as the AFM head scans across the surface. The cantilever is oscillated at or near its resonant frequency with amplitude ranging typically from 20nm to 100nm. The tip lightly “taps” on the sample surface during scanning, contacting the surface at the bottom of its swing. The amplitude of oscillation of the tip varies as it moves nearer to the surface of the film, this change is used as feedback to control the sample-tip distance and deduce the surface height of the film. The tapping mode of AFM is shown schematically in figure 4.8.

The feedback loop maintains constant oscillation amplitude by maintaining a constant RMS of the oscillation signal acquired by the split photodiode detector. The vertical position of the scanner at each (x, y) data point in order to maintain a constant “setpoint” amplitude is stored by the computer to form the topographic image of the sample surface. By maintaining constant oscillation amplitude, a constant tip-sample interaction is maintained during imaging. The x - and y -axis topographic resolution for most SPM scanning techniques, including AFM, is typically 2 to 10nm. The z -axis resolution is better than 0.1nm.

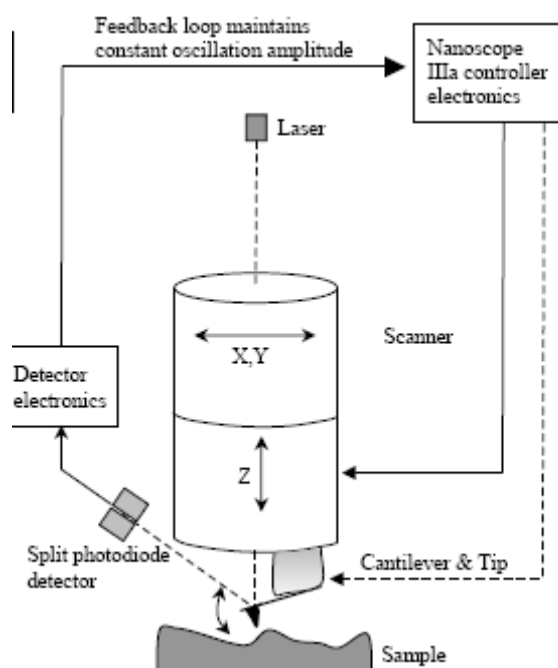


Figure 4.8. Schematic diagram showing the AFM tapping mode [11].

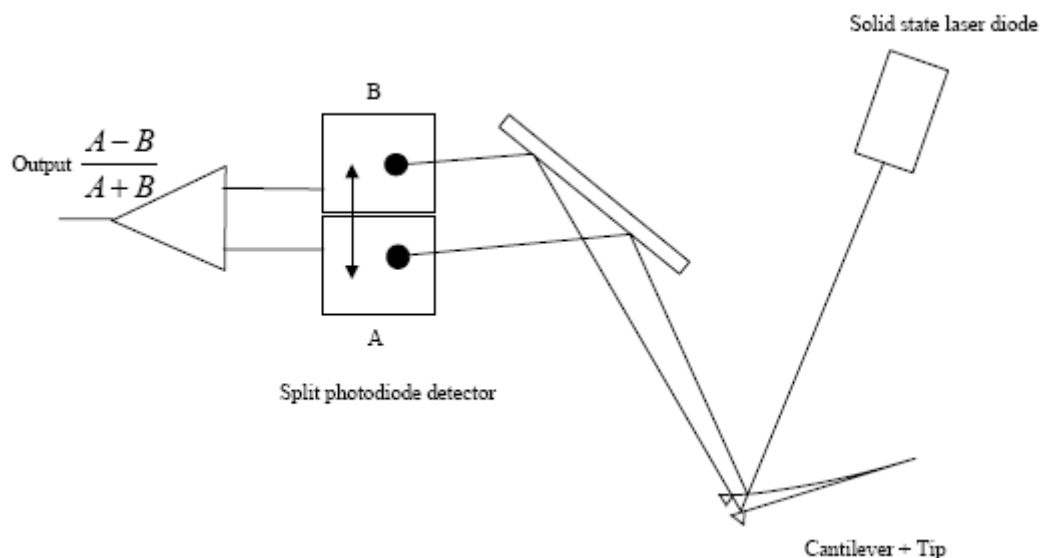


Figure 4.9. The mechanism of “beam deflection” detection for both contact and tapping mode [11].

Figure 4.9 shows the mechanism of “beam deflection” detection for both contact and tapping mode. Laser light from a solid state diode is reflected off the back of the cantilever and collected by a position sensitive detector (PSD) consisting of two closely spaced photodiodes whose output signal is collected by a differential amplifier. The angular displacement of the cantilever results in one photodiode collecting more light than the other photodiode, producing an output signal (the difference between the photodiode signals normalized by their sum), which is proportional to the deflection of the cantilever. This system can detect cantilever deflection $< 1\text{Å}$ and the long beam path (several cm) amplifies changes in the beam angle.

4.5 T_c MEASUREMENTS

In order to measure the critical transition temperature of the thin films, T_c , a four point resistance technique was used employing a probe dipped into a *He* storage dewar (Figure 4.11). The probe consists of a copper block with a platinum resistance temperature sensor (Cernox thermometer) embedded within. The film is contacted by an array of spring loaded Pogo® contacts set in a tufnol block (Figure 4.10). The contact block clamps the sample to the copper block ensuring good thermal contact between the temperature sensor and the sample. The probe is cooled by lowering it slowly into the cold helium vapor in the neck of a standard helium transport dewar. Data acquisition is automatically performed by a program written in the graphical programming language LabVIEW¹. As the probe is cooled, the measurement system continually measures the resistance of the film and the temperature sensing element

¹ Program was written by Gavin Burnell

using a standard four wire technique. The resistance of the platinum sensor is converted to a temperature using the calibration supplied by the manufacturer. To limit the amount of data recorded to manageable proportions a new point is only recorded when it is outside a user defined ellipse around the previous point.

In order to avoid the effect of Joule heating, a communicating mode was used so that the direction of current was reversed with the help of a diode.

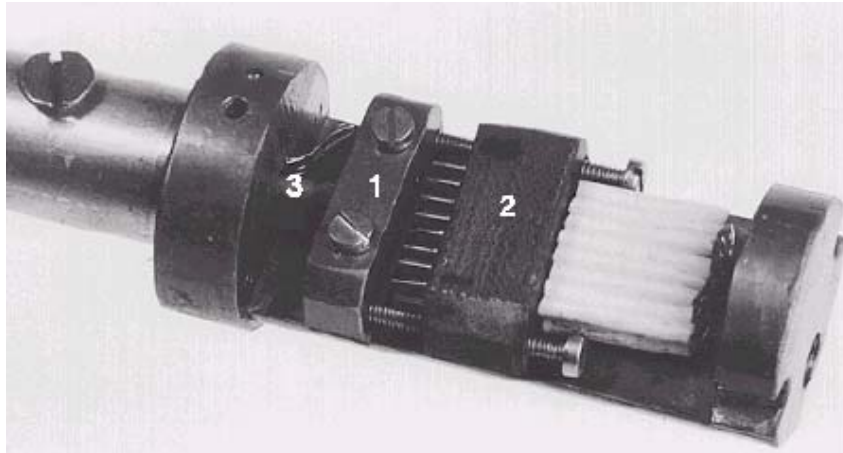


Figure 4.10. Tc probe sample holder showing copper block containing temperature sensor (1), pogo pin holder (2), and wiring (3). (Image courtesy of J. H. Durrell)

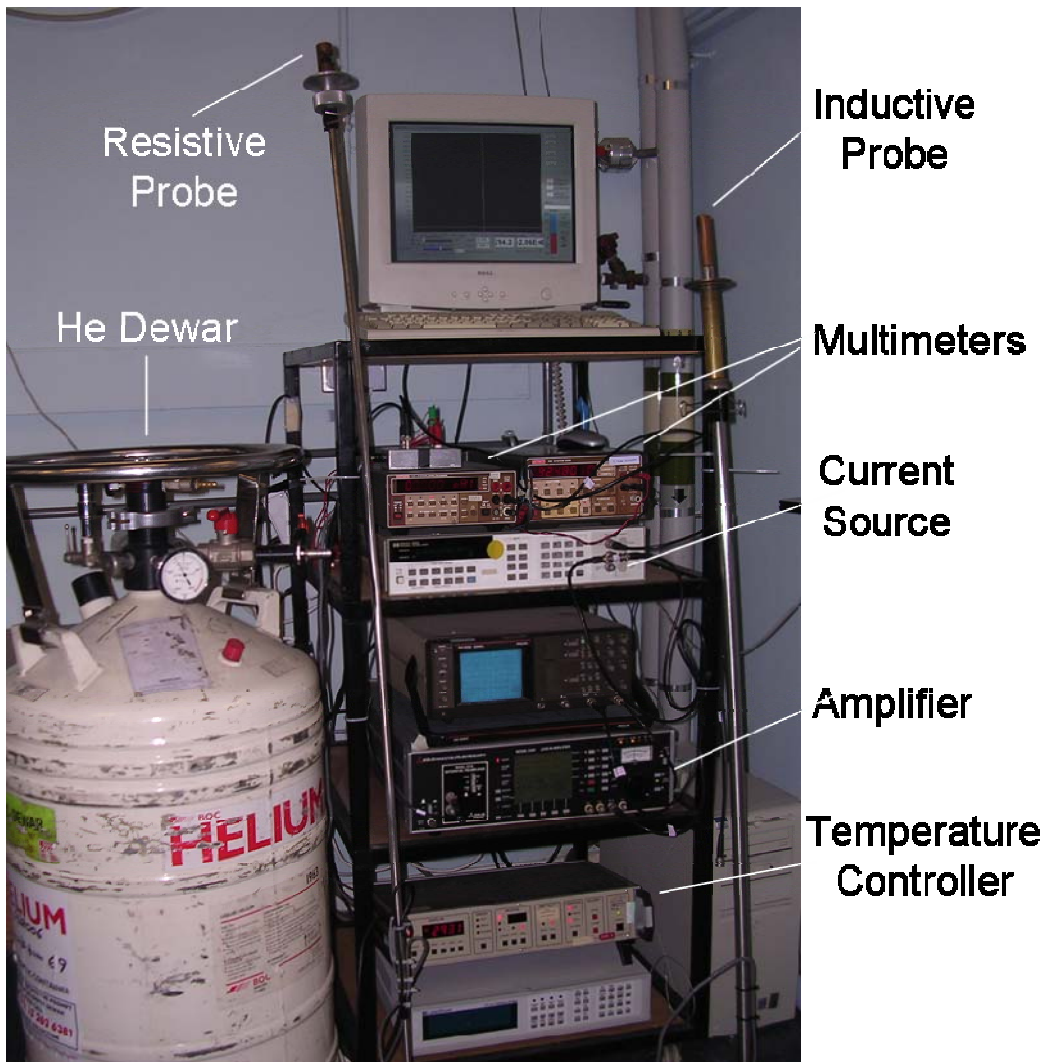


Figure 4.11. The T_c measurement setup, showing both inductive and resistive probes along with current (voltage) source and meters.

4.6 MEASUREMENT RIG

Measurement of the critical current and field of the specimen were done in an 8T superconductor magnet equipped with a high resolution two-axis goniometer.

4.6.1 SAMPLE MOUNTING

Contact to the sample was affected using Pogo® pins. To ensure that differential contraction at cryogenic temperatures does not cause loss of contact, indium pads were used between the pogo pins and the film (figure 4.12).

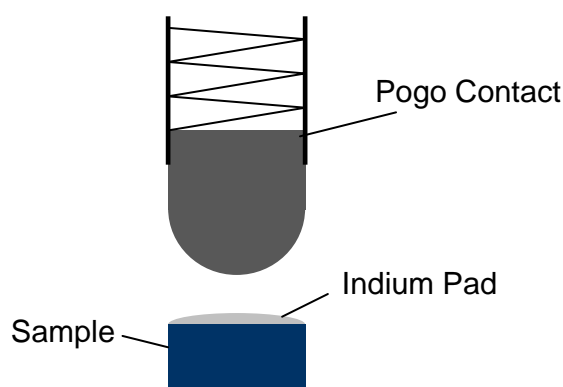


Figure 4.12. Contact between a pogo pin and a superconducting sample.

4.6.2 CRYOSTAT

After mounting the sample on the goniometer, the sample is placed in the bore of a temperature varying 8T superconductor magnet. Figure 4.13 shows the basic layout of the cryostat. By making vacuum using a diaphragm pump, vacuum can be created in the sample space which draws in cold helium liquid through a needle valve. The helium boils and a stream of cold gas flows over the goniometer. The heating element in the copper block allows a temperature controller (Oxford Instruments ITC 4) to maintain the sample at a constant temperature.

The temperature of the copper block is measured using a Lakeshore Cryotronics Cernox™ resistance sensor. The sensor is fitted into a flush fitting aperture in the copper block, as recommended by the manufacturer silicon grease was used to ensure good thermal contact. The magnet system is economical in operation, 30 l of liquid helium often being sufficient for a week of measurements [13].

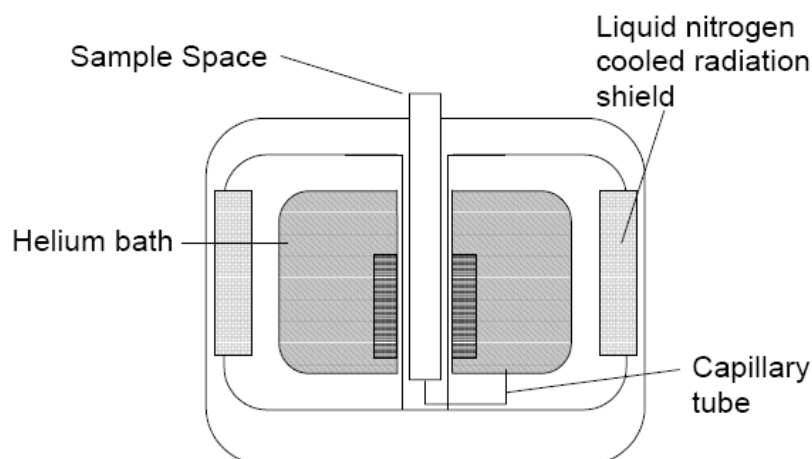


Figure 4.13. Schematic diagram of cryostat. For clarity the needle valve, magnet wiring and supports are omitted. (Image courtesy of J. H. Durrell)

4.6.3 MEASUREMENT APPARATUS

Four terminal resistance measurements on the sample were made using a HP 8250A universal source to drive a current through the sample. The current flowing through the sample was independently measured using a Keithley model 199 DMM. A Keithley model 182 nanovoltmeter was used to measure the voltage developed in the sample. The built in digitally synthesized filter of the nanovoltmeter was used to obtain the lowest noise readings. When in use this requires at least 8 seconds to be allowed between readings, to allow the voltage value to settle. The average noise levels of less than 1×10^{-8} V were measured, with this in mind a voltage criterion of 5×10^{-8} V was chosen to determine critical current. The same configuration also allowed both resistance/temperature and resistance/field measurements to be made. A matrix board allowed the current and voltage pairs to be connected to any combination of the 12 pogo pins in the tufnol block. Figures 4.14 and 4.15 show the physical setup and the block diagram of the measurement system, respectively.

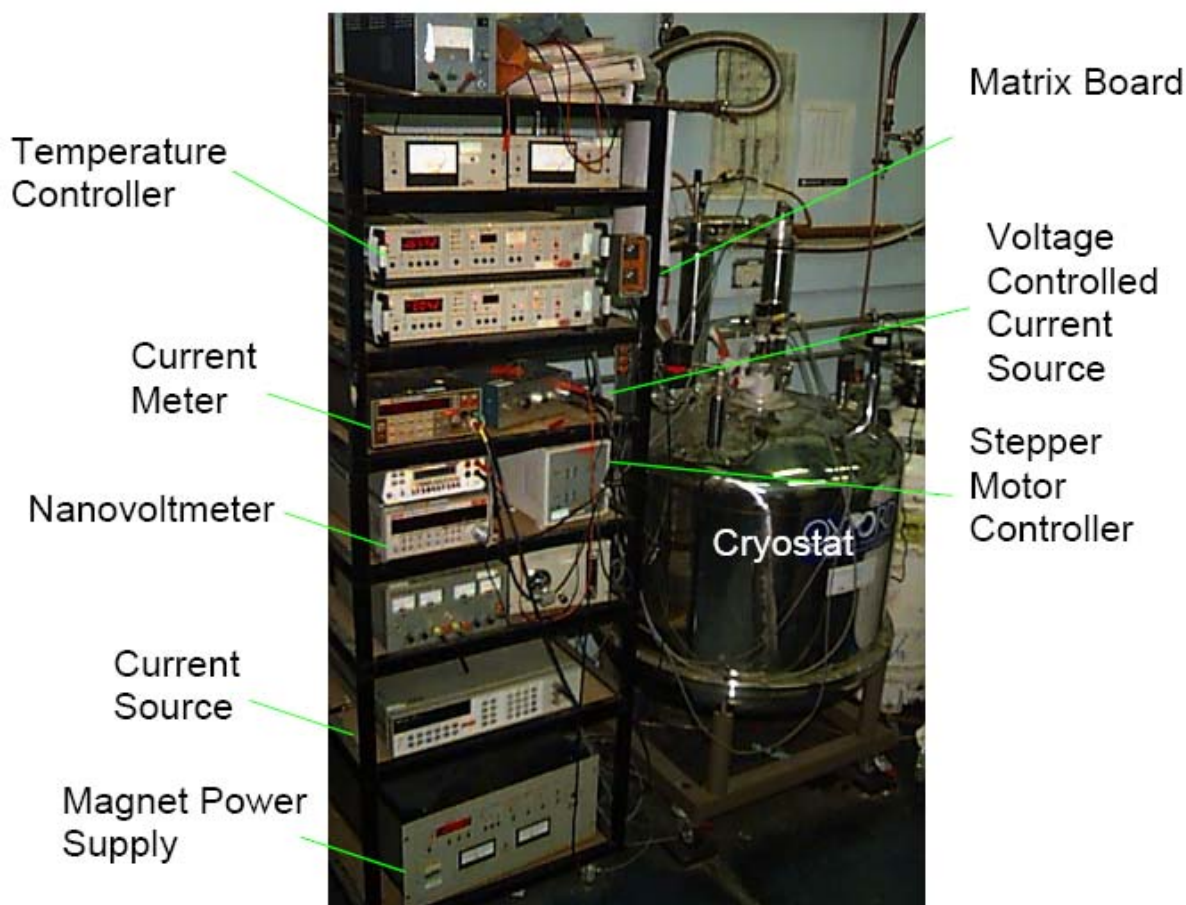


Figure 4.14. Physical layout of the experimental apparatus. (Image courtesy of J. H. Durrell)

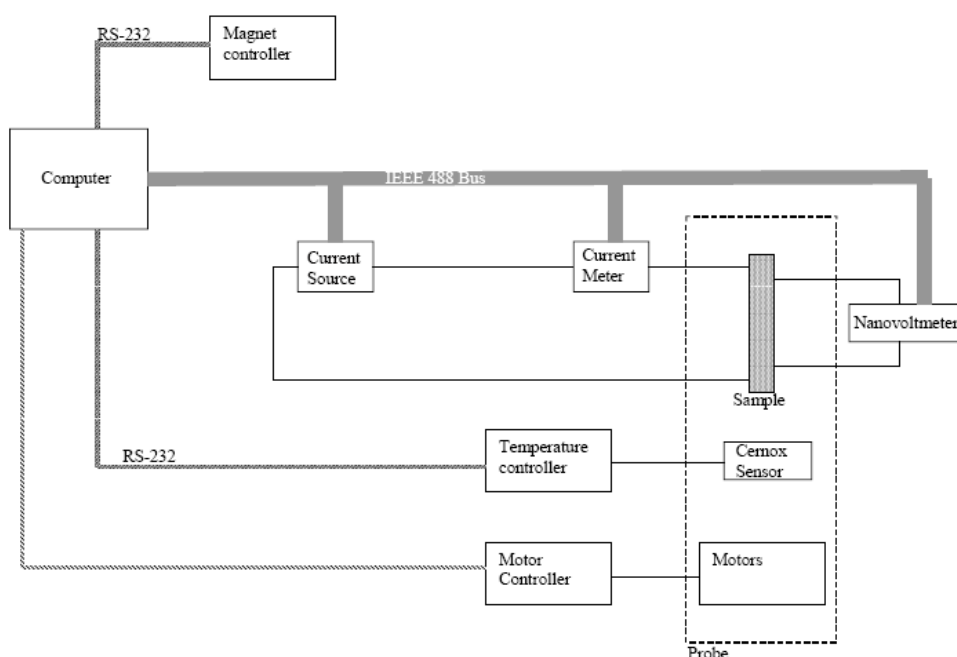


Figure 4.15. Block diagram of the measurement system. (Image Courtesy of J. H. Durrell)

The measurement rig is capable of making a resistance or V/I measurement at any point in the experimental parameter space: $(-8T < B < 8T)$, $(4.2K < T < 300K)$, $(-120^\circ < \theta < 120^\circ)$ and $(0^\circ < \phi < 90^\circ)$. This allows $R(T)$, $R(B)$, $J_c(B)$, $J_c(T)$, $J_c(\theta)$ and $J_c(\phi)$ measurements to be made. For each datum point required the computer sets the required environmental parameters in accordance with scan settings requested by the user².

Resistance values are measured by a commutating technique. A user specified current is applied in the forward and reverse directions to avoid any thermal effect (caused by DC current) and the voltage recorded. In this way any zero offset may be eliminated.

If an IV curve is required the current is then stepped either in predefined increments or in increments determined from the last measured IV curve and the number of data points per curve desired by the user. During the measurement, the current is increased by predetermined steps; at each step the voltage is recorded. When the recorded voltage exceeds a user-defined value, usually two or three times the selected voltage criterion, the measurement is terminated and the computer continues to the next set of experimental parameters. From the curve the critical current is determined by fitting a smoothed polynomial function to the measured data points. The value of the current at the voltage criterion may then be easily deduced.

4.6.4 SAMPLE PREPARATION

In order to pattern the films, they were first cleaned using acetone both in an ultrasound bath and using an airjet. A 2 μ m layer of Hoechst AZ1529 photosensitive polymer resist (positive) was applied and spun onto the sample for 40 seconds and then baked for 1 minute at 120°C to evaporate residue solvents and also promote the chemical cross-linking. The spin parameter (revolution per meter) of the spinner defines the final thickness of the photoresist layer. The photolithography process details like spin speed, baking time and developing/exposure time are found through a set of calibrations until the optimum parameters are found resulting in a good track pattern that is both thick enough and is within the resolution required. The samples were then exposed to UV light through a mask containing the critical current measurement pattern, using a projection lithography system (Canon mask aligner) and the mask pattern was transferred to the photoresist. When using the positive resist, the resist which is exposed to UV light which exactly corresponds to the underlying material which is to be removed. In other words, the polymer resist exposed to the UV light, undergoes a chemical change such that it becomes more soluble in the alkali developer. Therefore the

² Program developed in LabView software by J. H. Durrell.

mask contains exactly the copy of the shape to be patterned on the film³, resulting in remaining of the exact same shape in the underlying film after the lift-off process. The details of the photolithography process, is shown in figure 4.17.

Two different mask aligner machines were utilized in this experiment. Canon contact mask aligner with the resolution of approximately 6 μ m was used for the patterning the samples using the mask with 20 μ m feature sizes and Karl Suss (Karl Suss MJB3 UV300) mask aligner with 2 μ m resolution was used for masks with 5 μ m feature size. Although the UV light produces a wavelength of \approx 400nm, the resolution is limited by the minimum mask feature size, the contact between the mask and the sample and the thickness of the photoresist. Because of the inhomogeneity of the film surface, it was found that the samples patterned with 5 μ m track size, show no superconductivity. This probably is because of the suppression of the order parameter due to the proximity effect at a specific location in the track where there is a agglomeration of Gd island (because of inhomogeneity). Therefore, the mask with 20 μ m track size was preferred. Thirty seconds was found to be satisfactory for projection time to the UV light. The exposed pattern was then developed and removed in a 4:1 concentration of the resist manufacturer's proprietary developer for about 20 seconds. Visual examination under light microscope was performed after drying with nitrogen airgun to ensure that all the resist has been washed away especially at the edges where usually the resist is thicker. If required, any residue could be removed by a cotton bud dipped in acetone. At the end the sample was soaked in water to ensure that all the residues are removed and the surface is clean.

As the sample itself was conductive, there was no need to deposit a conductive layer on the sample; therefore the last step of the patterning was transferring the desired pattern from the patterned photoresist to the film or in other words, to physically etch away the unwanted areas of the film using an Argon ion miller. In an ion-milling system an ion gun directs ionized Argon towards the sample. The incident argon ions ablate both photoresist and the exposed film; however, the layer of the photoresist is much thicker than the film and also is milled much slowly (because the photoresist is not conductive so the ionized Argons are directed mainly towards the conductive film). Ion milling is strictly a mechanical process; it involves no chemical reactions with the sample because it uses a noble gas. It relies on striking a plasma to produce the etch species, and the plasma is initiated by applying a voltage across a gap containing the low-pressure argon gas. The Kaufman ion gun was powered with a Princeton Applied Research power supply, and the chamber was pumped down to less than 4×10^{-6} mbar using a turbo pump prior to milling. Argon gas with a 2% oxygen mixture in an

³ A negative mask, on the other hand, contains the complement of the shape to be patterned on the film. In negative resist, the exposed polymer undergoes chemical changes, resulting it to become more stable.

accelerating voltage of 500V was used to mill the samples at a pressure of 2×10^{-4} mbar. The oxygen enhances the etch rate by oxidizing the debris from the areas of film being removed. Usually a calibration run is performed in order to find the milling rate of the sample and therefore assess the time needed to mill the film. But as the substrate used in this experiment (sapphire) is transparent therefore it is possible to visually verify that the film has milled away. Therefore a milling time of 15 minutes with a 0° beam incidence angle was found to be sufficient for milling of an average 200 nm layer from the film. Ion-milling was found to give very satisfactory clean tracks once the remaining resist is dissolved in acetone, which outweighed the slightly increased complexity of the process. The alternative possible approach to Ar ion milling, is performing wet chemical etching using mixture of ($4\text{HNO}_3 : 1\text{HF} : 4\text{H}_2\text{O}$) acids, which was not practiced in this project.

Figure 4.16 shows an enlarged section of the $29\mu\text{m}$ patterned track after Ar-ion milling.

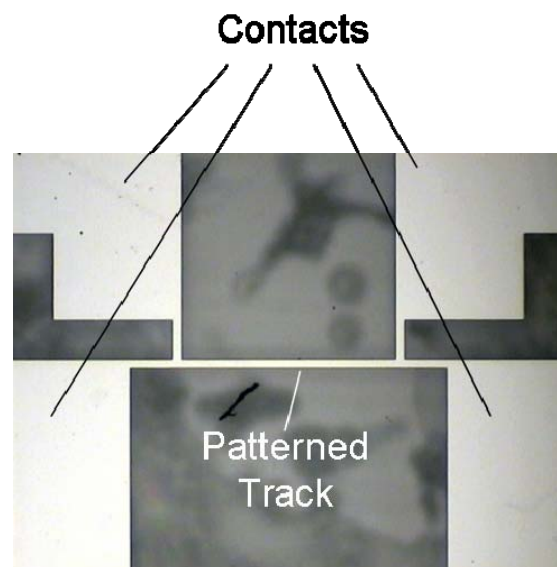


Figure 4.16. Section of Ar ion milled sample. The dark spots are the remained photoresist.

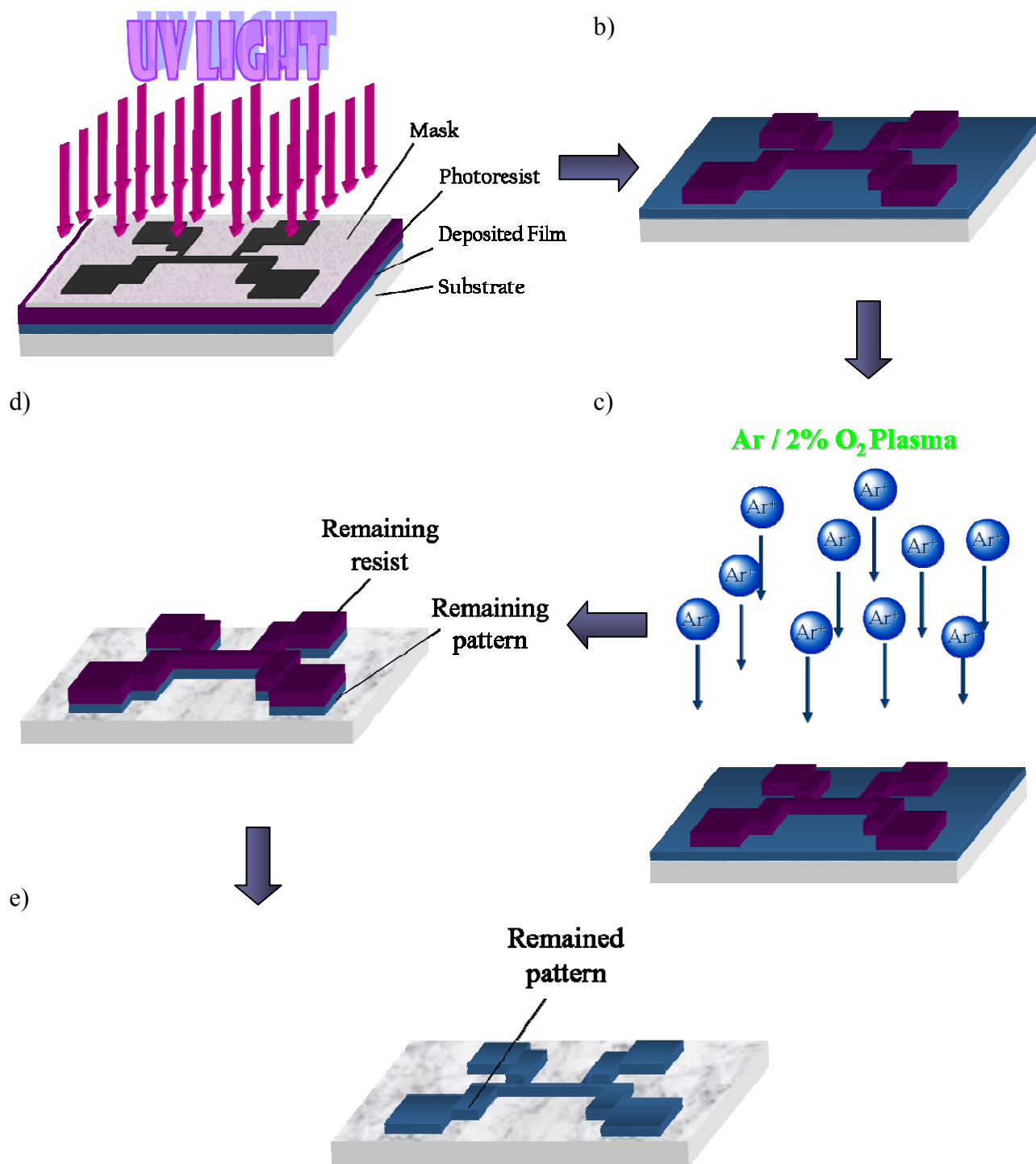


Figure 4.17. An illustration of the photolithography procedure followed by ion milling process. a) Exposure of the film bearing a photoresist layer. b) Developing the exposed film, causing to wash away the exposed resist., c) The ion-milling process, d) soaking in acetone causing to dissolve the remaining photoresist, e) the patterned film with remaining pattern.

4.7 VIBRATING SAMPLE MAGNETOMETER (VSM)

Magnetic characterization was carried out using a Vibrating Sample Magnetometer (VSM), which was first described by Foner [14], is essentially a gradiometer, measuring the difference in magnetic induction between a region of space with and without the specimen and therefore by comparing these two signals, gives the direct measurement of the Magnetization, M .

A schematic diagram of a VSM is shown in figure 4.19.

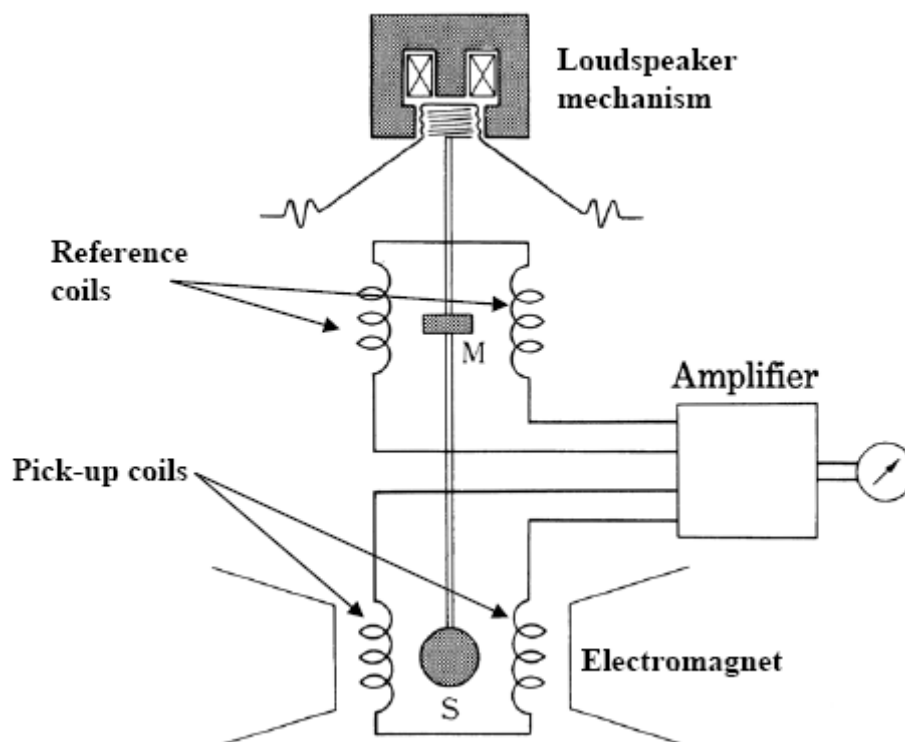


Figure. 4.19. A schematic diagram of a VSM [15].

The sample (S) is mounted on a small plastic cylinder (which is diamagnetic and has no magnetic response) using some silicone grease and is attached to a glass rod, which is then placed in the VSM. The sample is oscillated vertically in a region of uniform field between two magnets, and it is driven by a loudspeaker mechanism. The frequency is usually near 80Hz and the amplitude is 0.1-0.2mm.

At the upper end of the glass rod there is a reference in the form of a small permanent magnet (M) situated between a set of reference coils. Therefore the AC signal induced in the pick-up coils (according to the Faraday law of electromagnetic induction) by the magnetic field of the sample is compared with the signal from the permanent magnet and is converted to a number proportional to the magnetic moment. This means that the set-up is insensitive to changes in the vibration amplitude and frequency and also it is a non-destructive method and easy to use. The VSM has a high sensitivity and can measure magnetic moments in the range of μemu and its accuracy is better than 2%. However, the specimens used have to be rather short to fit

between the pole pieces of the electromagnet and so the hysteresis loops obtained are not intrinsic because of demagnetizing effects associated with using short specimens. For quantitative work, the VSM was calibrated with a bulk sample of Ni of known saturation magnetization. This sample was small enough to assume that all flux produced will cut the sense coils. However, thin film samples are normally grown on $10 \times 5 \text{ mm}^2$ substrates and so in certain orientations not all of the magnetic flux from these larger samples will cut the sense coils. From a study has been carried out on this VSM [8] it was found that the same M_s was obtained for a $2 \times 2 \text{ mm}^2$ sample as for a $10 \times 5 \text{ mm}^2$ (long axis parallel to applied field) but a reduction in M_s of 23 % was found when the short axis of the $10 \times 5 \text{ mm}^2$ was parallel to the applied field. Therefore, in general $5 \times 5 \text{ mm}^2$ samples were used for VSM work and for the case of measurements down to 5 K (using a ^4He cryostat) $4 \times 4 \text{ mm}^2$ were used so that the sample could be fit and rotated in the fused silica cryostat glass capillary.

4.8 FOCUSED ION BEAM (FIB)

This section gives a brief introduction to FIB and further details can be found elsewhere [16]. The Focused Ion Beam technique (FIB) was mainly developed during the late 1970s and early 1980s, and the first commercial instruments were introduced more than a decade ago [17]. The technology enables localized milling and deposition of conductors and insulators with high precision. Focused ion beam systems effectively combine together a scanning ion microscope and a precision milling system. By scanning the ion beam over a specimen and collecting the ion beam-induced secondary-electron or -ion signal an image of the surface is formed. Figure 4.20 is a schematic diagram of a FIB ion column. The structure of the column is similar to that of a scanning electron microscope, the major difference being the use of a gallium ion (Ga^+) beam instead of an electron beam. The ion beam is generated from a liquid metal ion source (LMIS) by the application of a strong electric field. This electric field causes the emission of positively charged ions from a liquid gallium cone, which is formed on the tip of a tungsten needle. The Ga LMIS is used because of its stability, simplicity of operation and the fact that Ga ions give good sputtering yields due to its low Fermi energy. A vacuum of about 1×10^{-7} mbar is maintained inside the column. After a first refinement through the spray aperture, the ion beam is condensed in the first electrostatic lens. The upper octopole then adjusts the beam stigmatism. Using the variable aperture mechanism, the beam current can be varied over four decades, allowing for both a fine beam for high-resolution imaging and a heavy beam for fast and rough milling. The blanking deflector and aperture enable blanking of the beam away from the sample into a Faraday cup.

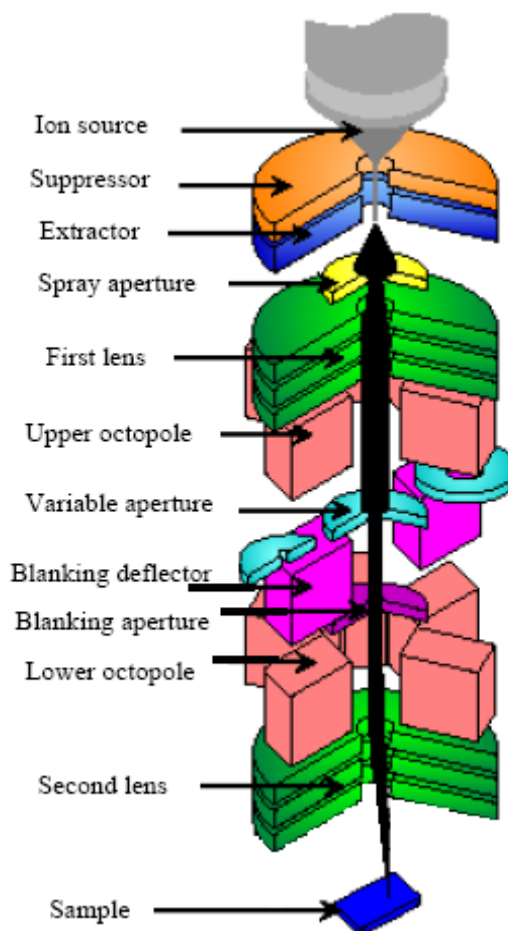


Figure 4.20. A schematic diagram of a FIB ion column [17].

This system not only protects the sample from constant milling, but can also measure the current. The lower octopole is used for scanning the beam over the sample in a user-defined pattern. In the second electrostatic lens, the beam is focused to a fine spot, enabling a best resolution in the sub 10nm range. A secondary electron detector is used to collect the secondary particles for imaging. Figure 4.21 is a schematic showing the principle of FIB imaging (a) and milling (b). During FIB imaging the finely focused ion beam is raster scanned over a substrate, and secondary particles (neutral atoms, ions and electrons) are generated in the sample. As they leave the sample, the electrons or ions are collected by the secondary electron detector. FIB imaging inevitably induces some damage to the sample. Most of the Ga^+ ions that arrive at the sample surface enter the sample, leading to ion implantation. The depth of the implanted region is related to the ion energy and the angle of incidence. When the Ga^+ ion energy is 30keV, the implantation depth in SiO_2 is $25 \pm 8\text{nm}$ [17]. Also, some milling always occurs when the ion beam is scanned across the sample surface, although the milling effect can be reduced by using a fine ion beam (fine spot and low ion current). The removal of sample material is achieved using a high ion current beam, as shown in Fig. 4.21 (b). The result is a physical sputtering of the sample material. The

milling process was calibrated using 'end-point detection'; this is a real-time graph of the average brightness in the milling area. An insulator will appear darker than a conductor since the secondary electron yield of the latter is much higher. This effect results in a typical end-point detection curve as shown in Figure 4.22.

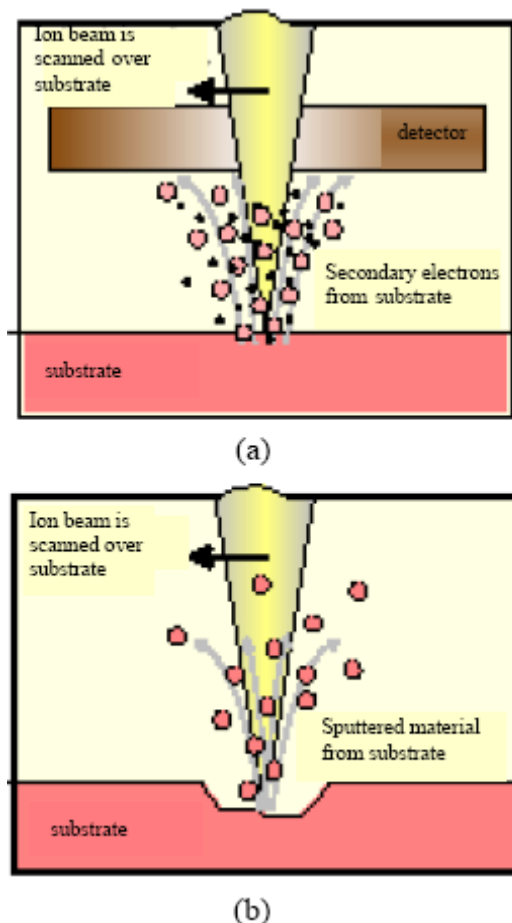


Figure 4.21. Schematic diagrams showing the principle of FIB (a) imaging and (b) milling [17].

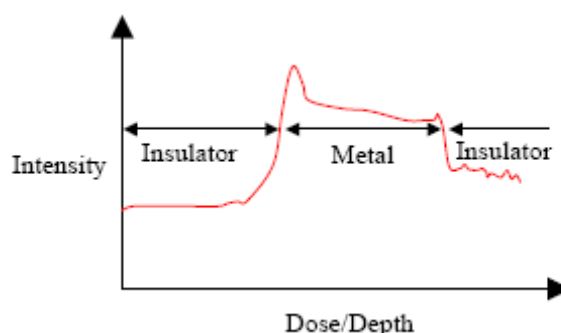


Figure 4.22. End-point detection. The graph shows the average brightness in the milling area as a function of the delivered dose. This is used to monitor the milling operation in real time. The insulator-metal-insulator transition is clear.

BIBLIOGRAPHY

- [1] D. B. Williams and C. B. Carter, *Transmission electron microscopy*, (Plenum, New York, 1996).
- [2] J. I. Goldstein, D. E. Newbury, P. Echlin, D. C. Joy, A. D. Romig, C. E. Lyman, C. Fiori, and E. Lifshin, *Scanning Electron Microscopy and X-ray Microanalysis*, 2nd ed. (Plenum Press, 1992).
- [3] H. Bubert and H. Jenett (eds.), *Surface and Thin Film Analysis, Principles, Instrumentation and Applications*, (Wiley-VCH, Germany, 2002).
- [4] C. B. Boothroyd, *Microanalysis in electron microscope*, Graduate lecture course, University of Cambridge, (2004).
- [5] C. A. Wallace, R. C. C. Ward, *J. Appl. Cryst.* **8**, pp. 255-260 (1975a).
- [6] C. A. Wallace, R. C. C. Ward, *J. Appl. Cryst.* **8**, pp. 545-556 (1975b).
- [7] J. A. Leake, *Techniques of Materials Reserch*, (University of Cambridge, 1997).
- [8] L. J. Singh, *PhD Thesis*, University of Cambridge (2005)
- [9] G. Thomas and M. J. Goringe, *Transmission Electron Microscopy*, (John Wiley and Sons, 1979).
- [10] M. Ohring, *The Materials Science of Thin Films*, (Academic Press, 1992).
- [11] Digital Instruments Veeco Metrology Group, Training Notebook (1999), <http://www.veeco.com/html/library.asp>
- [12] D. Morecraft, *PhD thesis*, University of Cambridge, (2003).
- [13] J. H. Durrell, *PhD thesis*, University of Cambridge, (2001).
- [14] S. Foner, *Rev. Sci. Inst.*, **30**, 548 (1959).
- [15] S. Chikazumi, *Physics of Ferromagnetism*, 2nd ed. (Oxford Science Publications, 1997).
- [16] J. Melngailis, *J. Vac. Sci. Technol. B*, **Vol. 5**, No. 2, 469, Mar/ April (1987).
- [17] S. Reyntjens, R. Puers, *J. Micromech. Microeng.* **11**, 287 (2001).
- [18] H. P. Klug and L. E. Alexander, *X-ray Diffraction Procedure For Polycrystalline and Amorphous Materilas*, 2nd ed. (John Wiley & Sons, 1974).



CHAPTER 5
RESULTS AND DISCUSSIONS

“The difficulty lies, not in the new ideas, but in escaping the old ones, which ramify, for those brought up as most of us have been, into every corner of our minds.”

John Maynard Keynes.

In this section, the results collected from different characterization techniques are mentioned and further discussed.

5.1 TRANSITION TEMPERATURE (T_c)

As explained in section 4.6, the transition temperature measurement was done for almost all the deposited films with different chemical compositions after each experimental run. The main goal was obviously to grow a film with the highest amount of gadolinium (Gd) that also shows superconductivity, simply because more ferromagnet material brings stronger magnetic response to the material.

In the preliminary deposition experiments, the superconductivity was completely suppressed by the existence of ferromagnet material even in the samples with highest amount of niobium (Nb). Figure 5.1 shows a typical R - T curve of the samples which did not show superconductivity.

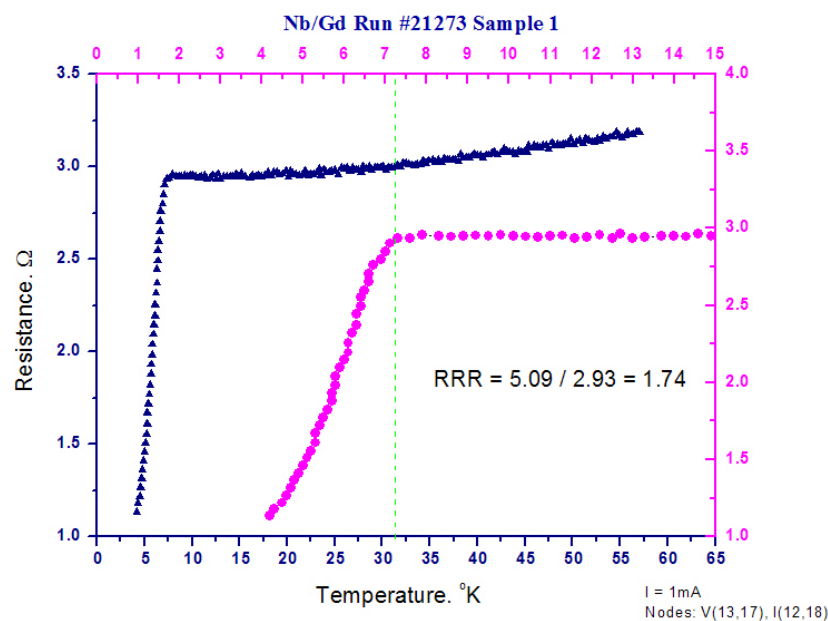


Figure 5.1. A typical R - T curve for samples which did not show superconductivity because of lack of segregation. The pink graph along with axes, are the magnified part of the main graph for low temperatures.

Having a superconductor-ferromagnet hybrid system requires having ferromagnetic grains or islands in the superconductor matrix, because having a network which is ferromagnetic but with superconducting matrix is very unlikely to show the superconductivity (continuous superconductivity) as the ferromagnetic islands are placed very close to each other. On the other hand if we have an excess of superconductors, i.e. on average the ferromagnetic islands are not connected to each other but the superconductors are, in this case, it is the percolative pathway between the superconducting matrix that determine when we do transport

measurement. So the minimum thickness of these ferromagnetic islands is the cause that determines what we actually measure, i.e. if the minimum thickness of the intermediate ferromagnetic grains is comparable to coherence length, then the superconductivity measure in the transport measurement is going to be strongly suppressed. So the reason for not having superconductivity in preliminary experiments is really not the lackage of Nb (on the basis of the powers of the magnetrons), but is just a need for better segregation of the elements. In these films, the scenario can be visualized as in some regions in the film, the accumulation of Gd islands is high enough that the percolative pathway can not pass through and the superconducting pathway is not fully connected or in other words, the superconducting channels are too narrow (it hasn't been segregated fully) that the superelectrons suppress in these regions because of the proximity effect.

After finding the optimum parameters for target magnetron powers and for heater current ($P = 30W$ for Nb and $P = 4.95W$ for Gd and the heater current of 30A), all the deposited films showed superconductivity. The expected transition temperature of bulk Nb is $9.5\text{ }^{\circ}\text{K}$ [1] but it is less than that for thin film of Nb and it is also expected that the transition temperature of the nanocomposites of Nb and Gd would be less than that of pure Nb in thin film because of the proximity of the Gd. The average transition temperature of between 7 to 9°K was found depending on the amount of Gd in the sample and how well the vacuum in the system was.

In figure 5.2 a typical of deposited film which showed superconductivity is shown.

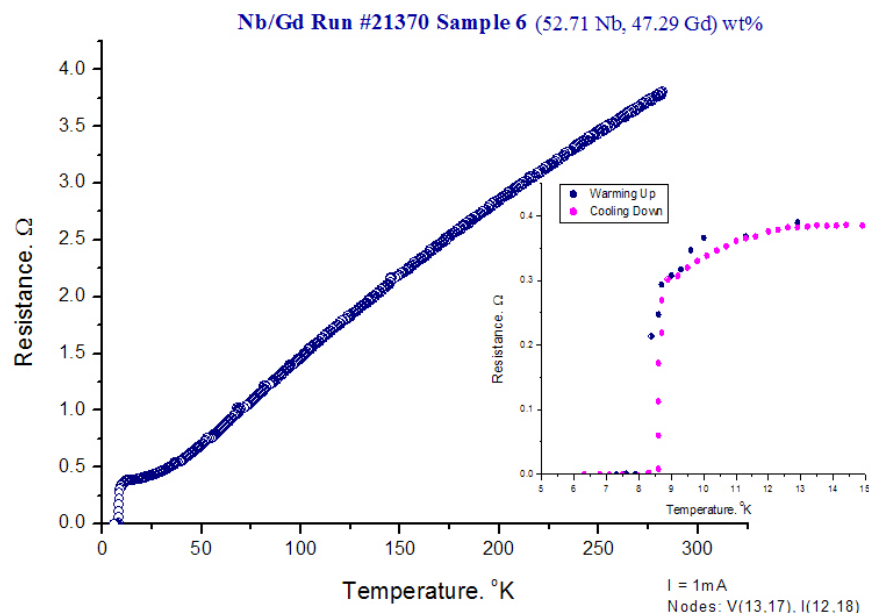


Figure 5.2. A typical R-T curve for one of the sample which did show superconductivity. The onset is the zooming of the transition temperature area done both while warming up and cooling down to avoid hysteresis.

Another important factor which was calculated using the R-T curve was Residual Resistance Ratio (RRR). Residual Resistance ratio is the ratio of the resistance at room temperature to

resistance at zero Kelvin or in the case of superconductors the transition temperature. The electrical resistivity of metals arises from two main mechanisms: At room temperatures (300K) the collision of the conduction electrons with lattice phonons is the dominant mechanism, however, at liquid Helium temperature (4K), the lattice vibrations (phonons) are frozen and the resistivity of metals is dominated by collisions with impurity atoms and mechanical imperfections in the lattice [1]. It is worth to note that the rates of collisions with these two methods are often independent of each other to a good approximation and by switching the electric field off, the momentum distribution would relax back to its ground state with the net relaxation time:

$$\left\{ \begin{array}{l} \frac{1}{\tau} = \frac{1}{\tau_L} + \frac{1}{\tau_i} \\ \tau_L : \text{collision time for scattering by phonons} \\ \tau_i : \text{collision time for scattering by imperfections} \end{array} \right.$$

Therefore the net resistivity can be given by the so-called **Matthiessen's rule** [2], an empirical observation which is quite useful for analyzing experimental data:

$$\left\{ \begin{array}{l} \rho = \rho_L + \rho_i \\ \rho_L : \text{resistivity caused by thermal phonons} \\ \rho_i : \text{resistivity caused by scattering of electron waves by static defects} \end{array} \right.$$

It's a good approximation to consider ρ_L independent of the number of defects if their concentration is small, and ρ_i independent of temperature. It was noted that by increasing the amount of Gd, the RRR increases or in other words the system becomes more dirty which is expected. The other factor affecting RRR is the quality of the vacuum of the system or the base pressure of the system before deposition. Poorer vacuums result in lower RRR (more impurities) and more suppression of the transition temperature of the deposited film.

5.2 ENERGY DISPERSIVE SPECTROSCOPY – SEM

In order to find the amount of Gd on each superconducting film, EDXS measurements were done. In order to check the homogeneity of the samples and reduce the measurement error, measurements were done at three different locations of the film and an average was taken as composition of the film. The results showed difference of within only 5% which shows the sputtered film can be considered homogeneous in the sense of spreading Gd islands in the Nb matrix. Also by choosing the Automatic Peak Determination tab in the EDXS software, the possibility of having any impurity in the film was rejected. The carbon peak observed is because some carbon atoms will evaporate from the carbon tape used to hold the sample. The

oxygen peak showed the existence of oxide in the film but the formation of oxides should not be a problem as its amount is not that much to suppress the superconductivity. In figure 5.3 a typical spectrum is shown. In the electron excited X-ray spectrum, the discrete energy lines are superimposed on a continuous background which is known as bremsstrahlung continuum ranging from zero to the primary energy of the electrons. The reason for this continuum is because of the fundamental laws of electrodynamics. Electrons are decelerated in the Coulomb field of an atom.

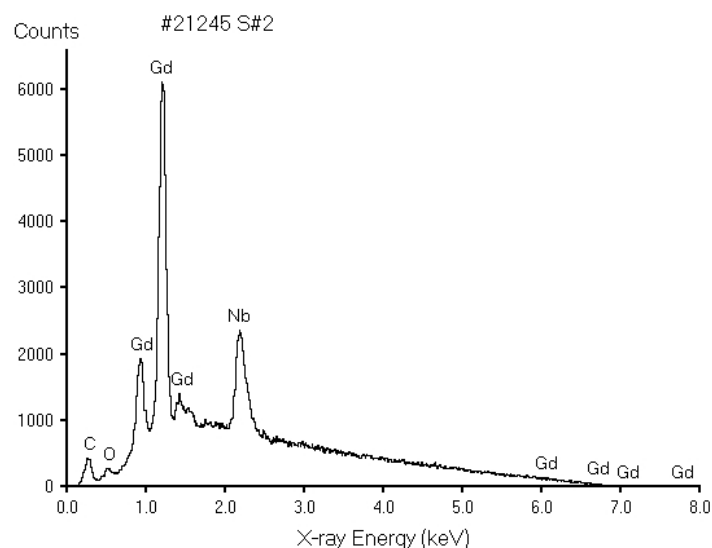


Figure 5.3. A typical spectrum of deposited sample (Gd rich sample)

Some crucial considerations for reducing the error and obtaining the most accurate results in EDXS measurements are mentioned as follow:

As explained in section 4.1, the width of the interaction volume, and hence the X-ray resolution, is typically about 2/3 of the electron range measured by K-O (Kanaya-Okayama) formula. Thus the X-ray resolution is better at lower accelerating voltages, and is much worse for lower atomic number specimens. In other words, the thicker the specimen the bigger the interaction volume and hence less lateral X-ray resolution is achievable.

The thickness of the sapphire substrate used in this experiment was about 1 mm. The sputtered films' thicknesses were different but were in the range of 150 to 300 nm. Given above explanations, it was crucial to control the size of the interaction volume to make sure that the detected signals are coming dominantly from the sputtered film rather than the substrate. According to the K-O formula, the high atomic number of the film constituents was in favor of a small interaction volume. Moreover, it was also important to control the penetration depth of the electron beam or the accelerating voltage of the electrons.

This was achieved by performing Monte-Carlo simulation to find the best accelerating voltage for electrons. A film thickness of 200nm as an average was considered for these simulations. The accelerating voltage assuring most of the signal that carry chemical

composition data would come from the film but not the substrate was found to be 7 keV. Also it helps to keep the interaction volume as small as possible, hence increasing the X-ray lateral resolution. As it is obvious from the simulation (figure 5.4), the interaction volume radius is about 160nm. The backscattered electrons are shown in red.

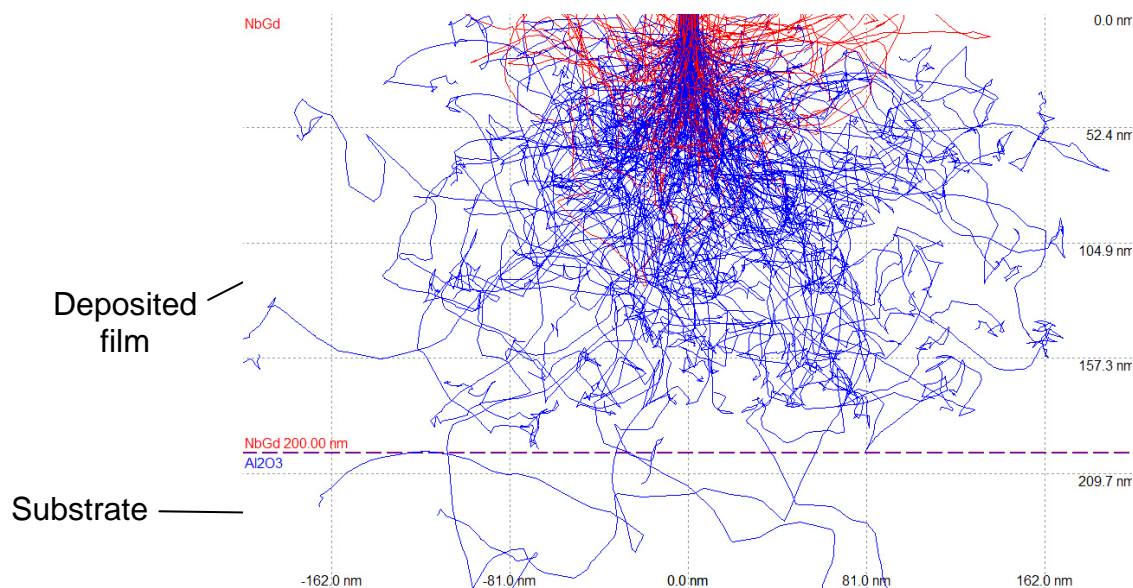


Figure 5.4. The Monte Carlo simulation done for 7keV beam and 200nm film thickness. The backscattered electrons are shown in red.

Furthermore when choosing the incident beam energy, this energy should be at least two times higher than highest peak energy of the elements to be detected. In other words, the energies of at least one of K, L or M lines of the element which is probable to be present in the specimen, should be half of the selected incident beam energy. This is because X-ray signals come from considerable depth in the specimen and on the way out, there is a high probability that they may be absorbed again. Therefore by choosing the energy of the incident beam two times higher than at least one of the possible characteristic excitation energies of the elements to be detected, one can ensure that the generated characteristic X-rays have enough energy to reach the detector. At least one of the characteristic energy levels of the elements suspected to be present in the specimen (mainly Nb and Gd) was lower than 7keV. However, it should be mentioned that choosing a low accelerating voltage incident beam, apart from making it very hard to focus, caused a drastic aberration in the beam (nature of low voltage beam) which required constant adjustment of the beam. The other factor affecting the amount of signal reaching the detector (resulting in low error) is the Working Distance (WD)

which is the distance from the top of the sample holder¹ to the top of the electron beam. For best results, the working distance should be set to 10mm (1cm). This matter was troublesome when checking the composition of the sputtering targets because their thickness is about 2-3 cm and their awkward shape makes it hard to align their top with the top of the sample holder, hence causing some error in Working Distance adjustment. However, their huge thickness allowed using bigger accelerating voltages which means much stronger signals that cover the error caused by misalignment of working distance.

Another important factor for having precise measurement is the Dead Time. The time constant τ is the time that the detector takes to process a pulse. It is typically from a few to 40 μs and can usually be changed by the user. Short τ allows higher count rates to be processed. Long τ gives better energy resolution as the electronics has more time to process the pulse. The detector cannot process further pulses while one is being processed hence it is “dead” for this time. If a further pulse arrives while the first is being processed then the dead time is increased. The maximum processing efficiency is reached at about 50% dead time. Much higher input count rates saturate the detector (100% dead time). In practice it is good to work with between 30 and 50% dead time which in this experiment dead time of 40% was chosen.

EDXS measurements showed the chemical composition range expected in the films (Section 3.2), was achieved. Although no precise control was possible in the chemical compositions, however, the qualitative change in the amount of Gd in different samples gave the opportunity to investigate the increase of the amount of Gd, in the samples properties.

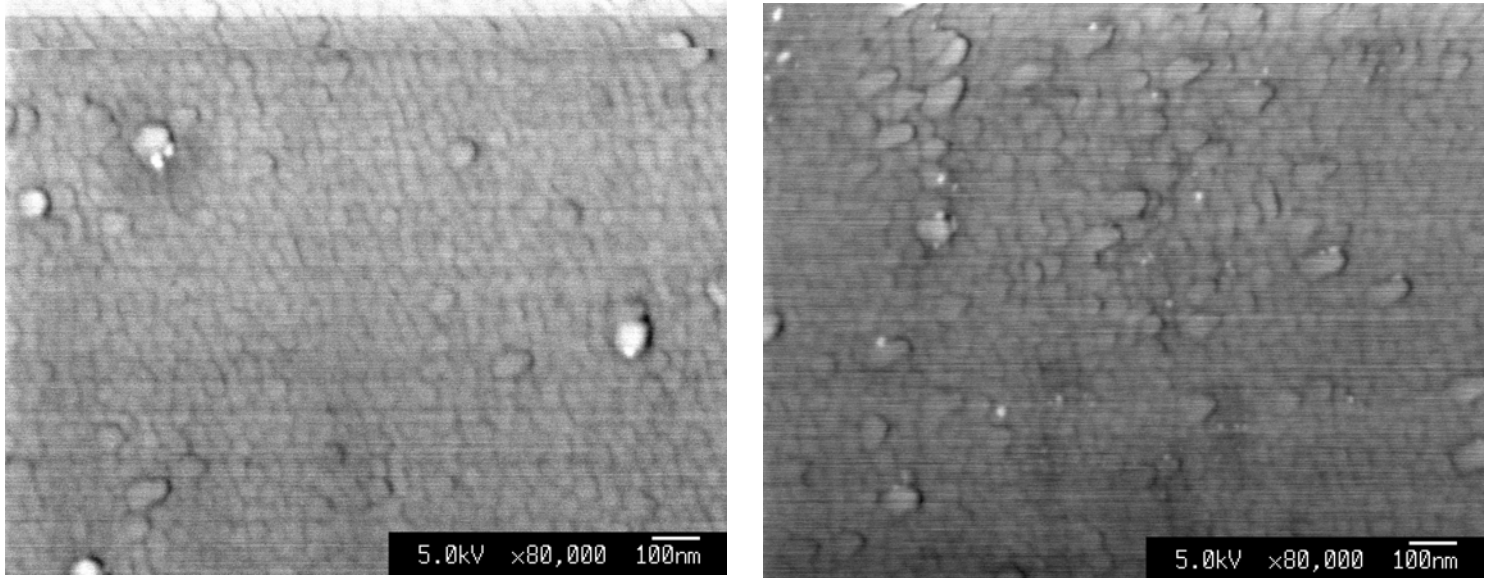
5.3 MICROSTRUCTURE IMAGING & TOPOGRAPHY

Observation of microstructure of the Nb/Gd in the composite revealed the very fine features and grain structure in the range of nanometer. Obviously, SEM is not able to resolve such a fine structure due to its limited resolution, so Field Emission Gun Scanning Electron Microscopy (FEG-SEM) with its ability to resolve much finer structures, was exploited for taking images of the microstructure of the nanocomposite. Figure 5.5(a) shows the FEG-SEM image of secondary electrons and 5.5(b) is the image taken with focused Ion Beam (FIB), formed from secondary electrons. Both images clearly show a phase separated network of Nb and Gd which is what expected, with distribution of apparent grain ranging from 20-50 nm although the larger grains may contain smaller particles that could not be resolved. The poor contrast has made it difficult to differentiate between Nb and Gd phases. For some unknown

¹ The top of the sample holder should be aligned with the top of the sample in order to reduce the error because the computer considers the Working Distance from the top of the sample holder regardless of the height of the sample.

reason the Backscattered signal in FEG-SEM was too weak to acquire an image. These problems, suggests using a more powerful technique such as Transmission Electron Microscopy (TEM).

a)



b)

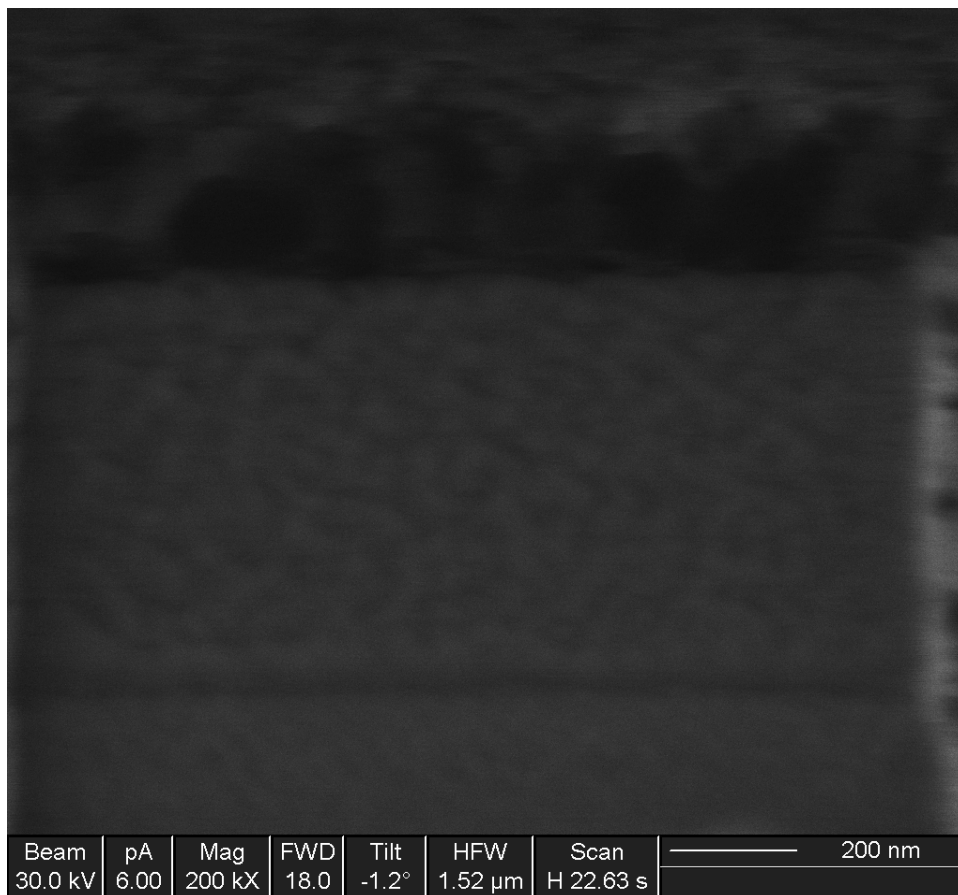


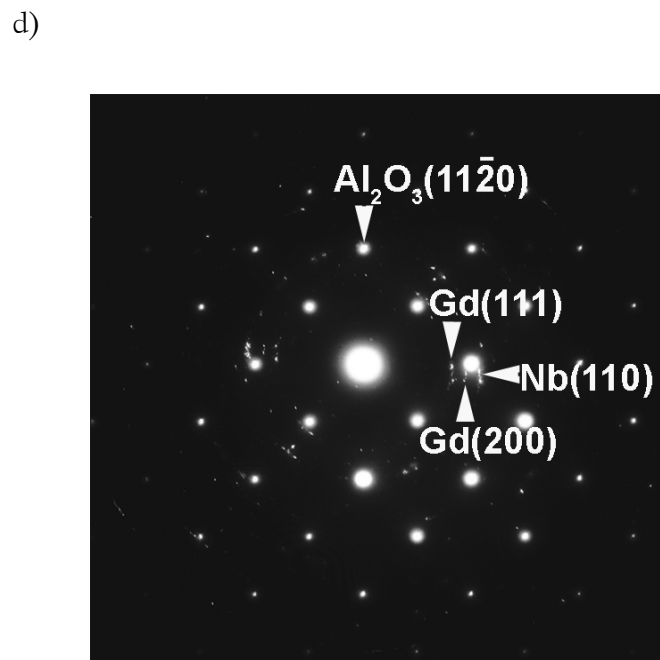
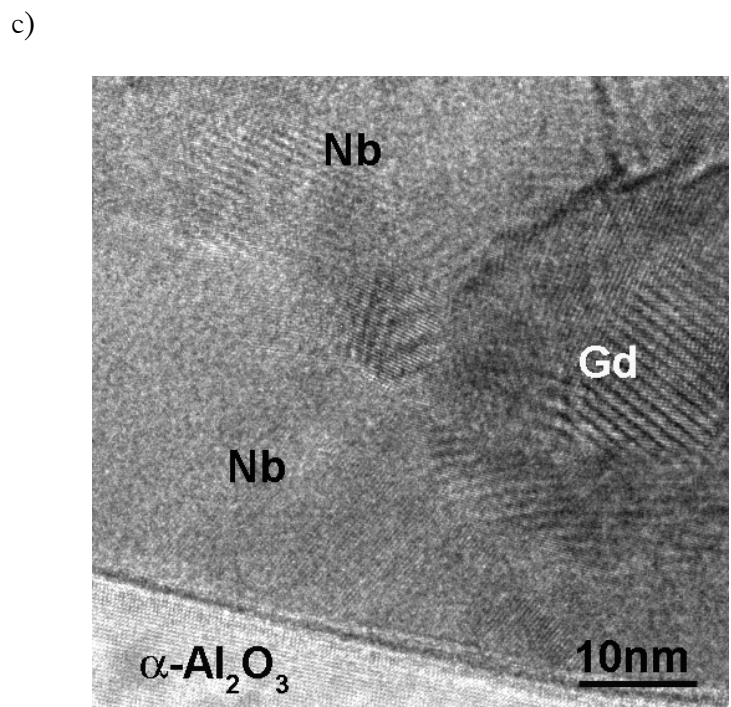
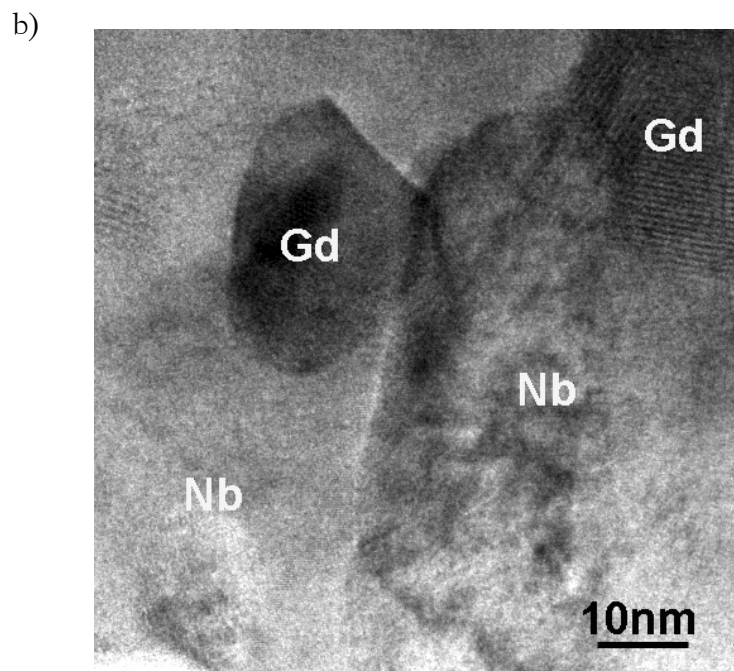
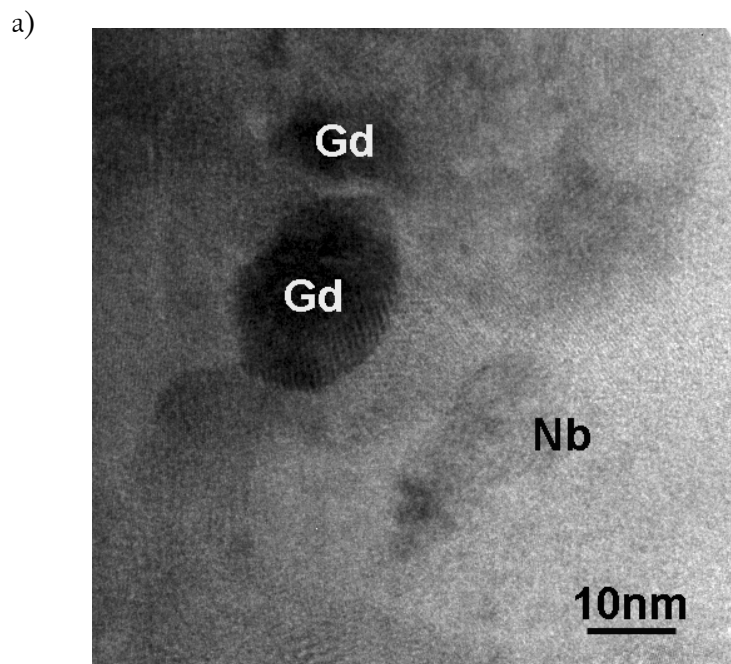
Figure 5.5. a) FEG-SEM images (secondary electrons images) taken from the nanocomposites showing features with sizes less than 50 nm. b) FIB image of the nanocomposite showing percolation pathway.

In order to obtain a much better contrast between Nb and Gd and also differentiate between Nb and Gd grains along with a larger magnification and better resolution of the individual grains, Transmission Electron Microscopy (TEM) and High Resolution Transmission Electron Microscopy (HRTEM) techniques were used².

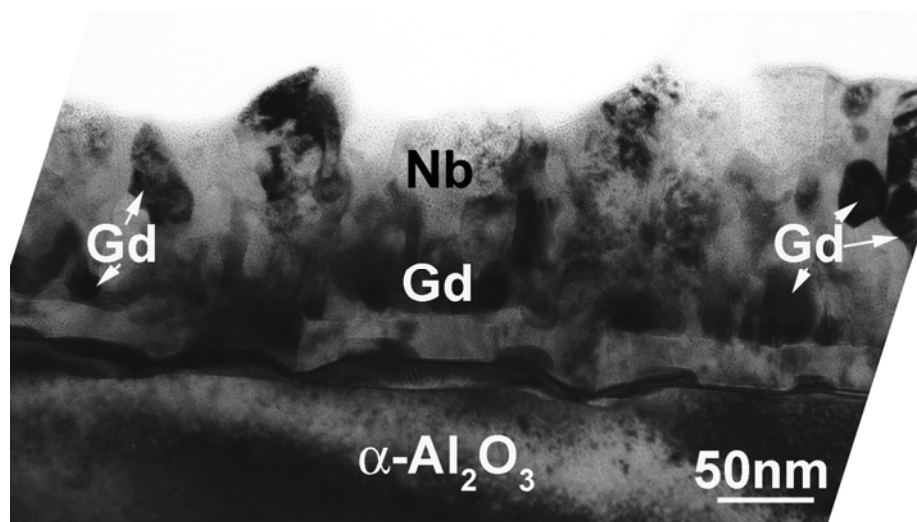
Images A, B and C clearly show the distribution of Gd grains in the superconductor Nb matrix. The average grain size of 20nm is observed for Gd and the sharp interface between Nb and Gd is clearly seen in image C. No sign of intermixing or formation of intermetallic phases is seen in the interfaces of Nb and Gd. Images E and F show diffusion of Nb into the substrate which leads to alloying of Nb with aluminium (Nb₃Al). This matter is discussed more in the results obtained from X-ray diffraction.

In image D the diffraction pattern of the film is shown. Apart from sapphire, both Nb and Gd are crystallized during growth. This matter is further discussed in the results obtained from X-ray diffraction.

² The TEM and HRTEM images were taken by Haiyan Wang at the Los Alamos National Laboratory, US. (Current address: Electrical Engineering Dept. Texas A & M University, College Station, TX 77843-3128)



e)



f)

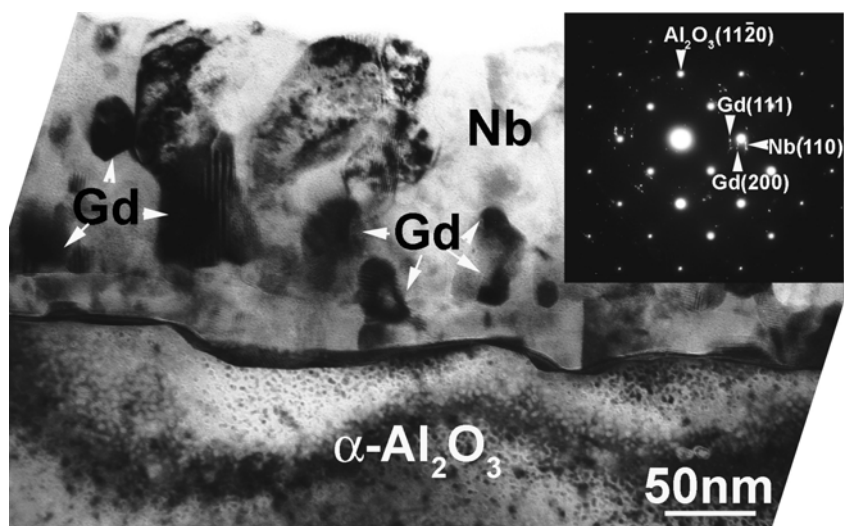


Figure 5.6. TEM and HRTEM images of the nanocomposite film. Image “d” shows diffraction pattern of the deposited film. “e” and “f” show the cross sections of the deposited film.

AFM images taken to show the topography of the surface film and also to check the grain sizes. Figure 5.4 shows an AFM image of the nanocomposite film, which is similar to the FEG-SEM image, except the grooved boundaries cannot be seen. The grain shape is almost round. Once again there is a distribution of grain sizes, ranging from 10-60 nm. The rms roughness was 3.1 nm over an area of $1 \mu\text{m}^2$.

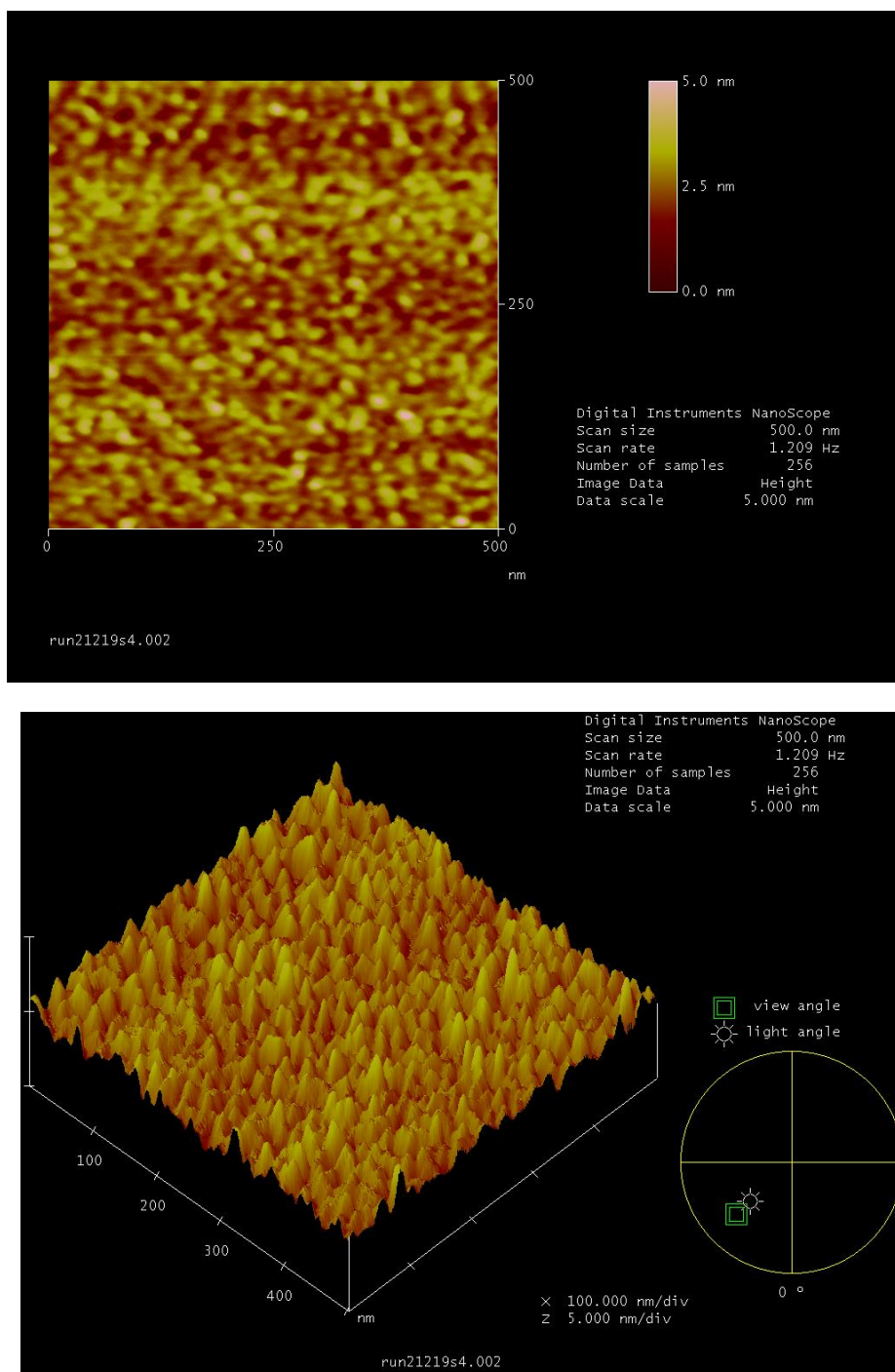


Figure 5.7. AFM images of the nanocomposite

5.4 X-RAY DIFFRACTION

For determining the phases present in the deposited nanocomposite, first a pure Nb and Gd film were deposited and the X-ray diffraction patterns of them were studied separately as a reference in order to find out any phase changes in Nb and Gd and also formation of any intermetallic compound or complex alloys during sputtering of the nanocomposite, although the TEM pictures showed that this is unlikely to happen. The reason for considering sputtered Nb and Gd patterns as reference rather than the bulk targets is to check whether there is any preferential orientation for growth as well as any phase change during sputtering process. It should be noted that because of the nature of sputtering process, existence of internal stresses and strains in the sputtered film is inevitable. Therefore some Bragg angles corresponding to the powder samples mentioned in the ICDD cards could be shifted in the thin film samples due to the mentioned stresses. Also in the case of preferential growth of the film or the so-called texturing, the intensities could be completely altered from the ones predicted in powdered samples. Therefore unlike the powdered specimens, the diffraction study of the thin film samples could be tricky!

The X-ray diffraction pattern of the sputtered Gd film acquired over night is shown in figure 5.8. The best matching data obtained from ICDD database, is shown below the image. The Gd crystal structure in the bulk form is hexagonal (*hcp*, $a = 3.636 \text{ \AA}$, $c = 5.783 \text{ \AA}$); however, as the HRTEM pictures of the microstructure show (section 5.3), the Gd average grain size is about 30 nanometers which bring the possibility of change in the crystal structure or physical properties due to finite size effects. When the crystallite size of a ferromagnetic material is reduced in one or more dimensions to the nanometer range, the magnetic properties are expected to change dramatically and some consequences may arise from this finite size of the crystallite grains.

The intricate diffraction pattern of pure Gd suggests the high chemical activity of it which as will be discussed later, has some consequences on the growth of nanocomposite. Careful studies of the diffraction pattern shows crystallization of Gd in both *hcp* and *fcc* phases. No single orientation is preferred since majority of possible reflections are observed for both phases; however, comparing the peak intensities with reference data, one can qualitatively conclude that there is more than one preferential growth direction for both crystallite phases of Gd. Having a lot of reflections, make it very hard to quantify the texturing in each preferential orientation. A Ward-Wallace (section 4.2.3) image of pure Gd measured with a densitometer could elucidate the amount of orientation in such multiple-oriented samples. Krill *et al.* reported preparation of nanocrystalline Gd by inert-gas condensation and subsequent compaction which as indicated by diffraction measurements, was mostly in the equilibrium *hcp* phase and 5-10% formed in *fcc* phase with lattice parameter 5.29 \AA indicated.

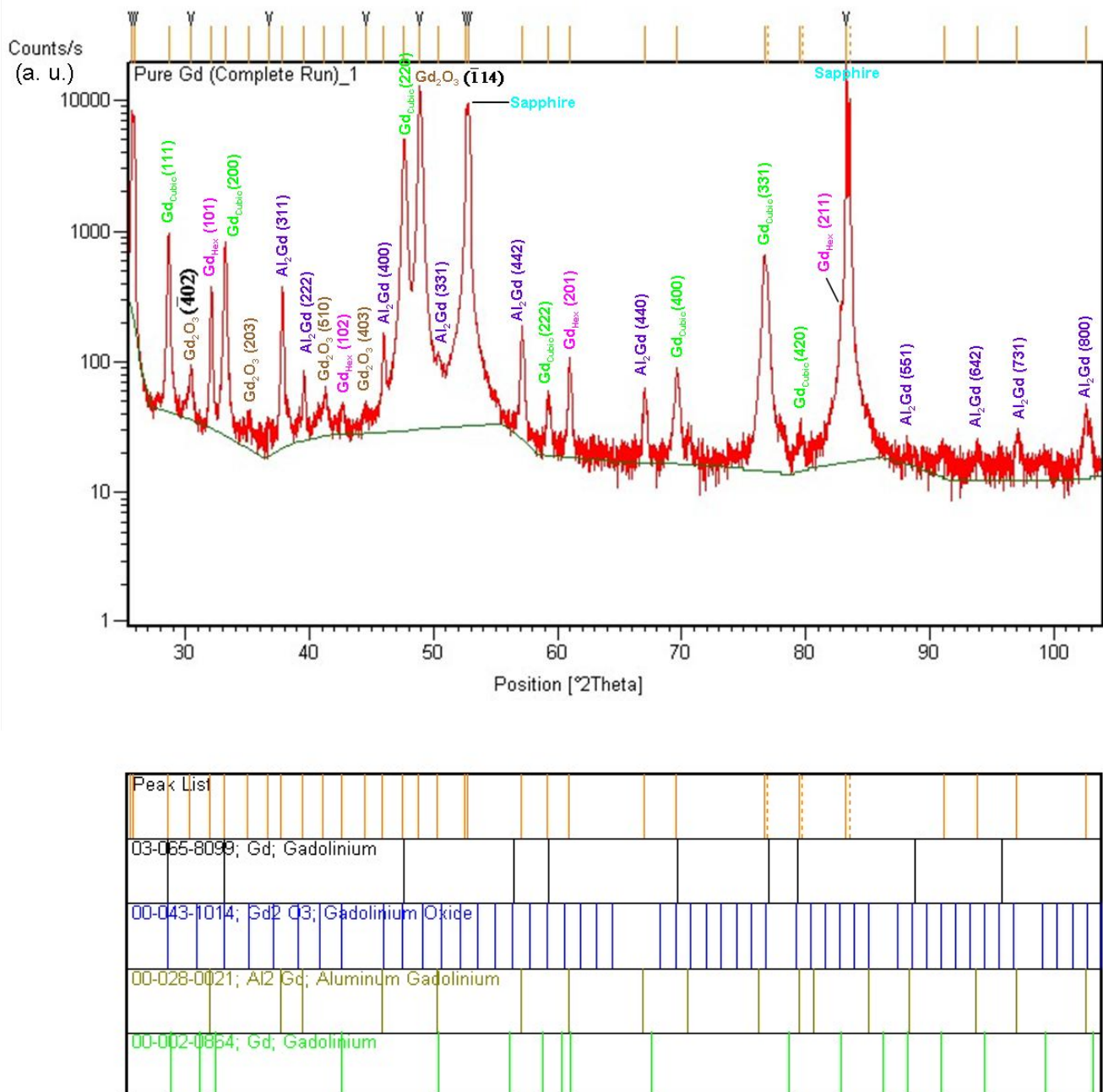


Figure 5.8. The X-ray diffraction of epitaxially grown Gd. The onset shows the peak lines for the sample (orange) and the Gd (red).

Apart from Gd, some of the unidentified peaks also match with Gd oxide (Gd_2O_3). Although the amount of oxygen read from the mass spectrometer was less than 10^{-8} mbar, however, the EDXS results also showed presence of small amount of oxygen in the system which can be attributed to the non-ideal vacuum of the system and also the probable leakage in the argon transfer pipe to the chamber. Being a highly active element and considering the relatively high substrate temperature, even the small amount of oxygen leads to formation of an oxide. In visual inspection of the pure Gd films, it was seen that the films are opaque which can be

attributed to the oxides in the upper layer of the film. Formation of Al_2Gd alloy was also revealed from the diffraction data.

The diffraction pattern of sputtered Nb film along with best matching phases from ICDD database is shown in figure 5.8. The formation of epitaxial Nb and Nb oxide due to the presence of minor amount of oxygen in the system is verified. Existence of three reflections points out the fact that Like Gd, no single preferred orientation was observed in pure Nb film, however, localized texturing in (220) and (200) reflections due to their huge intensities comparing to reference data is observed. The NbO_2 card taken from the ICDD database has huge number of reflections, hence one might argue matching three peaks is not enough to verify the existence of this phase because of high probability of matching due to high number of reflections, however, this data is supported by the EDXS data which rejects the existence of any other elements or compounds in the film rather than oxygen.

Ward-Wallace images of the nanocomposite have been taken overnight to show the different oriented reflections as well as revealing some qualitative data of amount of orientation in different reflections. As explained in section 4.2.3, the single dots stand for single crystal phase whereas a line depending on whether it has homogeneous or inhomogeneous width, stands for an unoriented and oriented phase respectively.

For Nb, (110), (210) and (220) reflections seem to be unoriented i.e. they get all the possible orientations in the reciprocal space, however, (200) reflection for Nb and (300) for Gd in hexagonal phase show semi texturing. What is meant by this statement is that some of Nb crystal planes in (200) direction, orient preferentially in the direction which is here dictated by the substrate and some, grow on random directions.

In the pure Nb sample, it was observed that some crystal planes tend to orient preferentially whereas some tend to grow randomly. In the nanocomposite sample with the buffer layer; however, the signal for Nb comes from both the Nb present in the buffer layer and in the film itself which makes it impossible to differentiate between them. The only preferential direction of growth for Gd is (300) and all the other reflections come from randomly oriented crystal planes. Both Nb(200) and Gd(300) directions are for the planes parallel to the sample surface (scattering vector normal to the surface) which due to the special cutting of the substrate, is parallel to $\{012\}$ family planes of sapphire. So in conclusion, some of the Nb (200) planes tend to grow preferentially on the $\{102\}$ planes of sapphire while the other grow in every direction. The same is true for Gd (300) planes. All the other crystallographic planes of Nb and Gd grow completely randomly.

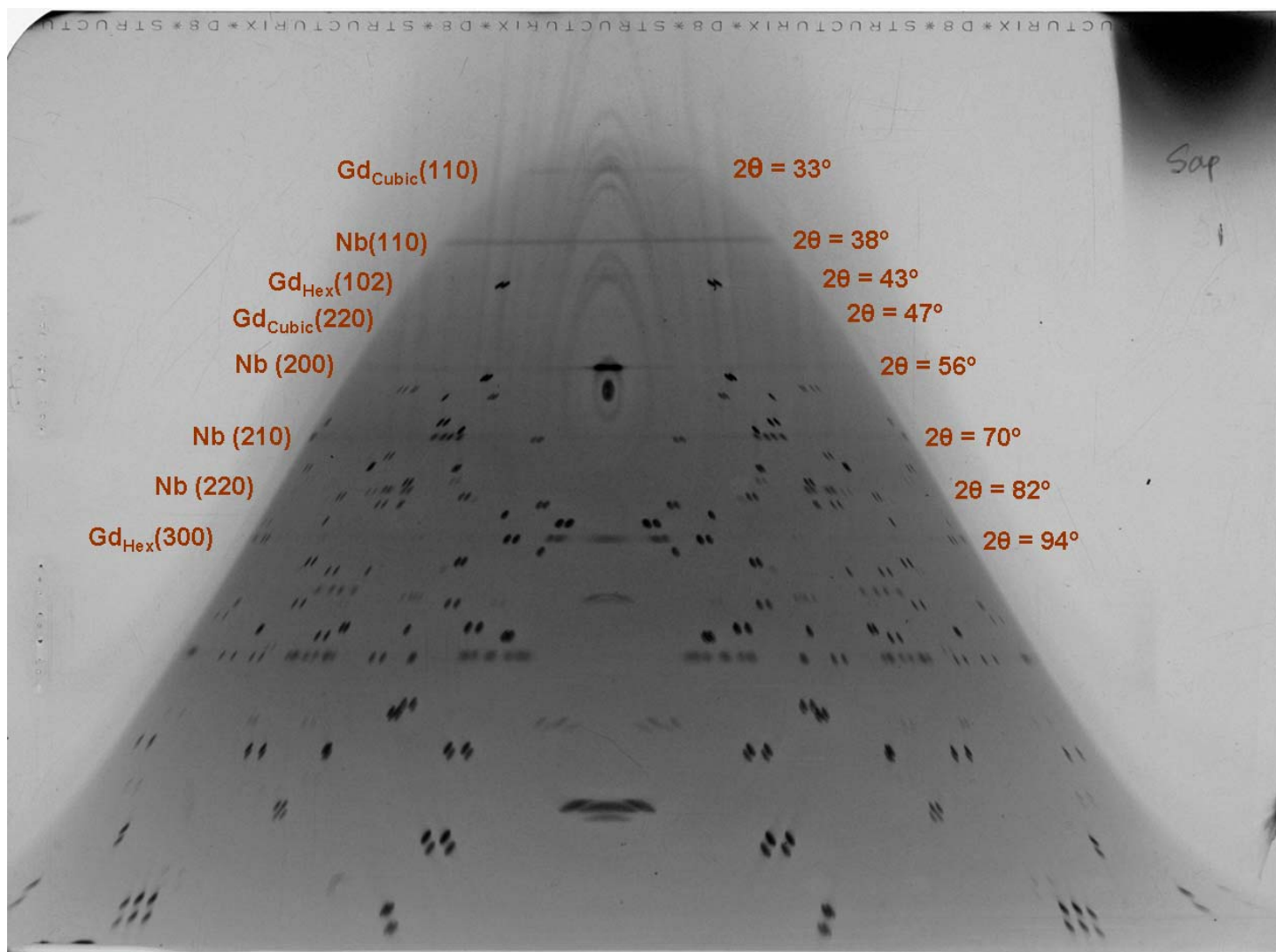


Figure 5.9. A Ward-Wallace photograph of the nanocomposite sample showing texture at specific orientations

The special geometry employed in the sputtering process (section 3.2) results in a range of variable chemical composition sputtered films from Gd rich for the sample sitting at one side of the heater close to the GD magnetron, to Gd poor for the one sitting at the other side close to Nb magnetron. Considering the high activity of Gd, increasing its amount is expected to have some consequences. For the films grown without any buffer layer and with a heater current of 50 Ampere (equal to approximately 1100 °C), it was seen that the Gd diffuses into the substrate and favours the formation of Al_2Gd alloy as also seen in the epitaxial grown pure Gd. Diffusion of Gd has other unfavorable consequence. In the epitaxially grown pure Nb film with the same heater specifications, no sign of diffusion of Nb into sapphire substrate was found; however, it seems that in the nanocomposite sample without any buffer layer, diffusion of Gd into sapphire provides the conditions (Kinetic energy) for the diffusion of Nb into sapphire and formation of AlNb_3 alloy which itself is a superconductor. The diffusion of

oxygen atoms at the Nb-sapphire substrate which accounts for Nb oxide have also been reported in epitaxially grown Nb/Gd multilayers [3]. As mentioned above, the diffraction pattern of pure Nb completely rejects any possibility of the diffusion of Nb to the substrate and forming the AlNb₃ alloy in the epitaxially grown Nb layer on the sapphire. Therefore a buffer layer of Nb is grown on the sapphire substrate before growing the nanocomposite to hinder the diffusion of Nb or Gd from the nanocomposite into substrate and possible chemical reactions.

The X-ray pattern for a series of samples sputtered at one deposition run, containing different amount of Gd taken overnight and with same parameters, is shown in figure 5.9 all in one for the sake of comparison, with the amount of Gd increasing from upper sample to lower one. Two extremely sharp and strong peaks of sapphire are closely seen close to 26° and 52°. Phase identification is done on the top part of the image. It is clear that Nb buffer layer has hindered diffusion of Gd into substrate and therefore formation of Al₂Gd and AlNb₃ alloys is being avoided; however, as the amount of Gd is increased, one can qualitatively say by looking at NbO(111), NbO(200), Nb₂O₅(831), Nb₂O₅($\bar{5}31$) and Nb₂O₅($\bar{8}04$) peaks that the amount of Nb oxide is increased. A possible explanation could be by introducing Gd to the system, diffusion of oxygen atoms from sapphire to the film become easier and more favourable as also have been reported elsewhere [3]. Both cubic and hexagonal Gd show several different reflections and by increasing the amount of Gd it seems that the growth is taken place in all these orientations. The same is true for Nb.

In Bragg-Brentano diffraction geometry, one can only detect part of the reciprocal space with scattering vector normal to the crystal planes. Therefore *out-of-plane* lattice parameter of crystalline phases can be found by relating the Bragg formula and the unique relationship between crystal structure and plane indices. However, the error arises from sample displacement always affect the measured 2θ s with respect to reference angles³.

$$\Delta(2\theta) = 2D (\cos\theta) / R$$

$$\left\{ \begin{array}{l} \Delta(2\theta) : \text{specimen displacement} \\ D : \text{Sample Displacement} \\ R : \text{Diffractometer radius, 157 mm here} \end{array} \right.$$

In other words, the angles measured in diffraction data should be corrected with respect to the value calculated here. The substrate peak can be considered as reference and the sample displacement calculated for that then added to other measured 2θ s.

³ Of course as mentioned earlier, usually stresses and strains present in atomic scale will increase the change of 2θ .

After correcting the measured 2θ s, depending on the interested crystal structure, the lattice parameter(s) can be calculated with related formulas given in textbooks. Phase identification done before determined cubic structure for Nb and both cubic and hexagonal for Gd. The relationship between plane indices and lattice parameter for cubic and hexagonal systems are as follow.

$$\text{Cubic} : \frac{1}{d^2} = \frac{h^2 + k^2 + l^2}{a^2}$$

$$\text{Hexagonal} : \frac{1}{d^2} = \frac{4}{3} \left(\frac{h^2 + k^2 + l^2}{a^2} \right) + \frac{l^2}{c^2}$$

However, in thin films usually the single crystal substrate peak is very intense and in order to avoid any damage to the detector is skipped or a ω -offset is deliberately put to decrease the signal coming from the substrate which in both cases affects the 2θ value of the substrate, hence it can not be used as a reference for finding sample displacement error. It should be mentioned that the reference angles of present phases can not be used as reference either (refer to footnote 2). For solving this problem, all the samples were mounted again in the diffractometer and one of the weak substrate peaks was chosen and scanned through in 2θ mode. The difference between the 2θ values measured and the values measured with the deliberate ω -offset was recorded and added to the $\Delta(2\theta)$ value calculated above. In this case, the difference in 2θ values of phases present in the film and reference can be considered only as a consequence of film stress.

For simplicity and because of weak and overlapping peaks between interested phases, Philips Highscore Plus[®] software was used to find the *out-of-plane* lattice parameter. The refinement of the unit cell parameters is performed by a least squares fit through the angular differences between measured peaks and indexed reflections, and by adjusting the 2θ zero or the sample displacement too. The information about unit cells and indexed reflections of the interested phases which had been identified before was then fed into as input for each phase and the refined cell parameter was calculated. Good quality peak positions are usually a must for successful unit cell refinements. One big challenge was close peaks of the different phases since they get contribution from both phases and are not an exact measure for each of the constituent phases, hence it was tried to pick peaks (for each phase) which uniquely belong to that phase and are not common with another present phases.

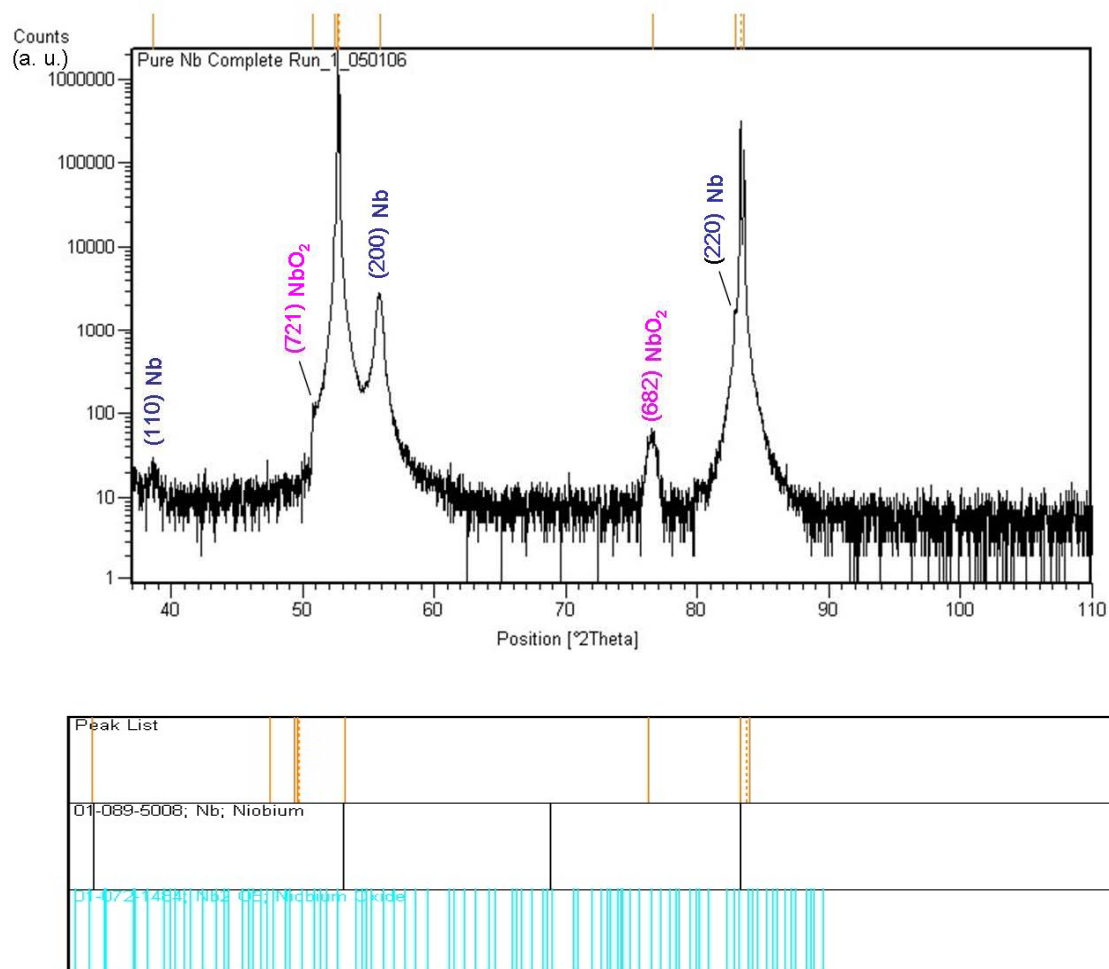


Figure 5.10. The X-ray diffraction pattern of epitaxially grown Nb.

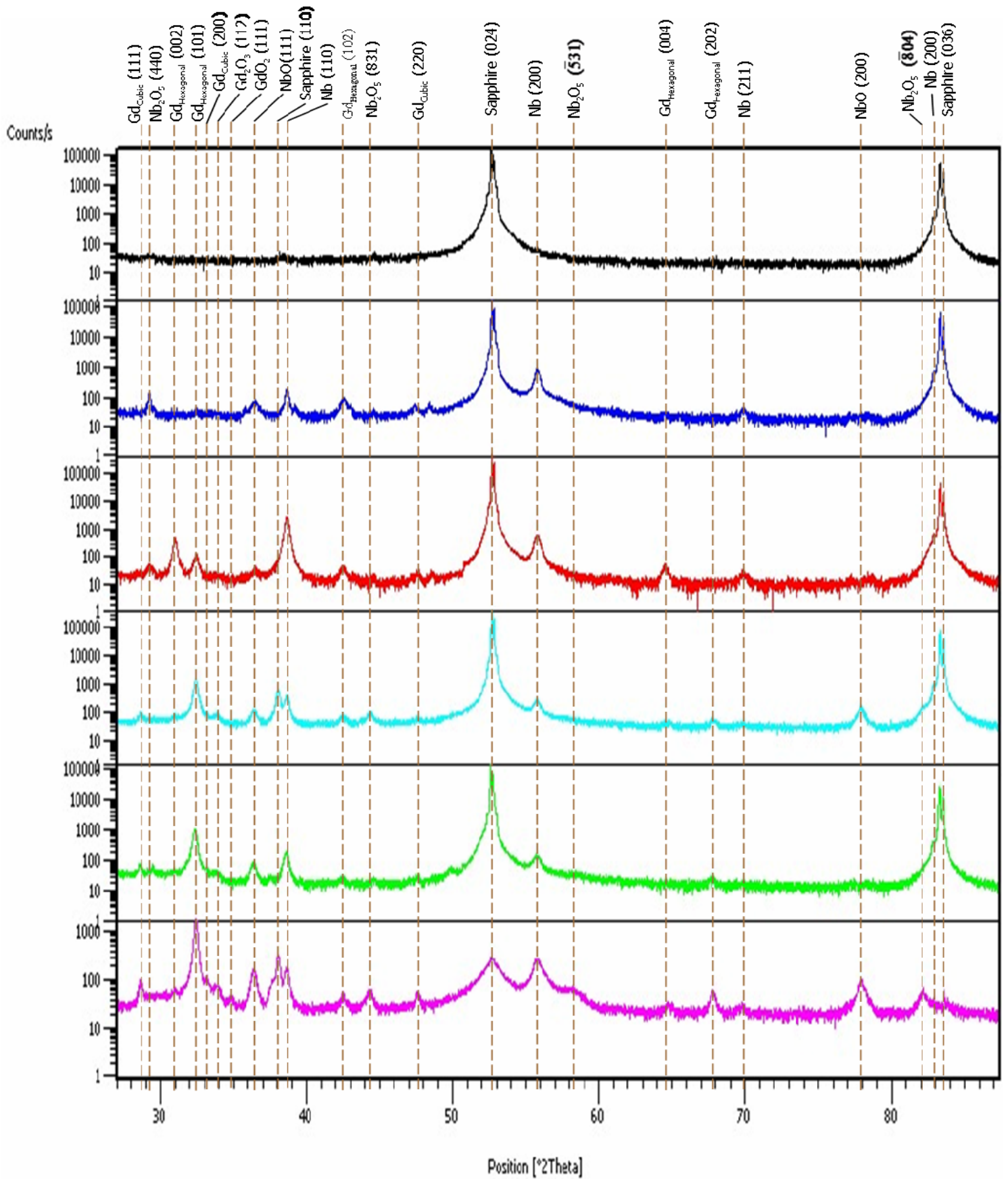


Figure 5.11. Diffractogram of 6 samples from one experimental run (the highest is Nb rich and the lowest is Gd rich)

As explained in section 4.2, the shape of an X-ray diffraction line (particularly the Full Width at Half Maximum or FWHM) can contain information about particle size (strictly the size of the coherently diffracting regions in the direction perpendicular to the reflecting planes) because in the thin film geometry, the perpendicular planes to the sample surface or (001) planes give rise to diffraction or in other words, the scattering vector is normal to the sample surface.

The average crystalline diameter can be obtained from the **Scherrer Equation**:

$$\tau = \frac{K\lambda}{\beta \cos \theta}$$

$$\left\{ \begin{array}{l} K = \text{shape factor (const. depending on the particle shape and the line indices typically} \\ \quad 0.85 - 0.9 \text{ and here } K = 0.9) \\ \lambda = X - \text{ray wavelength (Angstroms), here } 1.5418 \text{ \AA} \\ \beta = \text{Pure diffraction line width or Full Width Half Maximum (FWHM) which is corrected} \\ \quad \text{for } K_{\alpha} \text{ X - ray doublet separation and instrumental broadening (in radians)} \\ \theta = \frac{1}{2} 2\theta \text{ Bragg angle (peak positions)} \end{array} \right.$$

In this experiment however, because of existence of so many growth orientations and especially because of overlapping main peaks of constituent materials, the error calculated in the average crystallite size would be a lot! Therefore it was not calculated.

5.5 TRANSPORT & MAGNETIZATION RESULTS

5.5.1 CRITICAL TRANSITION TEMPERATURE

Figure 5.13(a) shows the transition temperature of the pure Nb and two nanocomposite samples (b and c) having different amount of Gd, in different magnetic fields. The measurements were done both in perpendicular and in plane (perpendicular to current) magnetic field geometries. These two geometries are shown in figure 5.11. The transition temperature of samples with more amount of Gd should decrease compare to pure Nb because of the proximity effect. Additionally the nature of a composite necessitates a large surface area between the constituents which implies a stronger suppression and further decrease in the transition temperature. This matter is observed in two nanocomposite samples with different amount of Gd. The pure Nb shows a transition temperature which is less than the composite. The explanation for this unexpected result, could be attributed to either presence of oxygen atoms or molecules due to non-ideal vacuum of the system or as explained in section 5.4, the high amount of Gd, motivates the reaction between Nb and sapphire, which itself is a superconductor with higher transition temperature and therefore increase the transition temperature of the composite.

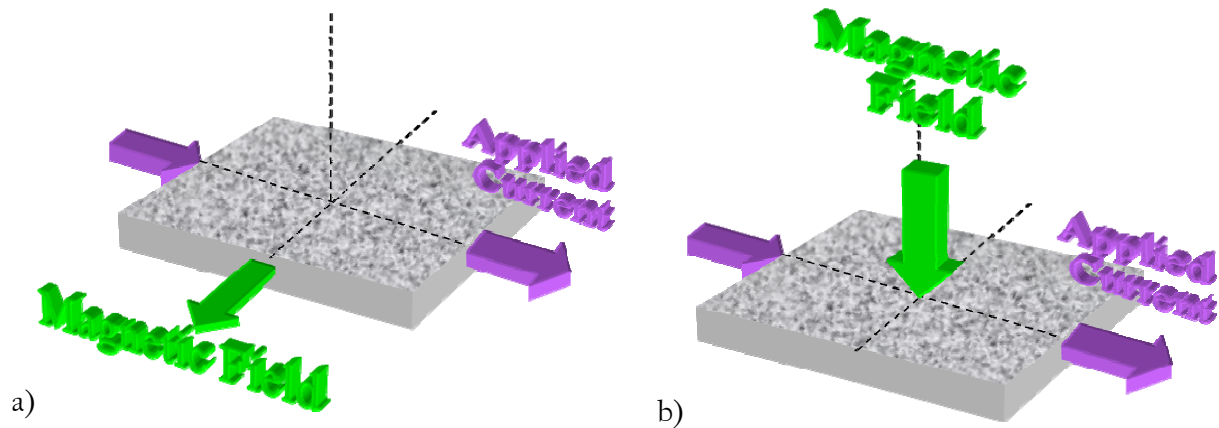


Figure 5.11. Two different geometries used for transport measurements. a) In plane magnetic field (perpendicular to the current), b) Perpendicular magnetic field.

The temperature dependence of critical field is well described by the empirical formula,

$$H_{c1}(T) = H_{c1}(0) \left[1 - (T/T_C)^2 \right]$$

The $H_{c1}(0)$ is the critical field extrapolated to absolute zero. This dependence is shown in figure 5.12 which essentially shows the H - T phase diagram of the superconducting state.

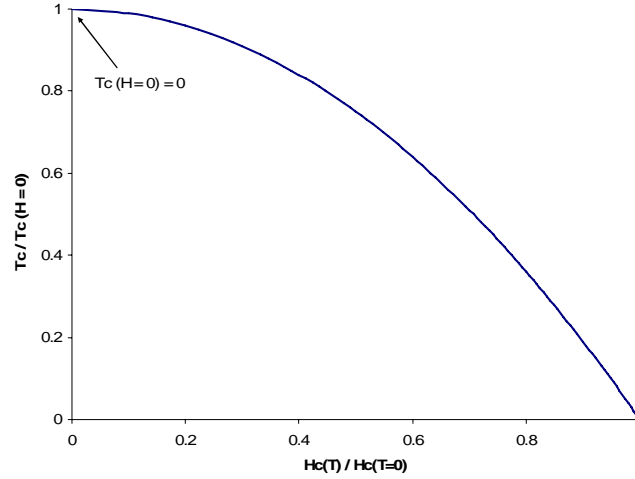


Figure 5.12. The H-T phase diagram of the superconducting state

The effect of magnetic field on critical temperature can be derived from this empirical formula:

$$H_{c1}(T) = H_{c1}(0) \left[1 - (T/T_C)^2 \right] \Rightarrow \frac{H_{c1}(T)}{H_{c1}(0)} = \left[1 - \left(\frac{T}{T_C} \right)^2 \right] \Rightarrow \left(\frac{T}{T_C} \right)^2 = 1 - \frac{H_{c1}(T)}{H_{c1}(0)}$$

$$\text{We can interpret this as } \Rightarrow \frac{T_C(\text{at } H \text{ field})}{T_C(\text{at zero } H)} = \sqrt{1 - \frac{H_{c1}(T)}{H_{c1}(T=0)}}$$

Therefore as it is obvious from the above figure, by increasing the field

$$\begin{aligned} \text{at } H = 0 \Rightarrow T = T_C \text{ However, if } H \uparrow \Rightarrow \frac{H_{c1}(T)}{H_{c1}(T=0)} \uparrow \Rightarrow \frac{T_C(H)}{T_C(H=0)} < 1 \text{ (although keep increasing)} \\ \Rightarrow T_C(H) \downarrow \text{ Until at } H = H_{c1}(T) \Rightarrow T_C = 0 \end{aligned}$$

Also one can argue by increasing the magnetic field, the density of the magnetic fluxes threading the superconductor increases, therefore the transition from superconductor to normal state (which occurs when the normal cores of the vortices start to overlap) happens at lower temperatures. Moreover, an applied magnetic field, tries to break apart the electrons with opposite movement directions or momentums (+ p and $-p$ momentums), in other words, the magnetic field like to tear the Cooper pair apart and therefore destroy the superconductivity. Hence the voltage potential or the attractive force keeping the electrons together, decreases and the energy gap of the Cooper pairs increase which itself implies the suppression of the superconductivity at lower temperatures (lower T_c).

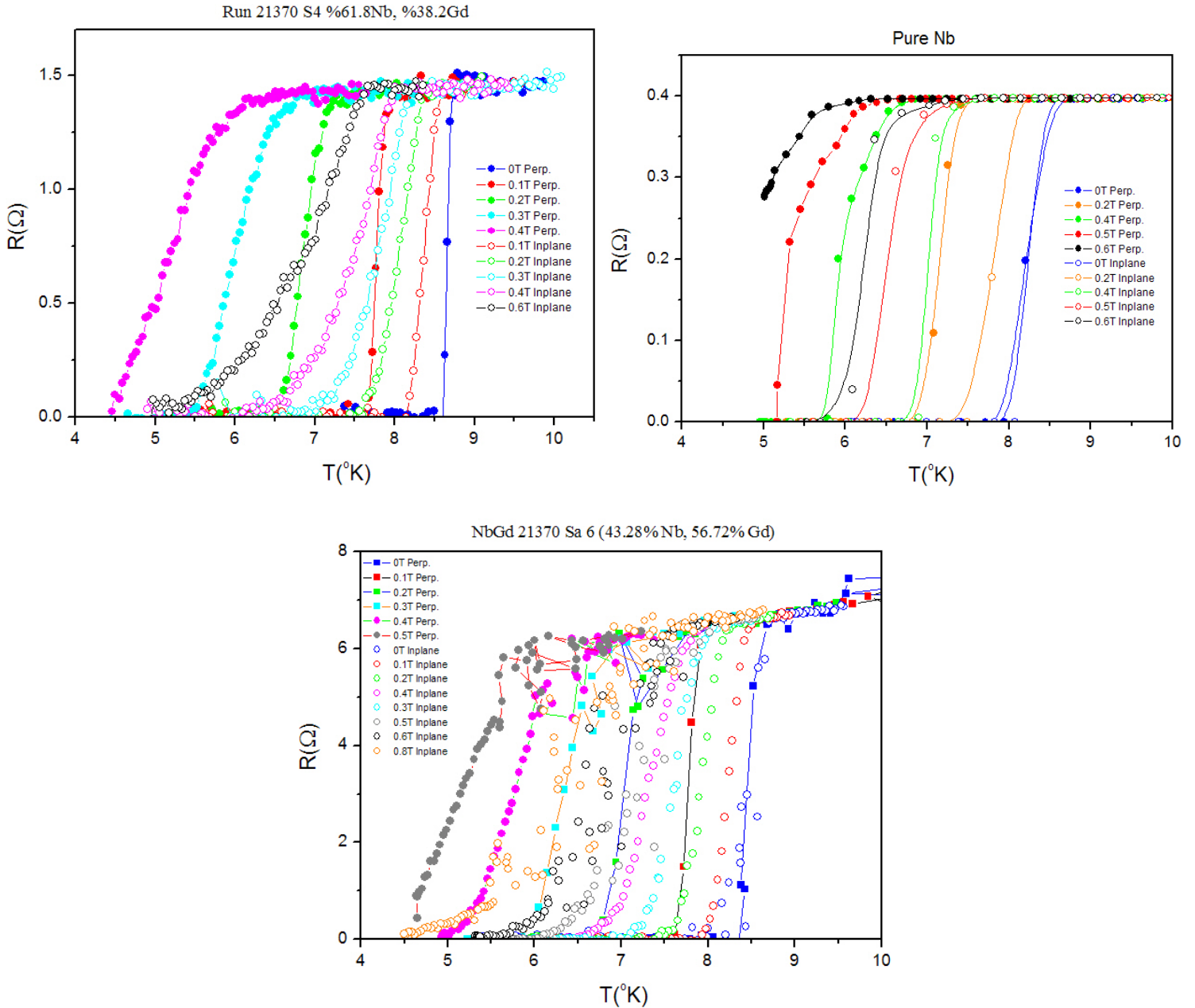


Figure 5.13. The R-T curves for pure Nb and two nanocomposite samples with different Gd amounts both in perpendicular and In-plane (parallel) fields.

Also as it's obvious from the figure 5.13, there is a difference in transition temperatures of the samples measured in-plane (perpendicular to current) and perpendicular fields. This cause for this observation can be attributed to either the demagnetizing effect or the phenomenon called surface superconductivity which happens in the case of a parallel field.

The magnetic behavior of a homogenous isotropic sample such as M or χ does not only depend on its intrinsic magnetic properties, but also on its geometry. The effect of the geometry of the sample on its magnetic properties is usually known as the “Demagnetizing Effect”. The demagnetizing effects can change B , H or M by several orders of magnitude when comparing samples with the same intrinsic properties but different geometries. In the

case of perpendicular field, because of the demagnetizing effect, magnetization is negative and therefore the initial field in the sample is higher than the applied field ($H_i > H_a$), therefore the transition temperature in this case is lower.

The demagnetizing factor for a disc of radius “ a ” and thickness “ t ” assuming that $a \gg t$, in a field perpendicular to the sample surface is:

$$n(\text{Demagnetizing Factor}) \cong 1 - \frac{t}{2a} \Rightarrow H_{\text{internal}} = \frac{H_a}{1-n} = \frac{2aH_a}{t}$$

Considering a 4 x 4 mm sample with 200nm film (on a say 600 μ m substrate), the internal field when applying a 1T stray field, would be:

$$n \cong 1 - \frac{600.2 \mu\text{m}}{2 \times 4000 \mu\text{m}} = 0.075 \Rightarrow H_{\text{internal}} = \frac{1T}{1-0.075} = 1.081T$$

Which is not so higher than 1T and although effective but could not be the main cause for the decrease seen in the transition temperature. However, we know that in the superconducting state, we have perfect diamagnetism ($\chi = -1$) and near the transition temperature, the susceptibility is almost zero ($\chi \approx 0$). Therefore one can argue that near the transition temperature, the sample is weakly magnetic hence the demagnetizing effect is not important.

Other possibility as mentioned before could be because of the phenomenon called surface superconductivity or the third critical field. In order to understand this phenomenon, let's review the superconductivity in a bulk type two superconductor. Considering a Type II superconductor in an external magnetic field H_0 decreasing from $H_0 > H_{c2}$. At the moment when H_0 falls just below H_{c2} , superconducting nuclei appear all over the volume of the superconductor and a tightly packed vortex lattice forms. The order parameter, ψ , at this field is small ($\psi \ll 1$). In other words, a phase transition of second order occurs as the material goes from the normal ($H_0 > H_{c2}$) to the mixed state ($H_0 < H_{c2}$). The nucleus of superconductivity mentioned above is a region between the normal cores of two neighboring vortices. The thickness of this region is of the order of $2\xi(T)$ because if the vortex lattice is close-packed and the radius of the normal core is assumed to be ξ , the distance between the core centers is $\sim 2\xi$.

This is how superconductivity arises in the bulk of a Type II superconductor at H_{c2} . It turns out that at the surface of a superconductor, the superconductor state can exist in much higher field, provided the surface is *parallel* (in-plane) to the external field. Therefore the critical field for the formation of the surface nucleus of the vortices can be expected to be larger than the critical field for a bulk superconductor. This follows from the expression for the critical field of a thin film which is most relevant when considering surface superconductivity.

The critical field of a thin film of thickness d in a parallel external field H_0 is [24]

$$H_{C\parallel} = 2\sqrt{6}H_{cm} \frac{\lambda}{d}$$

Thus as the critical thickness of the film decreases, its critical field goes up. Therefore we should expect the critical field for the nucleation of the surface superconductivity to be approximately twice the critical field for bulk superconductivity. As a matter of fact numerical calculations have shown that [23]

$$H_{C3} = 1.69 H_C$$

So as the external field decreases and reaches the value H_{c3} from above, a thin superconducting layer appears at the surface of a superconductor. The thickness of this layer is of the order of $\xi(T)$. The bulk of the superconductor remains normal and the magnetic field there is equal to the external field. In the surface superconducting layer, the magnetic field is somewhat weakened and the analogy with a thin superconducting layer implies screening effects both in the inner and the outer surfaces of the superconducting layer in opposite directions.

One explanation for the difference in transition temperatures measured at parallel and perpendicular fields, as mentioned before could be because of the existence of surface superconductivity. In the below diagram, the phase diagram of a Type II superconductor has been shown. When cooling a sample at a fixed field, say H (parallel), the transition from normal state to surface superconducting state happens at T_{Hc3} and the transition from surface superconducting state to mixed state happens at T_{Hc2} which is as clear from the figure, $T_{Hc3} > T_{Hc2}$ therefore, the transition temperature of the superconductor in a fixed field is higher in parallel field than a perpendicular field.

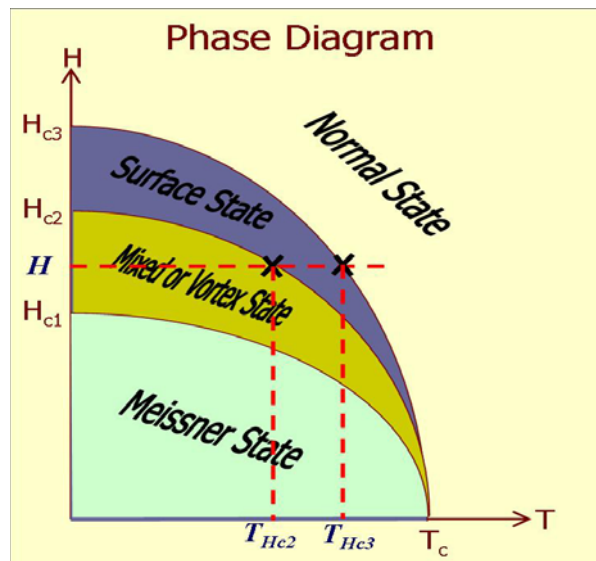


Figure 5.14. The phase diagram of a Type II superconductor showing surface superconductivity.

To prove the existence of surface superconductivity, we consider the transition temperature measured at for example 0.4T parallel field (the green empty circles in pure Nb), because we know that surface superconductivity happens in parallel fields to the surface.

In this field if we consider the existence of surface superconductivity, there should exist a third critical field H_{c3} in the case of parallel 0.4T field. However, if we consider a perpendicular field, as there is no surface superconductivity, hence no third transition temperature, the second critical field in this case should agree with agree with the numerically calculated formula relating second critical field in perpendicular field to the third critical field in the parallel field:

$$\text{@ parallel field } H_{\parallel} = 0.4T \Rightarrow \text{Surface Superconductivity} \Rightarrow H_{C3} \Rightarrow H_{C2} = \frac{0.4}{1.69} = 0.24T$$

$$\text{@ perpendicular field } H_{\perp} \Rightarrow \text{there is no } H_{C3} \Rightarrow H_{C2} = 0.2T \text{ (the solid orange line)}$$

According to the experiments, the data corresponding to parallel 0.4 T field superimpose the data for perpendicular 0.4T field (the minor difference could be attributed to the approximations used in the numerical calculations for deriving the relationship between second and third critical fields).

5.5.2 CRITICAL CURRENT OF NIOBIUM PLANE AND THE NANOCOMPOSITE

As mentioned in section 2.4.1, the technological importance of a Type II superconductor requires carrying as much amount of electrical current as possible without energy dissipation, which occurs when Abrikosov vortices start to move under the influence of Lorentz force. The solution is to avoid their movements by the so-called pinning centers.

The critical current measurements (measured in transport method) of the pure Nb along with two nanocomposite samples with different amount of Gd are shown in figure 5.15 for both perpendicular and in-plane fields. The data are normalized to the amount of Gd to take into account the superconducting portion of the film. The details of the measurement procedure have been explained in section 4.7.

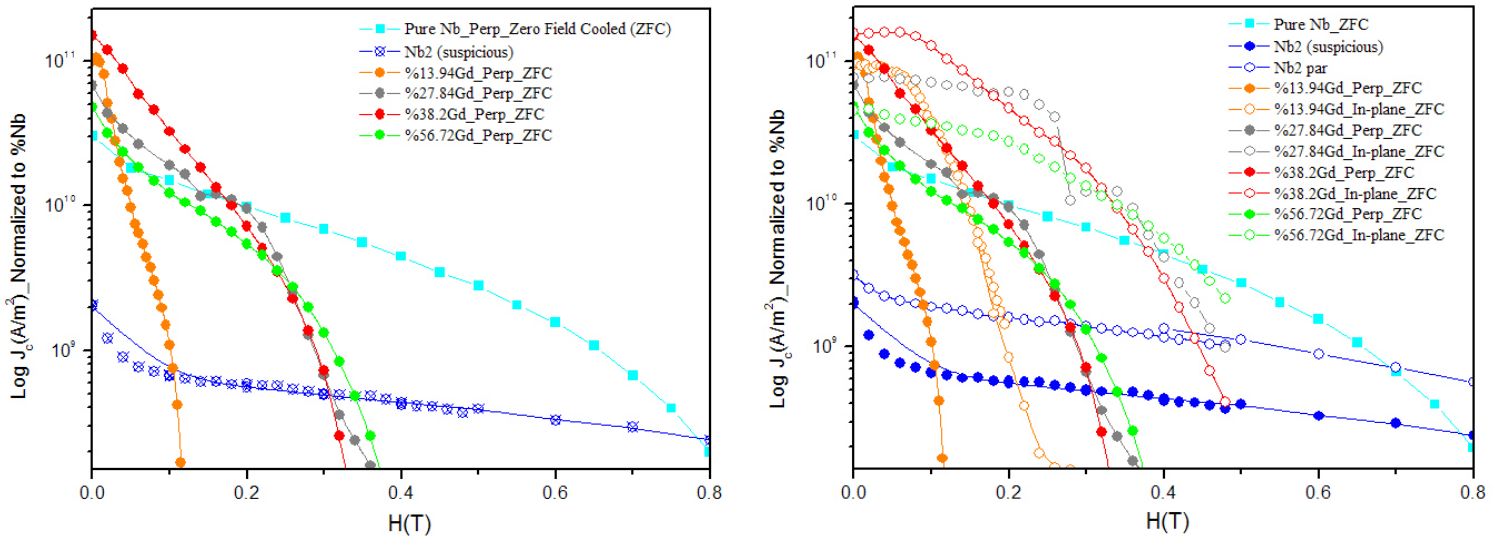


Figure 5.15. Critical current measurement of the pure Nb and two nanocomposite samples with different amounts of Gd in both perpendicular and in-plane magnetic fields (Zero Field Cooled).

It is clear from the above figures that the critical current density of all the nanocomposites having different amounts of Gd has been increased at lower fields, both in perpendicular and in-plane magnetic fields, compared to pure Nb. The same behavior is observed in magnetization measurements in the superconducting state, which will be further discussed in section 5.5.3. However, the critical current extracted from the magnetization curve, $M(H_c)$ (obtained by VSM) is by assuming the critical state model and thus, without any ferromagnetic contribution. The Gd is ferromagnetic and does produce a signal in the measurements which is out of control. Also the level of noise in VSM measurements at 4.9K is fairly high, which means that we could have a small J_c for large applied fields that goes beyond the VSM resolution and thus undetected. Therefore, in general, the transport measurements are more reliable than magnetic measurements for obtaining the critical current. There is no coherent correlation between increasing behavior of the critical current

with amount of Gd. The critical current has been increased compared to pure Nb, in the sample containing 13%Nb, then decreased in the sample with 27%Gd, reaching a peak in the sample with 38%Gd and decreasing significantly in the sample containing 56%Gd. This behavior is shown figure 5.16 for more clarity. Therefore although it can be concluded that adding Gd generally enhances the pinning properties of the pure Nb at lower fields, pinning enhancement is not directly correlated with the amount of Gd. The kink seen in the critical current (both parallel and perpendicular) of the sample having 27.84%Gd, could be attributed to the agglomeration of Gd in one part of the measurement channel.

As the growth conditions for all the films were the same, the inconsistency observed between the amount of Gd and pinning properties, can be attributed to the different morphologies and/or grain structure of the Gd grains in the superconducting matrix. The pinning properties of the superconductor is directly related to the dimension of the pinning centers and the coherence length, ξ , therefore it is suggested that the maximum pinning which occurs in the sample containing 38%Gd is probably because of the least difference between the coherence length and Gd grain size in this particular sample. Also as the distribution of the Gd nanoparticles is totally random in the superconducting matrix, one can argue that this random distribution could lead to some parts of the sample having higher amounts of Gd. This, in turn, results in lower critical current as the in a transport measurement, J_c detects the critical current for the track cross section with the lowest superconducting portion.

The TEM image of one of the samples (containing 32%Gd) was taken only and in order to reveal the relationship between coherence length and grain size or pinning centers' dimensions, all the images of the samples in one experimental run should be taken and compared.

The higher critical current of the nanocomposites at lower fields, can be attributed to the much effective pinning of the vortices in the nanocomposite samples compared to the pure Nb.

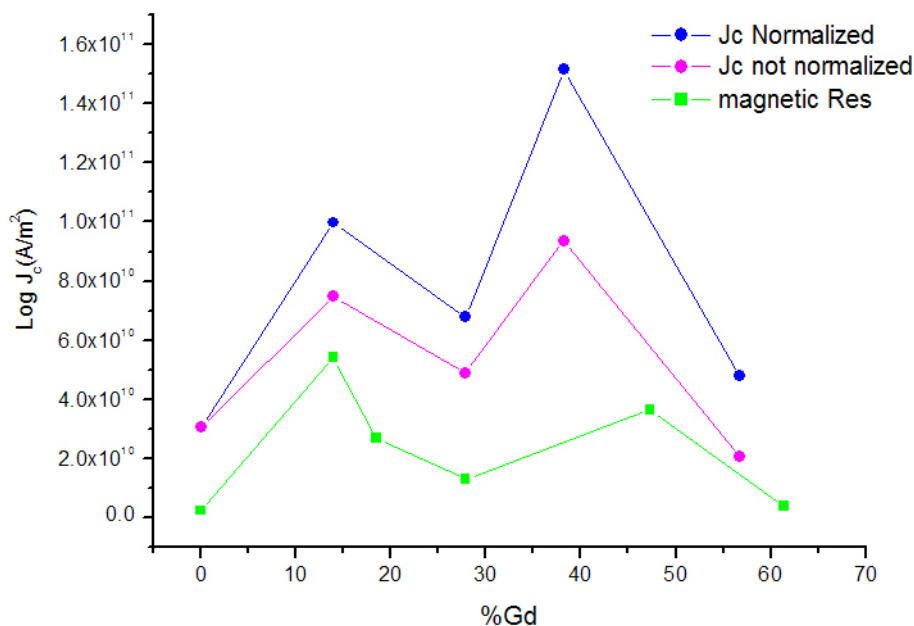


Figure 5.16. The graph of critical current for different amounts of Gd (Zero field cooled condotion).

This seems reasonable as the Gd grains will enhance the pinning efficiency by the so-called core pinning mechanism even if the effect of the magnetic properties of Gd on pinning properties, is ignored. The core pinning introduced by Gd grains is simply the energy reduction brought by moving a vortex from a superconducting region to a non-superconducting (normal) one. Of course the most enhancements in the pinning properties takes place when the dimension of the pinning center is on the length scale of the coherence length (normal core of the vortex).

The decreasing trend of the critical current by increasing the applied magnetic field can be explained by the fact that, by increasing the magnetic field, the number of vortices per unit volume of the specimen increases. Reminding the definition of the critical current which is the current at which the vortices start to move, it is clear that by increasing the number of vortices per unit volume, the number of pinned vortices per unit volume of the specimen increases as well, hence the amount of Lorentz force per unit volume increases and the critical current needed to move the vortices decreases. However, the irreversibility fields or in other words, the fields in which the suppression of the superconduction at 5K (in this experiment) is taken place, is much lower than the pure Nb. Although the irreversibility field can be correlated to the second critical field, but it does not have the exact value as the second critical field is measured at 0K by extrapolating the H - R graphs obtained from resistance measurements. The sample with the most amount of Nb, shows the lowest irreversibility field and by increasing the amount of Gd, the irreversibility field is increased although not reaching the value of the pure Nb, however the critical current decreases.

The calculation of pinning force as a function of magnetic field follows from the Lorentz force (section 2.4.2) as

$$F_L = j_{tr} \times B$$

As the magnetic field and the current are perpendicular, Lorentz force can be written as the scalar product of current density and the magnetic field. Having both, one can calculate the pinning force and its dependence on the magnetic field. The change in the pinning forces per unit volume of the superconductor in the zero field cooled state is shown in figure 5.17. Similarly, it shows that the sample containing higher amount of Gd, has less effective pinning than the sample with less amount of Gd. Also both figures (5.15 and 5.17) show that the pinning is much effective in in-plane field rather than the perpendicular field.

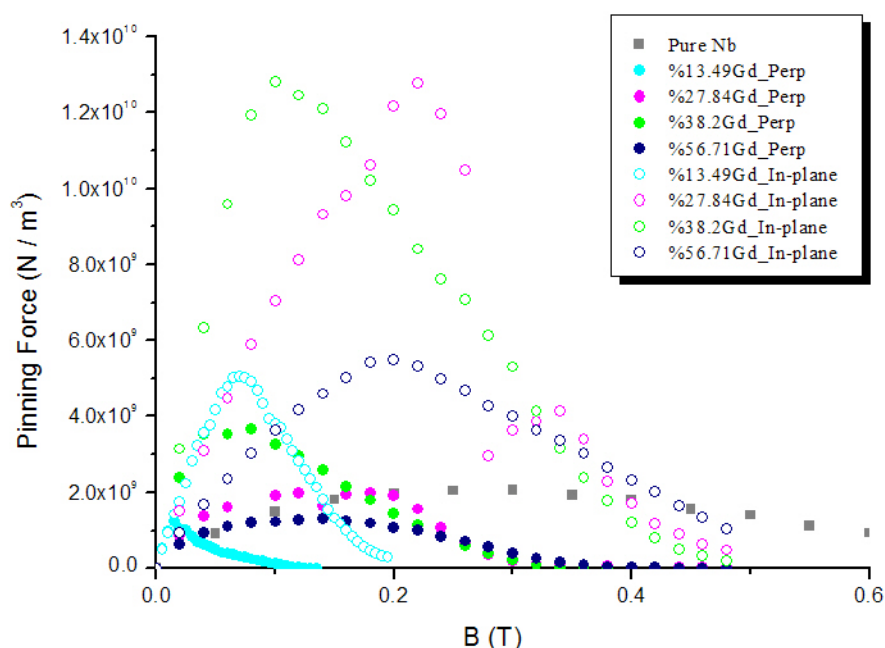


Figure 5.17. The pinning force comparison of the pure Nb and two nanocomposite samples, measured in Zero Field Cooled state.

Further careful study of the critical current of the two samples, close to the zero field, in both Field Cooled (FC) and Zero Field Cooled (ZFC) states, shows a hysteresis behavior in critical current as a function of the magnetic field (perpendicular field). The asymmetric behavior of the critical current versus magnetic field clearly shows the enhancement of pinning by magnetic contributions and rejects the possibility of any shifting in the graphs. In the field cooled state, the sample is first magnetized to 0.1T and then the field is continuously decreased. Keeping in mind that, 0.1T is higher than the saturation field of the Gd, by decreasing the field from 0.1 in the Field Cooled (FC) state, all the Gadolinium grains have already magnetized to their saturation magnetization, whereas, in the Zero Field Cooled (ZFC) state, the sample is exposed to a magnetic field which is gradually increased to reach its saturation magnetic field. Given the above explanation and take another look at figure

5.18, it is clear that the critical current in the FC state is higher than the ZFC state, suggesting the role of magnetic field in pinning enhancement.

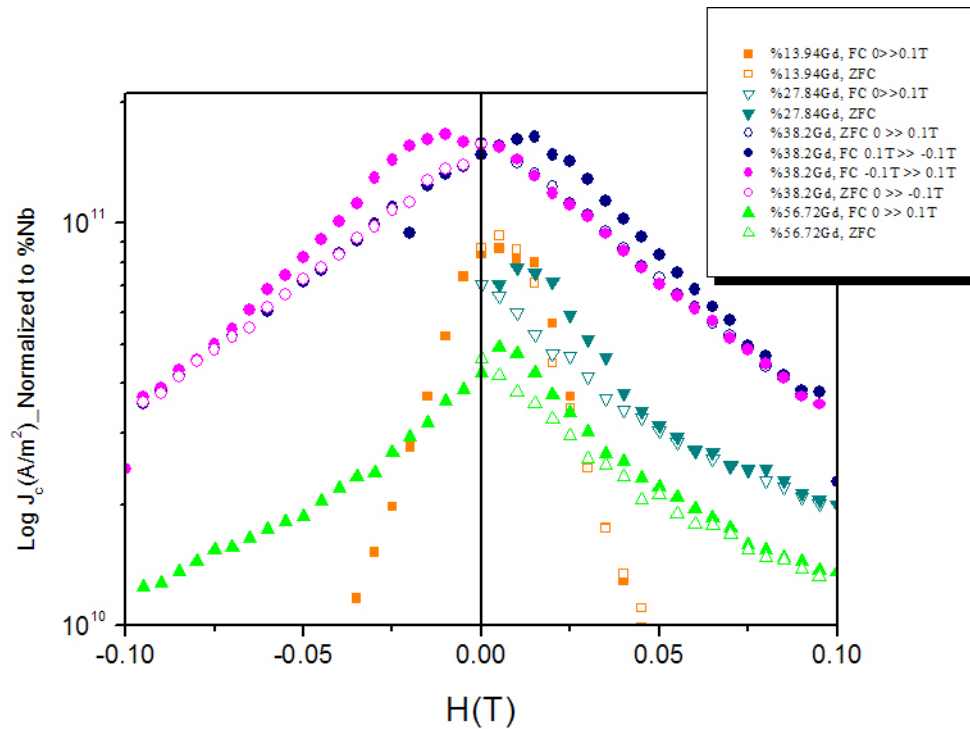


Figure 5.18. Measurement of critical current versus magnetic field in field cooled and zero field cooled states parallel fields).

The changes in the pinning force of a type two superconductor in an applied magnetic field can be divided into two regimes. In the first regime or the so called Single Vortex Motion regime, the pinning force increases linearly by increasing the magnetic field.

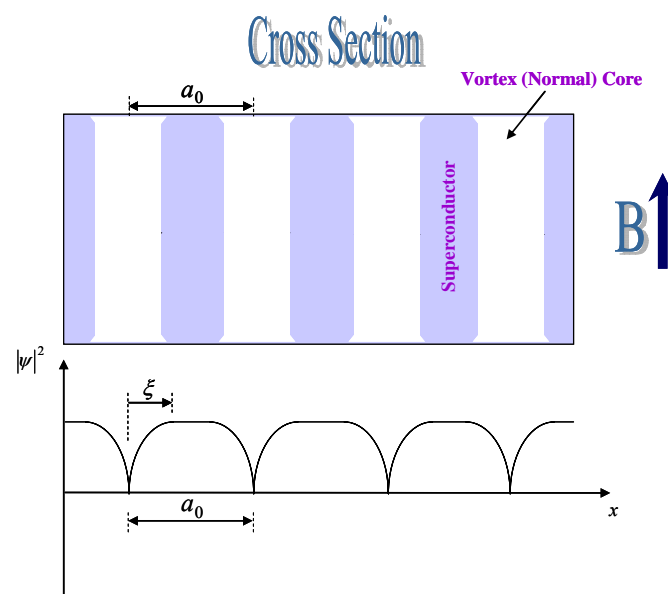
We know that in a Type II superconductor the magnetic field (of course in the fields higher than the first critical field of the superconductor) penetrate the sample in the form of superconducting vortices, each carrying a fluxon of magnetic flux. Considering a number of these vortices in a unit volume of the superconductor which also contains pinning centers such as inhomogeneity, defect, precipitates, and grain boundaries etc. vortices will be pinned by these pinning centers. For low magnetic fields, the number of the pinning centers in this regime exceeds the number of vortices. Therefore by increasing the magnetic field, the number of magnetic fluxes or vortices threading the unit volume of the sample increases, however as there are sufficient pinning centers, all of them would be trapped. Therefore one can say that all the vortices in this regime are effectively pinned and increasing of the magnetic field causes an increase in the number of pinned vortices which in return cause an increase of the pinning force per unit volume of the sample.

However, we reach a state at which all the pinning centers are occupied and increasing the magnetic field would cause an increase in the number of the vortices which are free⁴ to move as there are not sufficient pinning centers to trap them. In this case, the total pinning force per unit volume of the sample is constant as all the pinning centers have been already occupied and new unpinned vortices wouldn't change the total pinning force per unit volume of the sample. But as the magnetic field increases and hence the number of vortices, the free vortices can not move freely in the superconductor matrix as it contains lots of pinned vortices which hinder their motion. By increasing the field, the Lorentz force increases and therefore in this case, the only way for the free vortices to get around this problem is that the whole vortex structure or the vortex lattice starts to flow which obviously requires depinning of the pinned vortices, hence the pinning force per unit volume of the sample starts to decrease.

But then what happens when we increase the magnetic field in the case of constant pinning force, i.e. all the pinning centers have been occupied and the new vortices are free?

Considering a Type II superconductor in a vortex state, the change of superelectron wavefunction (probability) as a function of the distance inside superconductor is shown as below. We also suppose that all the pinning centers have been occupied.

By increasing the magnetic field, the number of free vortices increases and eventually these vortices become so close together that start to overlap.



⁴ Actually these vortices, in a sense are not that free to move as their movement is hindered by the pinned neighboring vortices.

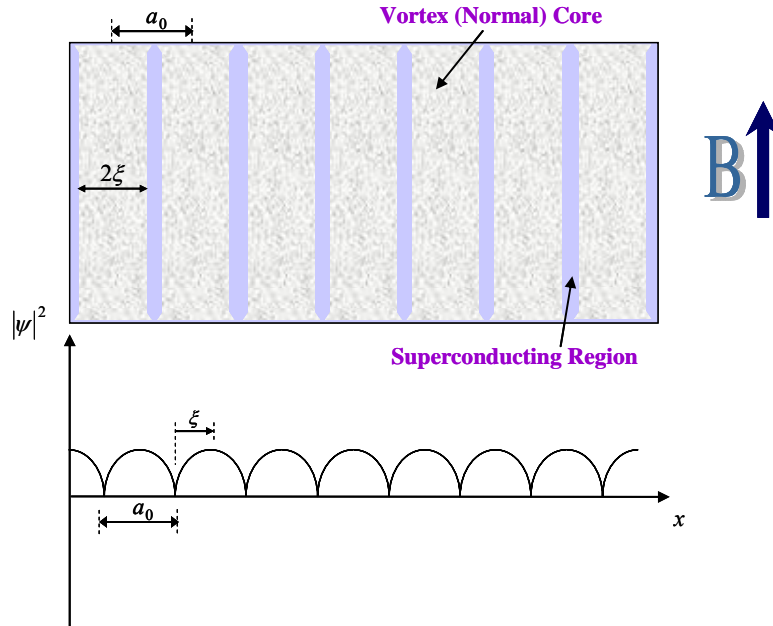


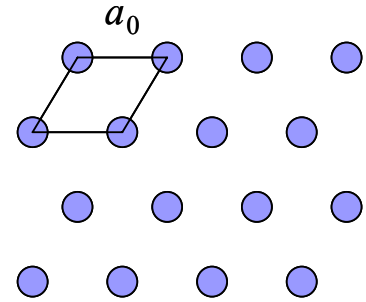
Figure 5.19. Effect of increasing the external magnetic field on the number of vortices threading into the material

Considering a hexagonal array of vortices,

$$\Phi = \frac{B}{S}$$

However, considering the unit cell, the equilibrium state of the vortex lattice in different applied magnetic fields can be calculated as:

$$\Phi_0 = \frac{B}{S} \Rightarrow \Phi_0 = \frac{2B}{a_0^2 \sqrt{3}} \Rightarrow a_0 = \sqrt{\frac{2B}{\sqrt{3}\Phi_0}}$$



Φ_0 is the flux quantum which is,

$$\Phi_0 = \frac{\pi \hbar}{e} \quad (\hbar : h/2\pi, e : \text{electron charge})$$

Also the coherence length, which varies with temperature can be calculated as:

$$\xi(T) = \xi(0) \frac{1}{\sqrt{1 - \frac{T}{T_c}}}$$

$\xi(0)$ is the coherence length at absolute zero which is about 39 nm for pure Nb.

5.5.3 MAGNETIZATION IN THE PRESENCE OF FLUX PINNING

Flux pinning leads to magnetization curves for Type II superconductors which are far from the ideal reversible curve and show very strong hysteresis. For understanding such curves, it's crucial to become familiar with the notion of *Critical State* which first introduced by Bean. The critical state is one at which the field gradient in all points in the sample has its maximum value and the flux is everywhere is on the point of slipping, with $J_t = J_c(B)$.

To investigate the flux pinning in these ferromagnet/superconductor nanocomposites, we have performed VSM magnetization measurements below the critical temperature of the nanocomposite ($T = 4.9$ K). Figure 5.19 shows the hysteresis loop of a superconductor response measured at $T = 4.9$ K which is a typical irreversible magnetization curve of a type superconductor in the presence of flux pinning centers.

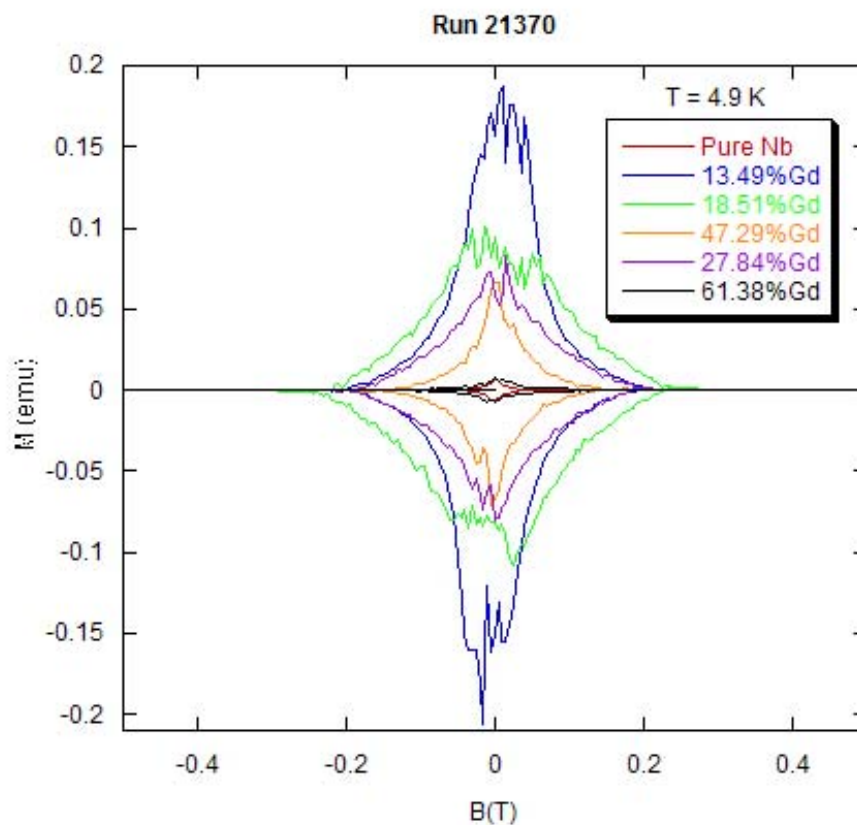


Figure 5.19. Measurement of critical current versus magnetic field in field cooled and zero field cooled states.

The average grain size of Gd grains in the nanocomposite is 20-30 nm (Section 5.3). When the crystallite size of a ferromagnetic material is reduced in one or more dimensions to the nanometer range, the magnetic properties are expected to change dramatically [3]. For nanocrystallites decoupled by a nonmagnetic surface layer, Tronc *et al.* [4] have observed the

superparamagnetic effect. Krill *et al.* [3] studied the magnetization of nanocrystalline Gd grown by inert-gas condensation. They saw two magnetic components, an equilibrium phase (hcp) Gd and a non-ferromagnetic Gd (fcc phase) located in or near the boundary regions in a considerable fraction (~10%) separating adjacent grains which results in two different magnetization behavior and Curie transition temperatures. Such antiferromagnetic or non-ferromagnetic coupling between Gd atoms has been observed before [5]. Such effects can be either attributed to finite size effects regarding the reduction in crystallite grains dimension [8] or the structural distortions associated with the surfaces and interfaces [9].

The saturation magnetization of the Gd is dominated by contribution of the 4f elements [6] which can be considered as a direct measurement for the strength of the exchange field due to the ordered 4f moments that give rise to a Zeeman splitting of the conduction electron band. Based on the theory introduced by Radovic *et al.* [7] for Superconductor-ferromagnet multilayers, this exchange field can also be considered as the main reason for the Cooper pair breakage in ferromagnet phase of the nanocomposite in the absence of an external magnetic field. In order to obtain information on the macroscopic magnetic behavior and also to verify that the gadolinium-containing dispersed composite phase was indeed ferromagnetic metal, magnetic hysteresis loops of the of the nanocomposite sample were measured. The magnetization vs. applied field curve of one of the superconducting samples ($T_c = 8.3$ °C) with 47.29% Gd is shown at 77K and 10K (figure 5.20). The curves are typical of a soft ferromagnetic metal and no superparamagnetic effect was observed.

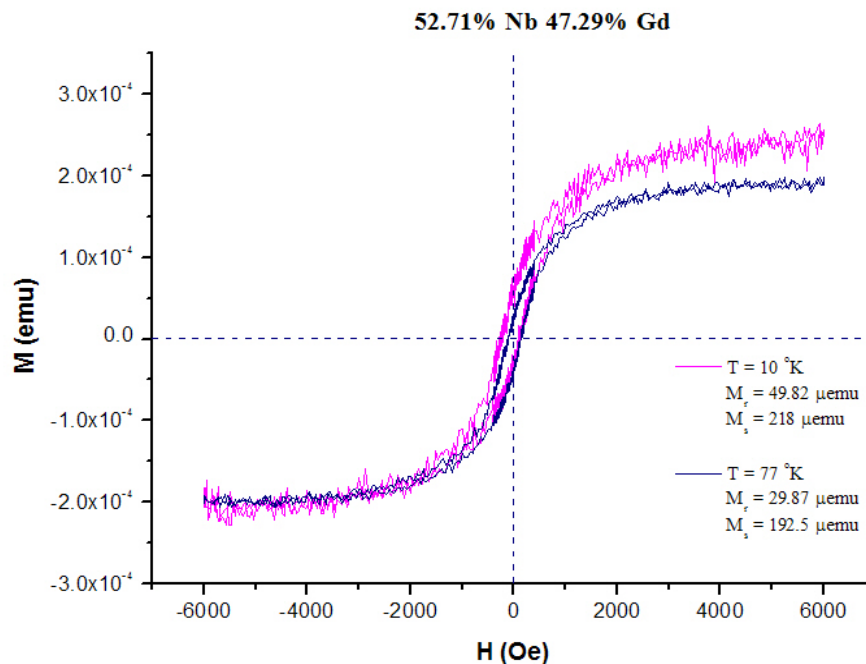


Figure 5.20. Measurement of critical current versus magnetic field in field cooled and zero field cooled states.

Spontaneous magnetization measurement of the sample was also carried out as a function of temperature to find the Curie temperature of the nanocrystalline gadolinium in the nanocomposite. Curie temperature of about 200 °K was found. Lowering of the Curie temperature with respect to the bulk value of 293 °K [6], has also been reported by Farle *et al.* for Gd/W monolayer [10]. The same effect has also been reported by Jiang *et al.* for Nb/Gd multilayers with decreasing the thickness of Gd [11]. In general significant changes in magnetic properties when reducing the crystallite dimensions to nanometer scale can be either attributed to finite size effects regarding the reduction in crystallite grains dimension [8, 12 and 13] or the structural distortions associated with surfaces or interfaces [9].

The measured $M_s(T)$ of gadolinium in the nanocomposite sample appears to vary linearly with temperature (T) and similar behavior has been observed for the thin films of pure gadolinium [12] supported by calculations done in the spin-wave approximation which have attributed it to the dimensionality of the film [14, 15].

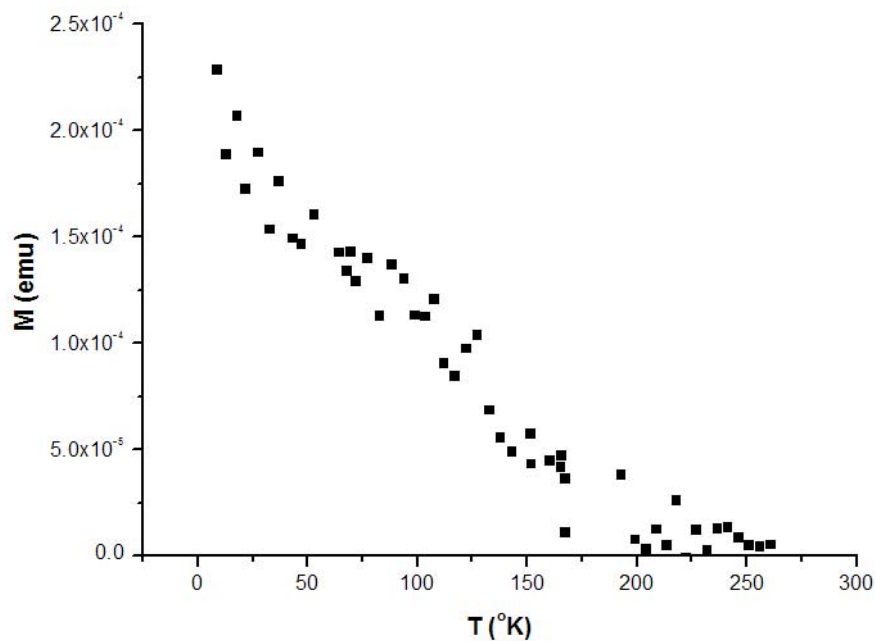


Figure 5.21. Measurement of critical current versus magnetic field in field cooled and zero field cooled states.

A magnetic moment per atom of $0.61\mu_B$ was calculated for a nanocomposite sample of 170 nm containing 47% Gd and saturation magnetism of 218 μemu at 10 °K which is significantly less than the theoretical large magnetization of Gd at low temperatures, $7.5 \mu_B$ per atom at absolute zero [16].

Dimensions of sample = $4 \times 4 \text{ mm}^2$

thickness of film = 100 nm (niobium buffer layer) + 170 nm (nanocomposite)

Gd (HCP), unit cell size $\rightarrow a = 3.64 \text{ \AA}$, $c = 5.78 \text{ \AA}$; *two atoms in the primitive unit cell*

$$\text{Number of unit cells} = \frac{V_{\text{nanocomposite}} \times 47.29\%}{V_{\text{Unit Cell}}} = \frac{4 \times 4 \times 170 \times 10^{12} (\text{nm}^3)}{66.33 \times 10^{-3} (\text{nm}^3)} \times 47.29\% = 19.39 \times 10^{15}$$

$$\begin{aligned} \mu_B / \text{Unit Cell} &= \frac{\text{saturation magnetization in emu} \times (1.0783 \times 10^{20}) \mu_B}{\text{Number of unit cells}} = \\ &= \frac{218 \times 10^{-6} \times (1.0783 \times 10^{20}) (\mu_B)}{19.39 \times 10^{15}} = 1.213 \mu_B \end{aligned}$$

$$\mu_B / \text{Atom} = \frac{\mu_B / \text{Unit Cell}}{\text{number of atoms in unit cell}} = \frac{1.213}{2} = 0.61 \mu_B$$

The reason for this huge loss of magnetic behavior can be explained as follow:

Although the exchange interaction produces strong interactions between neighboring magnetic atoms it can also be mediated by various mechanisms, producing long range effects. As the exchange energy for neighboring atoms is dependent only upon the angle between them it does not give rise to anisotropy [17]. In lanthanide metals, the $4f$ magnetic electrons are highly localized and therefore direct propagation of the exchange interaction is not energetically favorable [18]. However, in these metals where there is little or no direct overlap between the wavefunctions of neighboring magnetic electrons, indirect exchange couples moments over relatively large distances. It therefore acts through an intermediary which in metals is the conduction electrons (itinerant electrons) [18]. In this form of exchange, the magnetic ion induces a spin polarization on the conduction electrons in its neighborhood which is then felt by magnetic moments of other magnetic ions within range, leading to an indirect coupling. This type of exchange was first proposed by Ruderman and Kittel [19] and later extended by Kasuya and Yosida independently [20] to give the theory now generally known as the RKKY interaction. For example in multilayers where magnetic layers are separated by a non-magnetic layer, there can be exchange coupling between two magnetic layers which is mediated by RKKY interaction and has an oscillatory dependence on the thickness of the spacer [21]. The interaction between magnetic moments in Gd phases of the nanocomposite can be considered to be governed by the RKKY coupling which oscillates in sign with increasing atomic separation⁵ [18].

Atomic disorder at the boundary regions of Nb and Gd and structural distortions associated with the increase in the number of surfaces and interfaces (due to the reduction of crystallite

⁵ The origin of the oscillation observed in RKKY interaction is coupling coefficient, j , which oscillates from positive to negative as the separation of the ions changes and has a damped oscillatory nature.

size), can be possible reasons for changing the distribution of the interatomic distances at the Gd phase and specially in grain boundaries. Therefore depending upon the separation between a pair of ions, their magnetic coupling can be either ferromagnetic or antiferromagnetic, i.e. some of the Gd atoms in a certain Gd nanocrystalline in the nanocomposite may be coupled antiferromagnetically to their nearest neighbors. This probable disorder in the orientation of the magnetic moments in these regions may be the reason to their little or no contribution to the total magnetic signal of the nanocomposite. Observation of the *fcc* phase Gd in XRD data, further support the consistency of this explanation as the *fcc* phase Gd is shown to have antiferromagnetic behavior [22].

BIBLIOGRAPHY

- [1] C. Kittel, *Introduction to Solid State Physics*, John Wiley and Son's (1996).
- [2] O.J. Bressan. *J. Phys. F*, **5** (1975).
- [3] C. E. Krill, F. Merzoug, W. Krauss and R. Birringer, *Nanostr. Mat.* **9**, pp. 455-458 (1997).
- [4] E. Tronc, P. Pren~, J. P. Solivet, D. Fioranl, A. M. Testa, R. Cherkaoui, M. Nogu~s and J. L. Dormann, *Nanostrue. Mater.* **6**, 945 (1995).
- [5] P. E. Chizhov, A. N. Kostigov and V. I. Petinov, *Solid State Commun.* **42**, 323 (1982).
- [6] W. C. Koehler, in R. J. Elliot (ed.), *Magnetic Properties of Rare Earth Metals*, Plenum, New York, pp. 81 (1972).
- [7] Z. Radovic, L. Dobrosavljevic-Grujic, A. I. Buzdin and J. R. Clem, *Phys. Rev. B*, **38**, 759 (1991).
- [8] M. E. Fisher and A. E. Ferdinand, *Phys. Rev. Lett.* **19** 169 (1967).
- [9] H.-E. Schaefer, H. Kisker, H. Kronmiiller and R. Wiirschum, *Nanostruct. Mater.* **1**, 523 (1992).
- [10] M. Farle, K. Baberschke, U. Stutter, A. Aspelmeier and F. Gerhardter, *Phys. Rev. B* **47**, 11571 (1993).
- [11] J. S. Jiang, D. Davidovic, Daniel H. Reich and C. L. Chien, *Phys. Rev. Lett.* **74**, 2 (1995).
- [12] U. Paschen, C. Surgers and H. V. Lohneysen, *Z. Phys. B*, **90**, 289 (1993).
- [13] M. E. Fisher and M. N. Barber, *Phys. Rev. Lett.* **28**, 1516 (1972).
- [14] L. Valenta, *Phys. Status Solidi*, **2**, 112 (1962).
- [15] R. J. Jelitto, *Z. Naturforsch.* **19a**, 1567 (1964); **19a**, 1580 (1964).
- [16] P. Tessier *et al.* *J. of Alloys and Comp.*, **330-332**, pp. 369-372 (2002).
- [17] J. Bland, *PhD Thesis: A Mössbauer Spectroscopy and Magnetometry Study of Magnetic Multilayers and Oxides*, Liverpool University (2002).
- [18] D. Jilles, *Introduction to Magnetism and Magnetic Materials*, 2nd ed. Pp. 316-318, Chapman & Hall, London (1998) or R. J. Elliott, in *Magnetism*, (eds.) George T. Rado and Harry Suhl, Vol. II, Part A, pp. 406-421, Academic, New York (1965).
- [19] M. A. Ruderman, and C. Kittel, *Phys. Rev.* **96**, 99 (1954).
- [20] T. Kasuya, *Prog. Theor. Phys.* **16**, 45 (1956). And K. Yosida, *Phys. Rev.* **106**, 893 (1957).
- [21] S. S. P. Parkin, N. More and K. P. Roche, *Phys. Rev. Lett.* **64**, 2304 (1990).
- [22] P. E. Chizov, A. N. Kostigov and V. I. Petinov, *Solid State Commun.* **42**, 323 (1982).
- [23] [4] M. Tinkham, *Introduction to Superconductivity*, McGraw-Hill (1996).
- [24] V. V. Schmidt; P. Muller, A. V. Ustinov (eds) "*The Physics of Superconductors: Introduction to Fundamentals and Applications*" (Springer, Germany, 1997)